Interference experiments with a single Barium ion: from QED towards quantum feedback

Dissertation

zur Erlangung des Doktorgrades an der
naturwissenschaftlichen Fakultät
der Leopold-Franzens-Universität Innsbruck

vorgelegt von

Pavel Aleksandrovich Bushev

durchgeführt am Institut für Experimentalphysik
unter der Leitung von
Univ.-Prof. Dr. Rainer Blatt

June 2004

Abstract

This thesis reports on different experiments, from measurements of cavity QED effects to demonstration of feedback control of a motional state, conducted with a single $^{138}\mathrm{Ba}^+$ ion in an interference setup.

For these purposes a single barium ion is confined in a spherical Paul trap and continuously excited and cooled by near-resonant lasers on its $\mathrm{P}_{1/2} \rightarrow \mathrm{S}_{1/2}$ at 493 nm and $\mathrm{P}_{1/2} \rightarrow \mathrm{D}_{3/2}$ at 650 nm. A collimating lens and a distant mirror are placed such that 4% of the 493 nm resonance fluorescent light is retroreflected, resulting in interference fringes. It leads also to a modification of the spontaneous emission rate on the $\mathrm{P}_{1/2} \rightarrow \mathrm{S}_{1/2}$ transition and to an energy shift of the $\mathrm{P}_{1/2}$ state as well.

The modification of decay causes a modulation of the fluorescence at 650 nm with the same period as that for the 493 nm interference fringes. The level shift of the excited level results in the phase difference between 493 nm interference fringes and the 650 nm modulation fringes which varies with the 650 nm laser detuning and takes all values between correlation (phase close to 0 or 2π) and anti-correlation (phase π). The measured amplitude of the level shift is approximately equal to 240 kHz.

In the second part of the thesis the mechanical action of the fluorescence light which is reflected back onto the Ba^+ ion is demonstrated. The energy shift of $\mathrm{P}_{1/2}$ state has a sinusoidal dependence on the ion-mirror distance, thus leading to a spatially dependent force on the excited ion which changes the trap frequency by up to 300 Hz. RF spectral analysis of the resonance fluorescence allows sensitive and rapid measurement of the ion's 1 MHz oscillation frequency. We measure this sinusoidal variation of the trap frequency with an error less than 10 Hz by positioning the ion with nm-accuracy relative to the mirror.

The last part of the thesis is devoted to the control of an ion's motion by using active feedback. First, we use a phase-locked loop to synchronize the ion's oscillation to some external frequency generator. Secondly, we implement feedback based on the "cold damping" technique to cool the ion below the Doppler limit, by creating additional viscous force. We observe a reduction of the amplitude of the sideband while increasing the gain of the feedback. For sufficiently high loop gain a 7 dB Poissonian noise suppression is reached.

Zusammenfassung

Diese Arbeit berichtet von verschiedenen Experimenten, die an einem einzelnen $^{138}Ba^+$ Ion in einem Interferenzaufbau durchgeführt wurden. Die Messungen reichen von der Untersuchung von QED Effekten bis hin zur Realisierung einer aktiven Rückkopplung zur Kontrolle von Bewegungszuständen eines Ions.

Ein einzelnes Barium-Ion wird dazu in einer sphärischen Paul-Falle gespeichert und kontinuierlich durch resonante Laser auf den Übergängen $P_{1/2} \rightarrow S_{1/2}$ bei 493 nm und $P_{1/2} \rightarrow D_{3/2}$ bei 650 nm angeregt und lasergekühlt. Eine Linse sammelt 4% der Resonanzfluoreszenz des Ions auf und erzeugt einen kollimierten Strahl, der von einem 25 cm entfernter Spiegel zurückreflektiert wird. Dies führt nicht nur zu Interferenz, sondern auch zu einer Veränderung der Spontanemissionsrate auf dem $P_{1/2} \rightarrow S_{1/2}$ Übergang und zu einer Energieverschiebung des $P_{1/2}$ Zustandes.

Die Veränderung der Spontanemissionsrate moduliert die Fluoreszenz bei 650 nm mit derselben Periode wie das Interferenzmuster bei 493 nm. Durch die Energieverschiebung des angeregten Zustandes entsteht ein Phasenunterschied zwischen dem Interferenzmuster bei 493 nm und der Modulation der Zerfallsrate auf dem Übergang bei 650 nm. Dieser Phasenunterschied variiert in Abhängigkeit von der Verstimmung des Lasers bei 650 nm und kann alle Werte von Korrelation (Phasenunterschied ca. 0 oder 2π) bis zu Antikorrelation (Phasenunterschied von π) annehmen. Die Grösse der Energieverschiebung liegt im Bereich von 240 kHz.

Im zweiten Teil dieser Arbeit wird gezeigt, wie das rückreflektierte Fluoreszenzlicht das Ba+ Ion mechanisch beeinflusst. Die Energieverschiebung des $P_{1/2}$ Zustandes hat eine sinusförmige Abhängigkeit von dem Abstand Spiegel zu Ion . Dies führt zu einer räumlich veränderlichen Kraft, die auf das Ion wirkt und die Fallenfrequenz bis zu 300 Hz verschiebt. Die Analyse des Spektrums der Resonanzfluoreszenz erlaubt eine schnelle und empfindliche Messung der Oszillationsfrequenz des Ions bei ca 1 MHz. Die Verschiebung dieser Frequenz kann bis auf 10 Hz genau gemessen werden, indem das Ion auf einige nm genau relativ zum Spiegel fixiert wird.

Im letzten Teil dieser Arbeit wird von der Kontrolle der Bewegung des Ions mit Hilfe einer Rückkopplungstechnik berichtet. Als erstes wird ein phasenstabilen Regelkreis verwendet, um die Ionen-Oszillation an einen externen Frequenzgenerator zu koppeln. Danach wird eine Rückkopplung basierend auf der "cold damping" Technik eingesetzt, um das Ion unter das Doppler Limit zu kühlen. Wir beobachten eine Verringerung der Fläche des Seitenbandspektrums mit zunehmender Stärke der Rückkopplung. Ab einer bestimmten Verstärkung kann das Poisson Rauschen bis zu 7 db unterdrückt werden.

Contents

1 Introduction 1

2 Earlier experiments with a single Ba$^+$ ion 5
2.1 The ^{138}Ba$^+$ ion 5
2.2 The Paul trap 5
2.3 An initial interference experiment with a single Ba$^+$ ion 8

3 A classical antenna in front of a single distant mirror 11
3.1 Radiating dipole in free space 11
3.2 Radiative reaction of a dipole on retroreflected field 13
3.3 Action of a lens 15
3.4 Directive antennas and an atom inside the cavity 17

4 An atom in front of a single distant mirror 19
4.1 Atom-field interactions in the dipole approximation 19
4.1.1 Field description 19
4.1.2 Atom-field interactions 20
4.2 Spontaneous decay rate modification by a perfectly conducting wall . . 22
4.3 Level shift induced by a perfectly conducting wall 23
4.3.1 Ground-state level shifts 23
4.3.2 Excited-state level shifts 24
4.4 1D theory of the excited state level shift modified by a mirror 25

5 The modified Bloch equations 27
5.1 The optical Bloch equations 27
5.2 Excitation spectra 29
5.3 Correlation phase 30

6 Spectroscopic method of level shift measurements 35
6.1 The quality of the focusing retroreflected beam onto the ion 35
6.2 FFT of the red and the green fringes 37
6.3 Measurement of the correlation phase 38
6.4 Multilevel effects in correlation phase measurements 41

7 Detection of macro-motional sidebands 43
7.1 Detection of ion motion 44
7.2 Experimental setup 47
7.3 Detection of the macro-motional sidebands 49
7.4 Detection of the macro-motional sidebands with different cooling beam directions 51

8 Mechanical action of the mirror-modified field on the single atom 59
8.1 The experimental method 59
8.2 Level shift measurement via detection of an ion motion 61
8.3 Frequency shift versus probability to be an exited state 64
8.4 Trapping forces 65
8.5 Vacuum versus self-reaction 67

9 Observation of an ion's macro-motion in real time 71
9.1 Experimental setup 71
9.2 Calibration of the motion 73
9.3 Observation of ion motion 75
9.4 Phase locking of ion macro-motion 76
  9.4.1 Experimental setup 76
  9.4.2 Tracking the instantaneous frequency of the excited ion motion 79
  9.4.3 Phase locking of a mono-ion oscillator to sinusoidal signal 81
  9.4.4 Phase locking of a mono-ion oscillator to FM signal 84
9.5 The conclusion and outlook for PLL feedback experiment 85

10 Towards quantum feedback 87
10.1 Thermally excited harmonic oscillator 87
10.2 Cold damping technique 88
10.3 Experimental setup 90
10.4 Experimental results 91

11 Summary and conclusions 95

Bibliography 97

1 Introduction

The simplest system which radiates electromagnetic waves is an oscillating dipole. This is known as a Hertzian dipole, after H. R. Hertz who calculated first its electromagnetic field and made the first experimental demonstration that electromagnetic waves can be emitted by a current loop (dipole antenna) in 1888 [1].

It is known, that any radiating system can be imagined as a set of these elementary dipoles [2]. The radiating properties (radiation pattern, resonant frequency, etc.) of such a system depend on the properties of each dipole and on the surroundings of that system, the latter change boundary conditions for the emitted radiation. If, for example, the radiating dipole is brought in the vicinity of a reflector, the field which is reflected back onto the dipole modifies its linewidth and its resonant frequency [3]. This fact is used in the design of antennas in the RF range, where its emission diagram can be changed by placing the radiating dipole antenna between passive reflecting elements. It is well-known that such geometric modifications also change the resonance frequency of the antenna [4]. It is important to point out that the same effects exist even if the radiating system is described by quantum mechanics, i.e. in the case of an atom or an ion, where the classical current is replaced by the transition probability.

An atom which sits in the vicinity of mirrors or reflectors experiences energy shifts of its electronic states and a modification of the spontaneous decay rate. The experimental observation of the spontaneous decay rate change was first made by K. Drexhage et. al. [5], where radiators (Eu^{3+} ions) were deposited as mono-layers at well controlled distance (down to 2 nm) from a metal surface. The same effect has recently been demonstrated in the case of a single laser excited Ba^+ which is placed 25 cm from a mirror [6].

The level shifts are known as the van der Waals [7], Casimir-Polder [8] and resonant radiative shifts [3,9], the latter being caused by a retarded interaction of the atom with its own radiation field. For an atom in its excited state and at distances from a mirror much less than the transition wavelength, the level shift will be dominated by the van der Waals interaction, whilst in the far field the level shift is attributed to the resonant interaction with its own reflected field [9–12]. Such far-field shifts have been observed with a beam of ^{138}Ba atoms traversing an optical resonator [13] and with atoms in a microwave cavity [14]. The same effect has been predicted for a single trapped ion whose emitted radiation field is reflected back by a single, distant mirror [15], and recently this level shift has been observed with an indirect spectroscopic method [16].

A mirror-induced energy shift of an excited state, like a modified spontaneous decay rate [6,17], is analogous to the effect observed in the case of a radiating antenna in front of the reflector, and can be treated in terms of radiation reaction only, i.e. in terms of the interaction with its own reflected field. The quantum electrodynamic picture is quite different though, due to the presence of the vacuum field which also couples to the atom [18]. The concept of the vacuum field forms the prevailing language in the field of experimental cavity QED, see for example Refs. [13, 14]. It was also used in the proposals to trap an atom in a resonator [26, 27] to which our experiment is closely related. Rigorously speaking, however, the vacuum field alone cannot account for spontaneous decay or its modification by reflectors, but the radiation reaction must also contribute [19–22]. The same is true for excited-state level shifts. In fact, the degree to which vacuum fields and radiation reaction are seen to contribute depends upon the ordering of operators in the Heisenberg equations of motion, the choice of which has been called a "matter of taste" [18]. In what follows in the present thesis work we will use the concept of vacuum fields as a convenient language but without insisting on any particular distinction between vacuum fields and radiation reaction.

The far-field mirror-induced shift of an excited atomic level oscillates on the wavelength scale when the atom-mirror distance is varied. Therefore, when the position of the atom is controlled to the extent that it becomes sensitive to this spatial dependence, then the level shift acts as a spatially varying potential $U(\vec{r})$, and the atom feels its gradient $-\vec{\nabla}U(\vec{r})$ as a force.

This mirror-induced force is a peculiar case of the mechanical effect of light. Forces due to applied light fields were first demonstrated experimentally by Lebedev [23], and the recoil of an absorbed photon on an atom was observed by Frisch who deflected an atomic beam with incoherent light [24]. With the advent of the laser, such forces have found many important applications, from decelerating, cooling and trapping atoms to optical tweezers in biology [25].

The use of mirror-induced forces on individual atoms was first considered in connection with cavity-QED experiments, and has been proposed to trap atoms in an optical resonator [26, 27]. A single, trapped and laser-excited ion is an ideal system for the observation of such forces, as its position can be controlled on the nanometer scale [6, 28, 29], and interaction with a distant mirror has already been demonstrated [6,16,17].

In this thesis we present different kind of experiments performed with a single Barium ion placed in front of a single mirror. The resonance fluorescence of the laser excited ion is collected with a high aperture objective and then reflected onto the ion with a mirror which is placed approximately 25 cm distant. The advantage of our setup is not only that it allows us to detect the effect of a mirror on the internal, electronic state of an ion, which is the first objective of this work, but it is also possible to measure the spectrum of the ion's motion with a high signal-to-noise ratio (of approximately 7 dB), which has not yet been achieved by performing RF spectral analysis of the resonance fluorescence. We hence achieve a fundamentally new level of control over the total state of the atom and of possibilities for its manipulation. The second objective of this work was to reveal directly the action of the reflected field on the ion's motional degree of freedom. The work belonging to the first objective [16] has implications in, for example, precision spectroscopy. Results from the second objective are important for applications of single ions in quantum information processing, where logic operations involve the coherent control of the vibrational motion in the trap [30–33]. Moreover, the ability to measure an ion's motion in real time allows us to set up a new class of experiments for motion control with the help of active feedback. The long term goal of these experiments could be control of the motional state of the ion on the quantum level, i.e. to reach the standard quantum limit for measurements [34].

The objective of the chapter of this thesis work concerning feedback was to show the ability of the frequency/phase control of the ion's oscillation with the feedback based on a phase-locking loop. Another goal was to introduce the electronic feedback cooling of the ion's motion based on a "cold damping" method [35], when a viscous force is applied in the direction of the ion's oscillations, therefore slowing it down. As has been recently demonstrated such a method can be used to cool down a vibrational mode of the mirror by factor of 40 (from 300 K to approximately 8 K) [36]. The thermal energy of the mirror's mode is almost four orders of magnitude larger than the energy of the vibrational quanta of that mode, which is about 0.1 mK, and hence it is still far from the case when a harmonic oscillator (the mirror mode) behaves quantum mechanically [37].

In the present work we demonstrate the experiment performed with a Doppler cooled single ion which is confined in a Paul trap. The thermal energy of the ion's oscillation is only 10-20 times larger than the energy of its vibrational quanta. Therefore we believe this is the first demonstration of the feedback cooling based on "cold damping" technique with a single particle at the quantum noise limit.

The thesis is structured as follows: Chapter 2 gives an overview of the experimental setup for trapping and detecting single $^{138}\mathrm{Ba}^{+}$ ions, it also presents experimental results obtained in an earlier interference experiment. A theoretical description of the radiation properties of a classical antenna and an atom in front of a mirror is given in Chapters 3 and 4. All types of level shifts for a two-level atom in front of the infinite, perfectly conducting mirror are given as well as a comparison between an atom and an antenna. Chapter 5 is devoted to the optical Bloch equation (OBE) formalism, which allows calculation of the steady-state solution of the atom-field Hamiltonian. Emphasis is given to the case when the frequency of the atomic transition and its decay rate are modified by the presence of the mirror and these new values are then incorporated into the OBEs resulting in a phase shift (correlation phase) between interference fringes and red modulation. Experimental results which belong to the first objective are presented in Chapter 6. These include measurements of the dependence of the correlation phase on the detuning of the red laser at different laser intensities. Chapter 7 is dedicated to the description of the interference method used to observe the motion of the ion directly in the spectrum of its resonance fluorescence. Spectra of motion are measured for different directions of the cooling beam. Measurements of the mirror-induced force on the single ion are presented in Chapter 8 and include spectra of the sideband for a different ion-mirror distances, measurements of the trap frequency shift at different directions of the cooling beam and dependence of the trap frequency shift on the excitation probability. Chapters 9 and 10 present recent experiments devoted to the control of the ion's motion with active feedback. These measurements present the optical reconstruction of the trajectory of the ion's macro-motion, phase-locking of the ion's motion to the primary signal generator and feedback cooling based on the "cold damping" technique.

2 Earlier experiments with a single Ba^+ ion

The core components of the experimental setup used throughout this thesis work were built by Ch. Raab and are mostly described in his PhD thesis [38]. A clear theoretical description of how Paul traps work can be found, for example, in [39, 40]. The laser setup is described in [41]. This chapter describes a single Ba^+ ion and the Paul trap used. Also the first interference experiment will be briefly described.

2.1 The $^{138}Ba^+$ ion

In our experiment we use a single $^{138}\mathrm{Ba}^+$ ion. The electron configuration of Ba^+ is similar to Xenon with an additional valence electron. The three energy levels $6S_{1/2}$, $6P_{1/2}$ and $5D_{3/2}$ of the Barium ion form a Λ-System. There are two allowed dipole transitions: the $P_{1/2}$ to $S_{1/2}$ channel with transition wavelength $\lambda_g = 493.409$ nm and natural linewidth $\Gamma_{green} = 15.1$ MHz, and the $P_{1/2}$ to $D_{3/2}$ channel with transition wavelength $\lambda_r = 649.691$ nm and natural linewidth $\Gamma_{red} = 5.3$ MHz. The $D_{3/2}$ to $S_{1/2}$ transition is dipole forbidden but quadrupole-allowed with a very narrow natural linewidth of approximately 2 mHz (80 seconds lifetime).

Since a $^{138}\mathrm{Ba}^+$ ion has no nuclear spin there is no hyperfine splitting of atomic levels. However, the presence of an external magnetic field of approximately 4.2 Gauss splits the energy levels into eight Zeeman components. In our experimental setup we work mainly with the σ^+ and σ^- components of the ion fluorescence, and because of the magnetic field, the laser beam direction and its linear polarization are mutually orthogonal. The relevant level structure of $^{138}\mathrm{Ba}^+$ with Zeeman components is shown in Fig. 2.1.

2.2 The Paul trap

For precision optical measurements, for example in interferometric experiments with single atoms or molecules one has to not only to slow them down but also to localize their position in free space with nanometer precision. These requirements are still difficult to fulfil in the case of a single neutral atom or a single molecule, but can be relatively easily achieved if trapped ions are used instead.

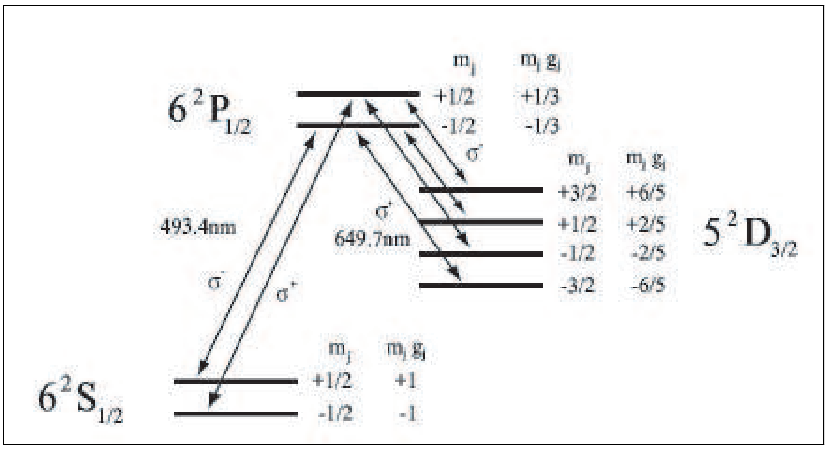

Figure 2.1: Level scheme for ^{138}Ba$^+$ used in the experiment. The dipole transitions with wavelength and polarization are indicated by arrows. The Zeeman substructure of the relevant Ba$^+$ levels is also shown.

Charged particles can be confined with the help of a Paul trap invented by W.Paul in 1958 [39]. The Paul trap forms a saddle-shaped quadrupole potential which is varied sinusoidally in time with drive frequency Ω_{drive}:

$$\Phi = (\alpha_x x^2 + \alpha_y y^2 + \alpha_z z^2)(V_o + U_o \cos(\Omega_{drive} t))$$

The sum of all coefficients α_i must be zero, i.e. $\alpha_x + \alpha_y + \alpha_z = 0$, as the spatial part of the trap potential obeys Laplace's equation. If the quadrupole potential is rotationally symmetric about the z-axis, then $\alpha_x = \alpha_y = -2\alpha_z$ and the motion of a single ion in each dimension becomes independent from the motion in other dimensions.

The one-dimensional equation of motion for a single ion is:

$$\ddot{x} + (a_x - 2q_x \cos(\frac{1}{2}\Omega_{drive} t))x = 0 \tag{2.1}$$

This equation is known as a Mathieu equation [42]. Parameters a_i and q_i depend on the trap geometry, the mass of the ion, the amplitude of the driving field and its frequency and are equal to

$$a_z = -2a_{x,y} = -\frac{8eV_o}{M_{Ba} r_o^2 \Omega_{drive}^2} \tag{2.2}$$

$$q_z = -2q_{x,y} = -\frac{4eU_o}{M_{Ba} r_o^2 \Omega_{drive}^2}, \tag{2.3}$$

where r_o is a radius of a trap.

The trap itself consists of a ring electrode with diameter of 1.4 mm and two end-cap electrodes which are placed along the symmetry axis of the ring, with a spacing of

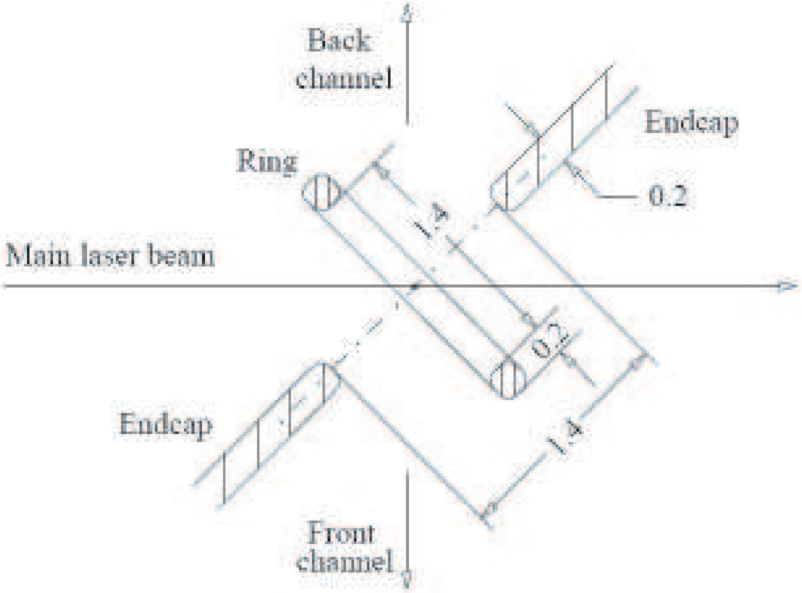

Figure 2.2: Design of the Paul trap and orientation with respect to the two detection channels and the direction of a main cooling beam (view from the top).

1.4 mm, see Fig. 2.2. The driving field, with a voltage up to 500 V at a frequency $\Omega_{drive} = 19.27$ MHz, is applied to the ring electrodes. The end-caps are grounded with respect to this ac field. Additional dc offset voltages are applied to the end caps for micro-motion compensation, see for details [38].

In this case the parameters a and q for all three axes are much smaller than 1, and the ion's motion can be approximated by the motion in an effective harmonic potential

$$\Phi_{eff}(\mathbf{r}) = \frac{|\nabla\Phi|^2}{4M_{Ba}\Omega_{drive}^2} = \frac{1}{2}M_{Ba}\omega_{trap}^2\mathbf{r}^2 \tag{2.4}$$

with trap frequency $\omega_{trap} \sim 1$ MHz. The radial symmetry of the trap is not perfect therefore the motion in the ring plane will have two frequencies, which are relatively close together (1 and 1.2 MHz). Oscillations in the direction of the end-caps have a frequency of approximately 2.2 MHz.

The energy of the ion motion in the trap can be reduced by means of laser cooling to an energy on the order of $\hbar\Gamma$. The ion motion can then be quantized, and we can estimate the width of the ground state wave function for a ^{138}Ba$^+$ ion in our trap: $\langle 0|x^2|0\rangle^{\frac{1}{2}} = \sqrt{\hbar/2M_{Ba}\omega_{trap}} \approx 6.3$ nm. This means that in principle, our atom can be localized in space with an accuracy much smaller than the fluorescence wavelength. In our experiment we use Doppler cooling to cool the motion of the ion in Paul trap. Doppler cooling of the three-level atom is a rather complicated theoretical problem – it is difficult to calculate analytically the cooling rate and the final thermal energy,

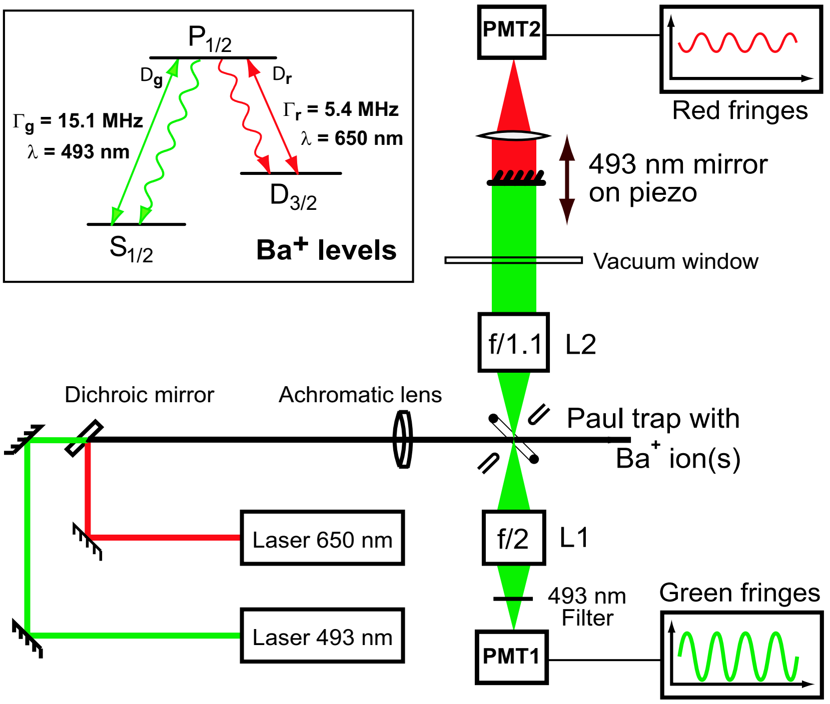

Figure 2.3: Setup of the interference experiment

therefore we use results calculated for the two level atom [43]. For optimal cooling conditions the ion's thermal energy is then equal to $\hbar\Gamma/2$, which corresponds to a mean phonon number of $\overline{n} \sim 10$. The size of the ion's wave packet is then

$$\langle \overline{n}|x^2|\overline{n}\rangle^{\frac{1}{2}} = \langle 0|x^2|0\rangle^{\frac{1}{2}}\sqrt{2\overline{n}+1} \approx 29\ nm \tag{2.5}$$

2.3 An initial interference experiment with a single Ba^+ ion

In this section we will describe the first interference experiment with a single $^{138}Ba^+$ ion and a distant mirror that was performed by our group, for further details see [6].

In the interference experiment, shown in Fig. 2.3, a single $^{138}Ba^+$ ion is held in a Paul trap and continuously excited and cooled by near-resonant lasers. Both lasers have linewidths below 100 kHz. The laser beams are combined on a dichroic mirror and focused into the trap. Both laser beams are linearly polarized and the intensities of the lasers are set to near saturation. The red laser (650 nm) is tuned close to resonance; the green laser (493 nm) is detuned by half of the transition linewidth $\Gamma_g/2$ for optimal Doppler cooling. A macroscope lens L2 (F$\sharp = 2$) collects part of the resonance fluorescence, the green photons of which are detected on PMT1 at count rates of around 15 × 10^3 cps. The resonance fluorescence emitted into the opposite direction is collimated by lens L1 (f-number 1.1, wavefront abberations $< \lambda/5$). The green part of this signal is retro-reflected by a piezo-adjustable plane mirror, while the red part is transmitted and detected on PMT2 at around 25 × 10^3 counts per second.

Lens L1, placed inside the vacuum chamber, and the retro-reflecting mirror are positioned about 25 cm away from the ion, are arranged such that they image the ion onto itself, i.e. the returning light is brought to a focus at the position of the ion. The ion and its mirror image can be observed visually through the macroscope. Overlapping the mirror image with the real ion leads to high-contrast interference fringes at PMT1 upon scanning the ion-mirror distance with a piezo actuator. Fine adjustment of the overlap is critical in obtaining high-contrast interference fringes. The green fringe contrast can be as high as 72%, limited by the optical set-up (mirror and window flatness, quality of L1), by the thermal motion of the ion [44], and by its micro-motion along the ion-mirror axis.

Simultaneously with the green signal on PMT1 we record on PMT2 the red fluorescence transmitted through the mirror, see Fig. 2.4. Varying the mirror-ion distance, which gives rise to the 493 nm fringes, also leads to the modulation of the red light with the same period. Note that this modulation is not due to interference at the red

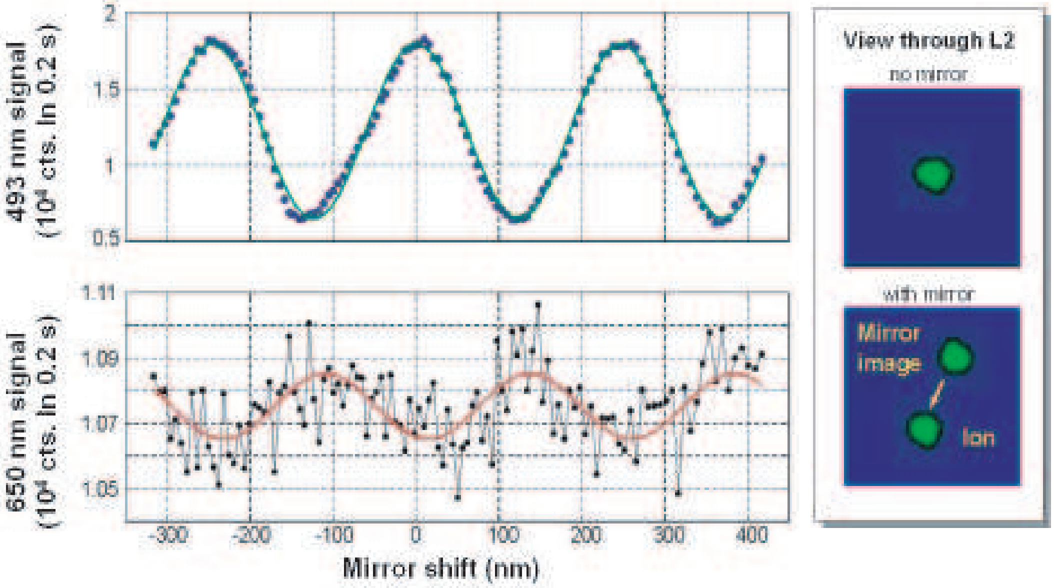

Figure 2.4: Left-hand-side picture: interference fringes at 493 nm and the simultaneously recorded fluorescence at 650 nm transmitted through the mirror on the left side. Right-hand-side picture: the view through the macroscope of an ion and its image

wavelength, because interference would lead to a different modulation period.

The red fringes occur due to the back-action of the mirror on the atom, i.e. the mirror modifies the vacuum field at the green wavelength and leads to enhancement and inhibition of spontaneous decay from the $P_{1/2}$ state. In the old interpretation one could expect that enhancement of spontaneous decay at 493 nm leads to increased depopulation of the upper state and consequently decreases the rate of detected 650 nm photons, while inhibited decay at 493 nm increases the 650 nm count rate.

However, by looking more carefully in Fig. 2.4 it is possible to see that there is a small phase difference between green interference fringes and red modulation fringes. This effect is due to a mirror-induced level shift of the $P_{1/2}$ state which depends on ion-mirror distance and this is one of the main topic of the present thesis work, and different experimental methods to measure this effect will be described in following chapters.

3 A classical antenna in front of a single distant mirror

It is well known that an atom can be modelled as a classical dipole or a dipole antenna [45, 49]. The radiation properties of this dipole change if a body which reflects radiation back to the dipole is brought into the vicinity [9]. There are two effects that appear: first the dipole will oscillate with a slightly different frequency, secondly the dipole's damping rate or the radiation linewidth will be altered. The magnitude of the effect depends on the distance between radiating dipole and reflector. In this chapter we will discuss classical electrodynamics of a radiating dipole in front of a reflector. The description will be limited to the a case of a perfectly reflecting wall, instead of that of a general reflector.

These effects have been known for a long time in classical radio-physics [46, 47]. The effects are widely used, for example, in directional and microwave antenna design, some principles of which will be outlined briefly as well.

3.1 Radiating dipole in free space

The simplest system which radiates electromagnetic waves is an oscillating point dipole. This is known as a Hertzian dipole, after H.R. Hertz who first calculated its electromagnetic field in 1888 [1]. The question: "How does a point dipole radiate in free space?" is very important because any radiating system can be imagined as a set of these elementary dipoles, hence a total field emitted by this system will be a superposition of fields from elementary dipoles.

The full theory of the Hertzian dipole can be found in [2, 48]. Here we will use two facts. The first fact is that radiated electromagnetic waves have the same frequency as the dipole's oscillation frequency. The second fact is that the oscillating dipole must loose kinetic energy because of the radiation it emits: the total radiated power averaged over the period of an oscillation of the dipole into a 4π solid angle being

$$S = \frac{2}{3}\frac{e^2}{c^3}\omega_0^4\overline{x^2} = \frac{1}{3}\frac{e^2}{c^3}\omega_0^4 x_0^2, \tag{3.1}$$

where ω_0 is the oscillation frequency of the dipole, x is the instantaneous position of the dipole and x_0 is the amplitude of the oscillations. The amount of radiated power is equal to the amount of kinetic energy which has been dissipated. This dissipation can be viewed as being induced by an external force arising from the radiation emission process, which slows the dipole's motion down, analogous to a friction or viscous force. In other words there is a force produced by the emitted radiation that acts on the dipole's motion. Hence there is *a reaction of the dipole to its own radiated field.* This self-reaction force is proportional to the second time derivative of the instantaneous speed of a charge (a rotating electron around nucleus in our case) and equals

$$\mathbf{F}_{SR} = \frac{2}{3}\frac{e^2}{c^3}\ddot{\mathbf{v}}. \tag{3.2}$$

This value for the force is correct when the emitted wavelength is larger than the classical electron radius:

$$\lambda = \frac{2\pi c}{\omega_o} \gg \frac{e^2}{mc^2} = r_0 \sim 3 \times 10^{-13} cm, \tag{3.3}$$

where m is the mass of an electron and r_0 is the classical electron radius.

Let us consider how the self-reaction force will change the motion of a dipole. If we were to set this force to zero the dipole would oscillate for an infinite amount of time with the same frequency. However, the radiation reaction is a damping mechanism for a dipole and will cause a broadening of the resonance line. The equation of motion is

$$m\ddot{\mathbf{r}} + m\omega_o^2\mathbf{r} = \frac{2}{3}\frac{e^2}{c^3}\ddot{\mathbf{v}}. \tag{3.4}$$

If condition given by Eq. 3.3 is fulfilled then the self-reaction force is much smaller than the restoring force of an oscillator. We can use a first order approximation for $\ddot{\mathbf{v}} = \dddot{\mathbf{x}} \approx -\omega_o^2\dot{\mathbf{x}}$, then the equation of motion for dipole motion is similar to the equation of a damped harmonic oscillator and we have

$$\ddot{\mathbf{r}} + \omega_o\gamma_o\dot{\mathbf{r}} + \omega_o^2\mathbf{r} = 0, \tag{3.5}$$

where γ_o is known as the natural linewidth of a dipole radiation and is equal to

$$\gamma_o = \frac{2}{3}\frac{e^2}{mc^3}\omega_o^2. \tag{3.6}$$

For the optical domain the natural linewidth is on the order of 100 MHz.

Now we can see that the reaction of a dipole to its own field leads to line broadening. There is a small oscillation frequency shift as well of order $\frac{\gamma_o^2}{\omega_o} \sim 1$ Hz. This shift is also known as a Bloch-Siegert shift for harmonic oscillators, but in most optical experiments it can be neglected, except for precision frequency standards or optical clocks.

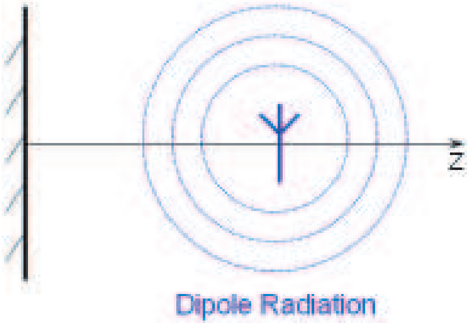

Figure 3.1: Radiating dipole drawn as antenna sitting in the vicinity of a perfectly conducting wall. The wall reflects part of the radiation back onto the dipole and causes an additional reaction force which drives or damps oscillations depending on the dipole-mirror distance z.

3.2 Radiative reaction of a dipole on retroreflected field

Let us consider how the radiation properties of dipole radiation will be changed if we bring a dipole close to a plane mirror, as shown in Fig. 3.1. We assume that the dipole is positioned at some finite distance z away from the mirror, the polarization of the dipole is also assumed to be parallel to the plane of the mirror. The equation of motion for this situation is the same as for the damped oscillator, see Eq. 3.5, but with the addition of an external force caused by the retroreflected field $\mathbf{E_{ref}}$:

$$\ddot{\mathbf{r}} + \omega_o \gamma_o \dot{\mathbf{r}} + \omega_o^2 \mathbf{r} = e\mathbf{E_{ref}}. \tag{3.7}$$

The right-hand-side of this equation can be represented as product of time dependent and z dependent functions, which yields:

$$\mathbf{E_{ref}} = e\mathbf{r(t)}k^3 W_{ref}(z), \tag{3.8}$$

where $k = \omega_o/c$ is the wave vector, and $W_{ref}(z)$ is the normalizing function, which depends on the radiation pattern of a dipole, the distance between the dipole and the mirror, and the geometry of the mirror (see [50]). In our case, for a plane and perfectly conducting mirror and for a vertically polarized dipole,

$$W_{ref}(z) = -e^{i2kz}\{\frac{1}{(2kz)} + \frac{i}{(2kz)^2} - \frac{1}{(2kz)^3}\}, \tag{3.9}$$

where z is the distance between mirror and dipole. The first term in this function corresponds to the dipole radiation in the far-field zone, while the last two terms belong to the instantaneous Coulomb interaction of the dipole with its image in the near-field zone. This expression for the normalizing function will be used later. Now let us rewrite Eq. 3.7 in a slightly different form

$$\ddot{\mathbf{r}} + \omega_o\gamma_o\dot{\mathbf{r}} + (\omega_o^2 + \frac{3}{2}\omega_o\gamma_o W_{ref}(z))\mathbf{r} = 0. \tag{3.10}$$

This is a main equation for determining the dipole evolution in the presence of a mirror. As can be seen from this equation the dipole will oscillate with a new or "perturbed" oscillation frequency Ω. To solve this equation we will use the following Ansatz:

$$\mathbf{r}(t) = \mathbf{r_o}e^{-i\Omega t}, \tag{3.11}$$

where Ω is the new oscillation frequency and $\mathbf{r_o}$ is the amplitude of the dipole's oscillations. Substituting this Ansatz into Eq. 3.10 we obtain the new frequency Ω of the dipole's oscillations

$$\Omega = \omega_o - \frac{i\gamma_o}{2} - \frac{\gamma_o^2}{2\omega_o} - \frac{3}{4}\gamma_o W_{ref}(z). \tag{3.12}$$

The first term in this equation is the unperturbed oscillation frequency. The second and third terms are the damping rate and the oscillation frequency shift due to the self-reaction. The self-reaction shift or Bloch-Siegert shift is usually neglected in the optical domain, as mentioned above. The last term corresponds to radiative reaction on the retroreflected field and can be separated into a shift of the oscillation frequency and a change of the damping rate.

In atomic physics, shifts of the oscillation frequency correspond to atomic level shifts, and the change of the damping rate corresponds to a modification of the spontaneous emission rate. The change of the damping rate is given by

$$\Delta\Gamma = \mathrm{Im}\{\frac{3}{4}\gamma_o W_{ref}(z)\}, \tag{3.13}$$

and the resonance frequency is shifted by

$$\Delta\Omega = \mathrm{Re}\{\frac{3}{4}\gamma_o W_{ref}(z)\}. \tag{3.14}$$

These two equations are solutions for the case of a single dipole in front of a perfectly conducting wall. It is possible to solve the task simply by taking the value for W_{ref} from Eq. 3.9 and substituting it directly into Eqs. 3.13 and 3.14, we then find the dipole damping rate change and the frequency shift as functions of the dipole-mirror distance:

$$\Delta\Gamma(z) = -\frac{3}{2}\gamma_o\{\frac{\sin 2kz}{2kz} + \frac{\cos 2kz}{(2kz)^2} - \frac{\sin 2kz}{(2kz)^3}\}, \tag{3.15}$$

$$\Delta\Omega(z) = \frac{3}{4}\gamma_o\{\frac{\cos 2kz}{2kz} - \frac{\sin 2kz}{(2kz)^2} - \frac{\cos 2kz}{(2kz)^3}\}, \tag{3.16}$$

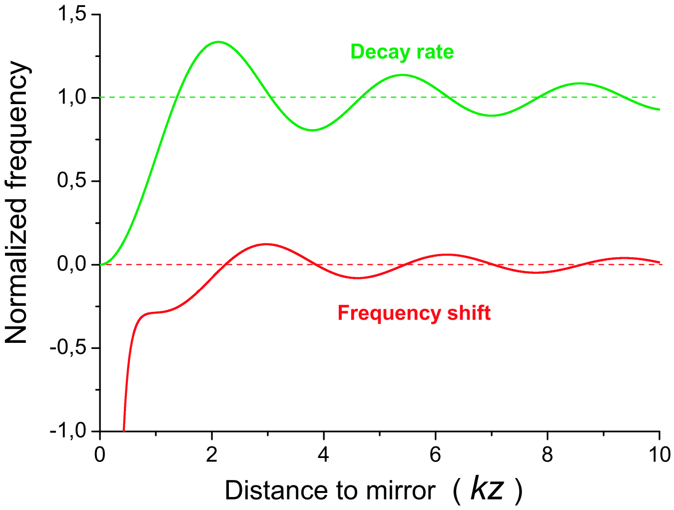

Figure 3.2: Decay rate of a classical dipole and resonance frequency shift normalized to the free-space value as a function of its distance to the mirror. The dipole is polarized parallel to the mirror (vertical polarization).

The dipole damping rate change and the frequency shift as a function of kz and normalized to the free space value are presented in Fig. 3.2. Let us consider two opposite cases. For $kz \ll \lambda$ or in the near field, the reflected field is 180° out of phase with the emitted field and they interfere destructively, hence the radiative decay rate of a dipole vanishes. This simply means that the dipole will not radiate in the horizontal direction. The frequency shift bends down due to attractive Coulomb interaction of a dipole towards its mirror image. In the case of an atom the attractive force towards the mirror surface would be treated as a van der Waals force.

For $kz \gg \lambda$ or in the far-field zone, the decay rate and the frequency shift apparently tend to the free space values which undergo oscillations with a spatial period of $\lambda/2$ with increasing z. The decay rate and frequency shift have a 90° phase shift with respect to each other. This effect is caused by a force created by the reflected field returning in phase or out of phase with the dipole oscillations.

3.3 Action of a lens

In our experimental setup there is a lens installed between the mirror and the single ion, see Fig. 3.3. By considering our experiment classically the single ion can be replaced by a radiating classical dipole. The lens collects a fraction $\varepsilon \approx 4\%$ of the emitted light and collimates it onto a mirror, positioned such that light is retro-reflected. The distance between the mirror and the dipole is less than $2\pi c/\gamma_o \approx 3$ m and therefore the light reflected back from the mirror is still coherent with the dipole's oscillation.

The focal distance of the lens is much larger than the wavelength, hence the light

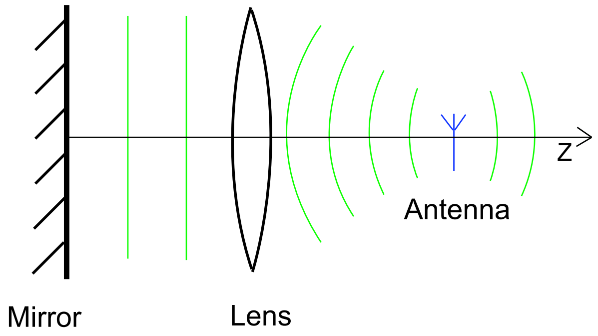

Figure 3.3: The dipole antenna sits at some distance z from the mirror. Part of the dipole radiation is collimated by the lens which subtends a solid angle ε and reflected back into antenna.

field radiated by the dipole can be regarded as a spherical wave, which is transformed to plane waves travelling onto the mirror and then subsequently reflected back. Neglecting some edge effects due to the finite aperture of the lens and the mirror, we can approximate the reflected field by a Gaussian beam. Since all our measurements are performed in the far-field, the beam goes through the focus and acquires an additional 90° optical phase (Guoy phase shift) with respect to the spherical wave, for details see [51].

The focusing action of the lens together with the Guoy phase shift cancels the near-field terms in Eq. 3.15, 3.16 and changes the phase of $1/2kz$ far-field term. Then for the new frequency and decay rate we get the following expressions:

$$\Gamma(z) = \gamma_o - \frac{3}{2}\gamma_o \varepsilon \sin(2kz), \tag{3.17}$$

$$\Omega(z) = \omega_o - \frac{3}{4}\gamma_o \varepsilon \cos(2kz), \tag{3.18}$$

where ε is the solid angle subtended by the lens. Here it is important to point out that this result is valid only if the dipole sits in the focal point of the lens. If the distance between the dipole and the focal point is more than one Rayleigh length of the focused beam, the reflected beam will have a smaller amplitude and a different phase, resulting in a decreased damping rate change and a decreased frequency shift.

A similar result, to within numerical coefficients $\frac{3}{2}$ and $\frac{3}{4}$ before the oscillation terms in Eqs. 3.17 and 3.18, was derived by Uwe Dorner et. al. [15]. In that work the authors performed calculations for the level shift and modified spontaneous emission rate of an atom in the presence of a mirror, using the theoretical framework of quantum optics. Here we would like to emphasize again that these are well known Cavity QED effects, i.e. inhibited and enhanced spontaneous decay and the energy shift of an excited level are already present in classical electrodynamics and are widely used for example in

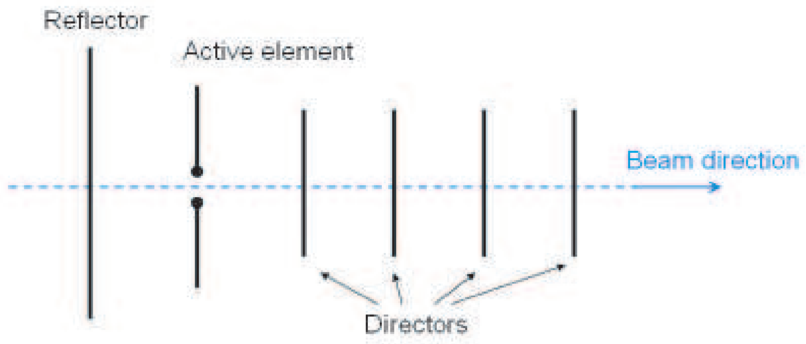

Figure 3.4: A Yagi-Uda antenna with one reflector and four directors. One often sees this type of antenna on the roofs of houses.

design of antenna array, such as Yagi-Uda antenna or directive short wave antenna, which has been invented by Shintaro Uda (1924, Japan), see for details [52].

3.4 Directive antennas and an atom inside the cavity

A directive antenna [4, 52] consists of an active element, usually a quarter-wavelength dipole, a reflector which sits behind the active element and which is a bit longer than the dipole, and an array of directors, for example see Fig. 3.4. The array of directors serves to create a particular emission pattern or emission diagram of an antenna.

A current is fed to only the active element, the other elements have a radiative excitation from that element, and the phase of that excitation is determined by the spacing between the elements and their length. It is well known that an element which is a bit longer than half a wave length at the right spacing will act as a reflector. An element which is shorter than half a wave length will reinforce the field travelling away, so this element acts as director and forms a beam, see [4].

Let us compare the emission diagram of a directive antenna with four directors with the emission diagram of a dipole antenna in free space. As one can see from the Fig. 3.5, the emission diagram of the antenna is completely different from the radiating dipole in free space. A beam appears due to the interference of several effective dipole emitters.

If we were to describe this effect in terms of decay rate we would say the decay rate of a dipole is altered when it is placed inside an antenna array structure. The resonance frequency of the antenna would be shifted as well.

The radiative properties of a directive antenna are analogous to the radiative properties of atom in a cavity or in front of a single mirror, but not completely. Although an atom in a cavity has inhibited and enhanced spontaneous emission and shifts of its levels in a cavity or even in the presence of a single mirror, to make a proper description of the atomic evolution and its radiation properties one must use the framework

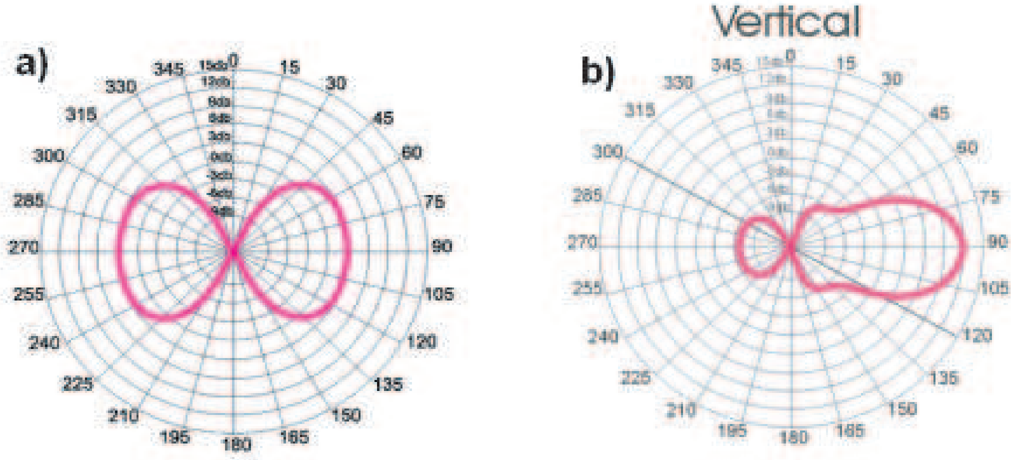

Figure 3.5: Figure a) is an emission diagram of dipole in free space. Figure b) is an emission diagram of Yagi-Uda antenna with four directors.

of quantum electrodynamics. This will be the main topic of the next chapter.

4 An atom in front of a single distant mirror

In the previous chapter the radiative properties of an antenna located in front of a perfectly conducting mirror was described. There the atom was approximated as a dipole antenna and the electromagnetic field emitted by the dipole was also treated classically. Under those assumptions two main effects appear: modification of the damping rate and a shift of the dipole's oscillation frequency.

In this chapter we will use a quantum-mechanical description of an atom coupled to the electromagnetic field. The full treatment of that task can be found in [11, 12, 50].

The radiative decay is an irreversible process and can be described using perturbation theory [53]. According to Fermi's golden rule [54], the decay rate of an excited atomic state is proportional to the density of the electromagnetic modes around the resonance frequencies, while a radiative level shift or Lamb shift [55, 57], coming from the absorption and emission of virtual photons across, potentially, the whole electromagnetic spectrum contributes to an energy shift of mainly the ground state. In other words, the Lamb shift comes from a coupling of a bound electron to the vacuum field.

In our experiment we observe a shift in energy of an excited state which is induced by a single distant mirror. In the framework of QED this level shift can be treated as being partially caused by the mirror modified vacuum field and partially by radiative reaction. The latter effect of radiation reaction is strongly analogous to the case of an antenna in front of a mirror.

4.1 Atom-field interactions in the dipole approximation

4.1.1 Field description

The quantized electromagnetic field is described by the vector potential $\mathbf{A}(\mathbf{r}, t)$ [58], which can be expanded over a set of transverse mode functions $\mathbf{A}(\mathbf{r})$ with angular frequencies ω_k

$$\mathbf{A}(\mathbf{r}, t) = \sum_{\omega_k} (\frac{2\pi\hbar c^2}{\omega_k})[a e^{-i\omega_k t}\mathbf{A}(\mathbf{r}) + a^+ e^{i\omega_k t}\mathbf{A}^*(\mathbf{r})], \tag{4.1}$$

where a and a^+ are the lowering and raising operators respectively. The mode functions $\mathbf{A}(\mathbf{r})$ form an orthonormal set and are the ordinary solutions of the Helmholtz equation

$$\nabla^2\mathbf{A}(\mathbf{r}) + k^2\mathbf{A}(\mathbf{r}) = 0. \tag{4.2}$$

Under these considerations the Hamiltonian of the electromagnetic field will be $H = \sum_{\omega_k} \hbar\omega(a^+a+\frac{1}{2})$, and by knowing the state of the electromagnetic field we can calculate the expectation value of any field operator. For example, for the vacuum state the mean electric field is $\langle\mathbf{E}(\mathbf{r},t)\rangle = 0$, whereas $\langle\mathbf{E}^2(\mathbf{r},t)\rangle \neq 0$. Now let us suppose that the field is in some state with a certain photon number $|n\rangle$. The intensity of the electromagnetic field is then

$$\langle I\rangle = \langle\mathbf{E}^2(\mathbf{r},t)\rangle = 4\pi\hbar\omega|\mathbf{A}(\mathbf{r})|^2 n + \langle\mathbf{E}^2(\mathbf{r})_{vac}\rangle. \tag{4.3}$$

The first term in the Eq. 4.3 is the intensity of the n-photon field. It is interesting to note that the vector potential $\mathbf{A}(\mathbf{r})$ plays the role of the wave-function here. The square of its magnitude is proportional to the probability of finding a photon in a given volume which is on the order of λ^3 at a given point in a space. The last term describes the energy of the vacuum fluctuations, and simply means that the electromagnetic field has an energy even if there are no photons in it.

The vacuum field plays a major role in QED and some of the effects, such as the Casimir force [8], the Lamb shift [55] and the anomalous magnetic moment of an electron [56] can be treated as being caused by this field alone. For example the Lamb shift can be calculated as a Stark shift of atomic levels due to the field associated with vacuum fluctuations [18, 61]. The theory which describes spontaneous emission of an atom becomes mathematically inconsistent without the use of the vacuum fluctuations, because vacuum terms preserve commutation rules [18]!

4.1.2 Atom-field interactions

We consider an atom coupled to the quantized electromagnetic field. In the non-relativistic case and in dipole approximation, i.e. the magnitude of the field does not change over the size of an atom, and by using the Coulomb gauge for the total Hamiltonian of the system [59], the Hamiltonian can be split into atomic, field and interaction parts:

$$H_{tot} = H_{atom} + H_{field} + H_{int}. \tag{4.4}$$

The atomic part is:

$$H_{atom} = \frac{p^2}{2m} + U(\mathbf{r}_e), \tag{4.5}$$

where p is the momentum of an electron, $\mathbf{r}_e$ is its coordinate and $U(\mathbf{r}_e)$ describes the Coulomb attraction of an electron by the nucleus of an atom. The field Hamiltonian is exactly the same as in the previous section

$$H_{field} = \sum_{\mathbf{k},\varepsilon} \hbar\omega(a^+a + \frac{1}{2}), \tag{4.6}$$

where the sum is taken over all available modes of the electromagnetic field with wave vector $\mathbf{k}$ and with polarization vector ε. The interaction part will be

$$H_{int} = \frac{\varepsilon_0}{2} \int E^2_{inst}(\mathbf{r}_a) d^3r + \frac{e^2}{2mc^2} A^2(\mathbf{r}_a) - \frac{e}{mc} \mathbf{A}(\mathbf{r}_a) \cdot \mathbf{p}_a, \tag{4.7}$$

where $\mathbf{r}_a$ is the position of an atom in space and $\mathbf{p}_a$ is its momentum and $E_{inst}(\mathbf{r}_a)$ is the instantaneous magnitude of the electric field at the atomic position. The first term in the interaction part describes the instantaneous Coulomb interaction of an electron with some external field, the second part can be treated as the kinetic energy of an electron acquired from the action of the vacuum field. The third part represents the dipole interaction of an atom with an external transverse electromagnetic field.

Perturbation theory can now be used to calculate the spontaneous decay rate and level shift. Our starting point will be the eigenfunctions of the atomic Hamiltonian $|j\rangle$, where the ground state of an atom will be denoted by $|g\rangle$ and the excited state by $|e\rangle$. The field state $|0\rangle$ is a vacuum state and the state $|\mathbf{k}\rangle$ is the one-photon field, with wave vector $\mathbf{k}$.

The decay rate can be computed using Fermi's golden rule [54,60], and ignoring the first and second terms in the interaction Hamiltonian (see Eq. 4.7), as they contain either only field or only atomic variables and therefore cannot change the state of an atom or the field during a dipole transition, we obtain

$$\Gamma = -\frac{2\pi}{\hbar^2} \frac{e}{mc} \sum_{\mathbf{k},\varepsilon} |\langle g, \mathbf{k}|\mathbf{A}(\mathbf{r}_a) \cdot \mathbf{p}_a|e, 0\rangle|^2 \delta(\omega_a - \omega_{\mathbf{k}}). \tag{4.8}$$

Here, the spontaneous decay takes place between states $|e\rangle$ and $|g\rangle$ of an atom with frequency ω_a.

To calculate the radiative level shift, let us consider an atom in state $|a\rangle$ in the vacuum. The total shift will be a combination of first and second order perturbation shifts. The first order shift comes from the first and second terms in the interaction Hamiltonian and will be

$$\Delta_{inst} = \frac{\varepsilon_0}{2} \int E^2_{inst}(\mathbf{r}_a) d^3r, \tag{4.9}$$

from the first term, and

$$\Delta_{vac} = \frac{e^2}{2mc^2} \sum_{\mathbf{k},\varepsilon} \langle 0|A^2(\mathbf{k}, \mathbf{r})|0\rangle, \tag{4.10}$$

from the second term.

The last term of the interaction Hamiltonian will contribute to the second order level shift and gives

$$\Delta_2 = \frac{e^2}{mc^2} \sum_j \sum_{\mathbf{k},\varepsilon} \frac{|\langle a, 0|\mathbf{A}(\mathbf{k}, \mathbf{r}) \cdot \mathbf{p}|j, \mathbf{k}\rangle|^2}{E_a - E_j - \hbar\omega_k}. \tag{4.11}$$

All these contributions to the total level shift are infinite. The term Δ_{inst} diverges because the Coulomb energy becomes infinite at the center of an electron. The terms Δ_{vac} and Δ_2 become infinite because the sum over the field modes $\sum_k A^2(\mathbf{k}, r)$ diverges as ω_k^2. However, this description turns out to be incorrect, because if an electron or an atom obtains relativistic momentum, the mass of the particle will also be increased as well. All physical variables calculated in perturbation theory are inversely proportional to the mass, hence the total contribution from relativistic terms can simply be ignored [61].

In other words, from the diverging integrals which represent any physical variables we have to subtract the energy of the free electron, and then the total value becomes convergent. This procedure is called mass and charge renormalization and is well described in the textbooks [18, 62].

4.2 Spontaneous decay rate modification by a perfectly conducting wall

Modification of spontaneous emission in the optical domain has already been observed in Eu^{3+} ions on dielectric substrates of different thicknesses deposited on a silver mirror [63]. In the present section we will consider the single atom sitting in front of a perfectly conducting wall. This task is similar to the one described in Chapter 3. Let us assume also that the distance from the atom to the wall is less than c/Γ or the coherence length of the field emitted by an atom. The polarization of the atomic dipole is vertical. The atom has only two levels: ground state $|g\rangle$ and excited state $|e\rangle$.

The decay rate of an atom can be calculated using Fermi's golden rule, given by Formula 4.8. In the case of a dipole transition we obtain

$$\Gamma(z) = \frac{\pi}{\hbar} |\mathbf{A}(\mathbf{z}) \cdot \mathbf{d}_{12}|^2 \rho(\omega), \tag{4.12}$$

where $\mathbf{A}(\mathbf{z})$ is the wave function of a photon in the final state, i.e. after emission, $\mathbf{d}_{12}$ is the matrix element of the dipole moment operator and $\rho(\omega)$ is the density of the final states. It has been shown in [64], that in the absence of losses, both quantum-mechanical and classical approaches yield the same answer, as for the case of an antenna in front of a wall (see Eq. 3.15), and the decay rate is given by

$$\Gamma(z) = \Gamma_o - \frac{3}{2}\Gamma_o \{ \frac{\sin 2kz}{2kz} + \frac{\cos 2kz}{(2kz)^2} - \frac{\sin 2kz}{(2kz)^3} \}, \tag{4.13}$$

where Γ_o is the spontaneous decay rate of an atom in free space.

This really implies that the modification of spontaneous emission of an atom in front of a reflecting wall can be explained either in terms of the radiative reaction on the retroreflected field or in terms of the coupling of an atomic dipole to the modified vacuum modes. This is one of the "puzzles" of QED, where a real physical effect may have several interpretations leading to the same numerical answer. Detailed analysis of that problem can be found, for example, in articles [19–21,66]. The manifestation of the quantum vacuum is beyond the scope of this thesis. However, I will briefly discuss the different interpretations, and the confusions they can cause, in the following chapters.

4.3 Level shift induced by a perfectly conducting wall

Let us now calculate the radiative level shifts of an excited two-level atom placed in front of a perfectly reflecting wall and whose dipole moment is parallel to the mirror. The level shifts are calculated with perturbation theory using Eq. 4.11. The total expression for the radiative shift in the dipole approximation can be found in [11,67]. We will consider only two limiting cases: when the atom sits in the near-field zone, i.e. $z < \lambda/10$, and when it sits in the far-field zone, i.e. $z > \lambda/10$, see for details [22].

4.3.1 Ground-state level shifts

The ground state shift in the near-field zone ($kz \ll 1$) arises from the van der Waals potential and is given by:

$$\Delta_g = -\frac{3\hbar}{64(kz)^3}\Gamma_o. \tag{4.14}$$

This level shift can be understood as arising from the instantaneous Coulomb interaction of the dipole moment of an atom with its mirror image.

When the atom is placed further away from a mirror, i.e. in the far-field zone, the ground-state level shift will be induced by the Casimir-Polder interaction, which results from a modification of the vacuum field by a conducting wall. In that case the ground state shift is [22]:

$$\Delta_g = -\frac{3\hbar}{16\pi(kz)^4}\Gamma_o. \tag{4.15}$$

The Casimir-Polder shift can be interpreted as a modification of the Lamb shift [11], since in the presence of a mirror, modification of vacuum fluctuations causes a change in the Bethe contribution to the Lamb shift of the atomic ground state [57].

These level shifts are both negative, hence an atom which sits in the ground state is attracted to the mirror.

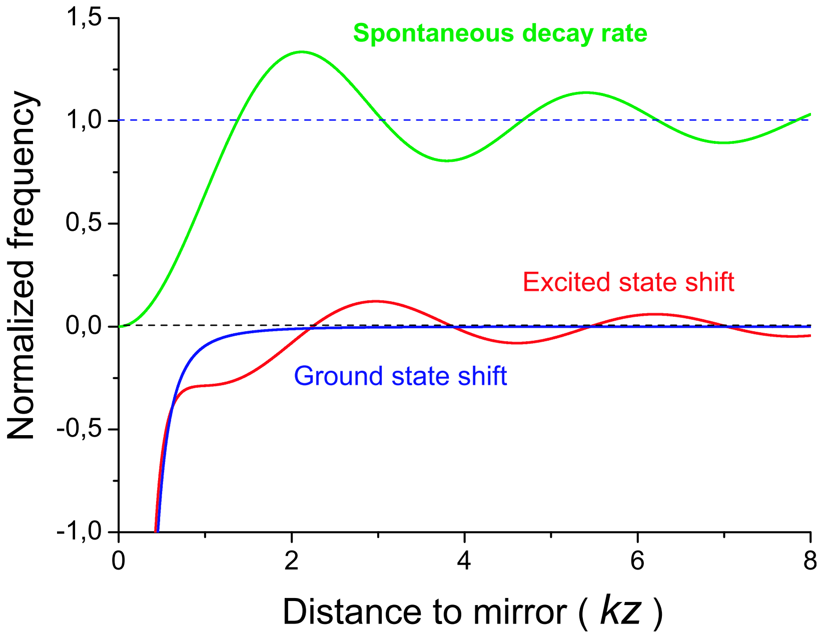

Figure 4.1: Decay rate (upper line) of an atom and its radiative level (red and blue lines) shifts normalized to the free-space emission decay rate Γ_o as a function of its distance to the mirror. The red line corresponds to the excited state, the blue one to the ground state.

4.3.2 Excited-state level shifts

In the near field zone, the oscillating dipole moment of an atom "sees" its image and is attracted to it. As for the ground state atom in the near field the excited level shift will be due to the van der Waals interaction, and is given by

$$\Delta_e = -\frac{3\hbar}{64(kz)^3}\Gamma_o. \tag{4.16}$$

Here it is important to note that there is no total change in the resonance frequency of an atom. This is valid, of course, only for an "ideal" two-level atom. Real atoms have more levels, and do not reveal this feature. At large distances an excited-state level shift will be dominated by the interaction of an atom with its own retroreflected field. The behavior is similar to that of an antenna, and the level shift is given by

$$\Delta_e = -\frac{3\hbar}{4}\frac{\cos(2kz)}{2kz}\Gamma_o. \tag{4.17}$$

More precisely this far-field oscillating shift may be interpreted as the radiation reaction from the retroreflected field and modified vacuum fluctuations [11]. It is important to add here that this level shift cannot be attributed to the action of the vacuum field alone [18].

Actually, there is a Lamb shift for excited levels as well [49]. Although it has a positive sign, it is much smaller (by a factor of at least 10^{-3}) than the Lamb shift for ground states. Therefore the contribution to the shift of the excited level due to the Casimir-Polder attraction is negligible, compared to that of the ground state.

Level shifts and decay rate in units of Γ_o of an atom in front of a perfectly conducting wall are shown in Fig. 4.1 as a function of kz. Three physically different potentials emerge that affect both the ground state and the excited state [22]. These are the van der Waals [7], the Casimir-Polder [8] and resonant-radiative potentials [13]. It can be seen also that the level shift of an excited state as well as the decay rate in the far-field zone reveals the properties of a radiating dipole antenna in front of the wall, see Fig. 3.2.

One possible interpretation of this effect would be that of the radiative reaction of the excited atom with its own retroreflected electromagnetic field. This effect is completely analogous to the case of an antenna and has been already described in the section 3.2.

The shift of the ground state in the far-field zone, which falls as $1/z^4$, can be treated as the interaction of an atom with spontaneously polarized dipoles on the surface of the wall [65].

In our experimental setup a lens is placed between the atom and the mirror. That lens collects the fluorescence of the atom and focuses it back. The van der Waals and Casimir-Polder contributions to the ground and excited level shifts vanish in our case because of the large distance (in the experimental setup the mirror is about 25 cm from the atom). This is why the modification of the spontaneous decay rate and the level shift of the excited state will be due to only the radiative reaction on the back-reflected field, and they behavior will be similar to the case of the classical dipole in front of a mirror, see section 3.3.

4.4 1D theory of the excited state level shift modified by a mirror

In the article [15] authors considered theoretically a system which modelled our experimental setup, where a small part $\varepsilon \approx 4\%$ of the light emitted from a laser excited Ba^+ ion is collimated by the lens and then retroreflected by the mirror towards the ion.

They calculated the spontaneous decay rate modification and the excited level shift of a two-level atom in front of a single mirror using perturbation theory for an atomic Hamiltonian in the rotating wave approximation. The quantized field modes which were used in that model are solutions of homogeneous 1-D Maxwell equations.

The modified decay rate and the atomic detuning from resonance (equivalent to the level shift) will be

$$\Gamma(z) = \Gamma_o - \varepsilon\Gamma_o \cos(2kz), \tag{4.18}$$

$$\Delta(z) = \Delta_o - \varepsilon \frac{\Gamma_o}{2} \sin(2kz). \tag{4.19}$$

It can easily be seen that the answer which is derived in [15] differs by a factor of 3/2 from Equations 3.17 and 3.18, which are derived for the case of an classical dipole in front of a mirror. It would be very interesting to perform an experiment to measure the absolute magnitude of the effect and to compare the calculations for an antenna and an atom.

As seen from Equations 4.18 and 4.19 the modified decay rate and the modified level shift depend only on ε and the ion mirror-distance, but do not depend on the intensities of the exciting lasers. This is actually a consequence of the radiative reaction as in the case of an antenna, but it can not be a sufficient argument for the action of the modified vacuum field!

What is also interesting about their work, is that they succeeded in computing the atomic evolution and field evolution in such a system, in the case when the atom-mirror distance is much larger then the coherence length of the fluorescence, i.e. $z \gg c/\Gamma$ and they even make numerical simulations for the intermediate case, when the atom-mirror distance is of the order of the coherence length of an emitted photon.

The new decay rate and detuning can be substituted into the optical Bloch equations to calculate steady state atom variables, such as population of an excited level.

5 The modified Bloch equations

The shift of an excited level together with the modified spontaneous decay rate results in a change of the resonance lineshape, which is impossible to measure directly from the spectrum of resonance fluorescence. The indirect spectroscopic method used in our experiment was to measure a phase shift between the green interference fringes and the red fringes (correlation phase), which depends on the intensities of the green and red lasers and their detunings.

The levels of $^{138}\mathrm{Ba}^+$ ion form a Λ-system, as shown in Fig. 2.1. The evolution of such a system under laser excitation is described by the optical Bloch equations (OBE), see, for example [69, 70]. The OBE in our case are derived from the master equation for an 8-level atomic density operator [68] describing the internal dynamics of a laser driven atom with dissipative processes such as spontaneous emission. The excitation spectra can be calculated numerically and are used to fit experimental data.

The back action of a mirror can be incorporated into the OBE by taking into account the modified spontaneous emission rate and the level shift from Equations 4.18 and 4.19. The phase shift between red and green fringes can then be calculated numerically.

5.1 The optical Bloch equations

Let us consider a single three-level atom interacting with two laser beams, as seen in Fig. 5.1. Rabi frequencies are defined using the matrix element for the dipole moment of each transition

$$\Omega_g = \frac{\mathbf{d}_{PS}\mathbf{E}_g}{\hbar} \tag{5.1}$$

$$\Omega_r = \frac{\mathbf{d}_{PD}\mathbf{E}_r}{\hbar} \tag{5.2}$$

The intensities of both lasers are quite high, i.e. the Rabi frequency is on the order of the spontaneous decay rate, hence the laser fields can be treated as classical electromagnetic waves $\mathbf{E}_g\sin(\omega_g t)$ and $\mathbf{E}_r\sin(\omega_r t)$ with spectral widths $\delta\omega_g$ and $\delta\omega_r$.

The atomic Hamiltonian in the basis of atomic states $|S\rangle$, $|P\rangle$, $|D\rangle$ is defined by

$$H_{atom} = \sum_i \hbar\omega_i |i\rangle\langle i|, \tag{5.3}$$

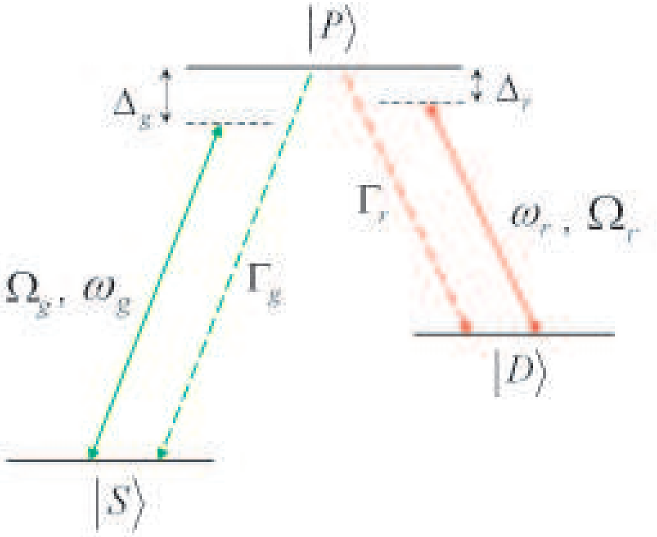

Figure 5.1: Three-level atom with eigenstates $|S\rangle$, $|P\rangle$, $|D\rangle$, laser fields $\mathbf{E}_g$ and $\mathbf{E}_r$, Rabi frequencies Ω_g and Ω_r, green and red laser detunings Δ_g and Δ_r.

where i=S, P, D. Assuming a dipole interaction between the atom and the laser fields we can write the total Hamiltonian using the rotating wave approximation (RWA), in matrix form in the same basis as the atomic Hamiltonian [71, 72]

$$H = H_{atom} + H_{int} = \hbar \begin{pmatrix} \omega_{SP} & \frac{\Omega_g}{2} e^{+i\omega_g t} & 0 \\ \frac{\Omega_g}{2} e^{+i\omega_g t} & 0 & \frac{\Omega_r}{2} e^{+i\omega_r t} \\ 0 & \frac{\Omega_r}{2} e^{+i\omega_r t} & \omega_{PD} \end{pmatrix} . \tag{5.4}$$

Although this Hamiltonian does not describe dissipative processes, such as spontaneous decay from the P-level to S- and D-levels, the spontaneous decay can be invoked as an interaction of an atomic dipole with the vacuum field. To follow this approach one must use the quantized field in the description instead of classical fields, see subsection 4.1.1.

By following a different approach the spontaneous decay rate and finite laser frequency width can be introduced as dissipation mechanisms due to the coupling of an atom to the infinite number of vacuum electromagnetic modes, or, in other words, as a connection to the external heat-bath. In that case the atomic states are no longer pure states, and the system is described with a density operator $\hat{\rho}$ written as

$$\hat{\rho} = \sum_{i,j=S,P,D} \rho_{ij} |i\rangle\langle j|. \tag{5.5}$$

The diagonal elements of the density operator $\langle i|\rho|i\rangle$ are the probabilities of finding an atom in state $|i\rangle$. For example, in our experiment the intensity of the fluorescence (or scattered) light is proportional to the probability of being in the excited state, and is calculated as

$$P_e = \langle P|\hat{\rho}|P\rangle = \rho_{pp}. \tag{5.6}$$

The equation of motion for the atomic density operator obeys the Liouville equation [73],

$$\frac{d\hat{\rho}}{dt} = -\frac{i}{\hbar}[H, \hat{\rho}] + L_{damp}(\hat{\rho}). \tag{5.7}$$

where the first term corresponds to the Schrödinger equation and L_{damp} describes dissipative processes due to the spontaneous decay of the upper state. The operator L_{damp} has the following general form

$$L_{damp}(\rho) = -\frac{1}{2}\sum_m C_m^+ C_m \rho + \rho C_m^+ C_m - 2C_m \rho C_m^+, \tag{5.8}$$

where the operators C_m describe different dissipation mechanisms. In particular, spontaneous decay is described by $C = \sqrt{\Gamma}\sigma^-$. The operator σ^- is a lowering operator and denotes the transition from the upper level into the lower one. Also, decoherence due to the finite laser linewidth can be included in L_{damp}, and is given by $C = \sqrt{2\delta\omega_i}|i\rangle\langle i|$.

Equation 5.8 can be transformed into a system of linear equations [72]. These linear equations are known as the optical Bloch equations. Steady-state solutions of the density matrix $\rho(\infty)$ can be calculated numerically from these linear equations.

5.2 Excitation spectra

The three-level atom description which has been described in the previous section can be expanded into an 8-level model to calculate the evolution and steady state level populations of a real atom [68], where the three original levels are now split into 8 levels due to the presence of the magnetic field.

An excitation spectrum is a record of fluorescence intensity versus the detuning of the green or red laser. The intensity of the red or green fluorescence can be calculated from the formulae

$$N_g = \Gamma_g \rho_{pp}, \tag{5.9}$$

and

$$N_r = \Gamma_r \rho_{pp}. \tag{5.10}$$

The fluorescence light is measured with a photo-multiplier tube. By choosing a color filter we are able to measure the intensity at a selected wavelength. The population ρ_{pp} for any set of parameters is a steady state solution of the OBE and can be used to fit experimental spectra, see for example Fig. 5.2.

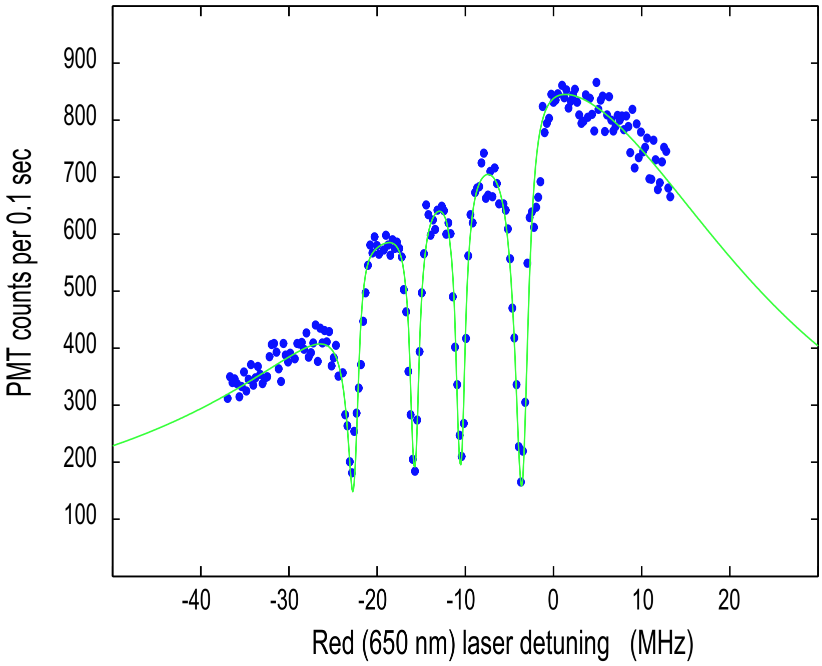

Figure 5.2: Excitation spectrum of resonance fluorescence (blue circles) at 493 nm. Fit of the 8-level OBE (green line) to the experimental data with parameters: Δ_g = – 13.15 MHz, S_g = 0.35, S_r = 1.36, $\delta\omega$ = 50 kHz, u = 4.34 MHz, α = 90°.

As expected, the spectrum of resonance fluorescence has a Lorentzian shape with four notches on it. These notches are known as dark resonances and appear when detunings of the green and red laser coincide and the atom is optically pumped into a superposition of the S and D states. Then the atom simply does not "see" the light.

The fit of the OBE's to the experimental data enables the determination of a set of parameters [68], namely: the saturation parameters of the green and the red lasers ($S = \frac{\Omega}{\Gamma}$), the detunings of the lasers relative to the atomic Bohr frequency ($\Delta = \omega_{laser} - \omega_{atom}$), the Zeeman splitting ($u = 0.14\frac{MHz}{G} \times B$), the line-widths of lasers $\delta\omega$ and the angle α between magnetic field and the polarization of the light fields.

5.3 Correlation phase

In our experimental setup, as seen in Fig. 2.3, a single mirror reflects a part of the resonance fluorescence inducing a shift of the upper level together with a change of the decay rate. Unfortunately, it is not possible to measure level shifts on the order of several hundreds of kHz from spectra like that shown in Fig. 5.2 due to relatively low (for this type of measurement) signal-to-noise ratio. Note, dark resonances remain

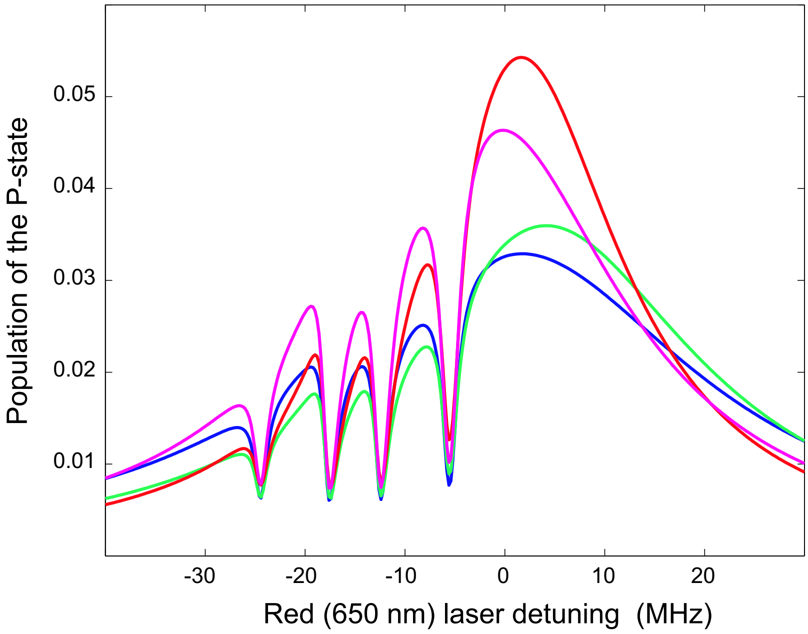

Figure 5.3: Modified excitation spectra at different ion-mirror distances, when $2kz = 0$ (red line), $\pi/2$ (green line), π (blue line), $3\pi/2$ (magenta line). Parameters are $\varepsilon = 0.4$, $\Delta_g = –15$ MHz, $S_g = 0.5$, $S_r = 1$, $\delta_l = 50$ kHz, $\alpha = 90°$.

at the same position in the excitation spectrum, regardless of the ion-mirror distance because of their dependence on only the frequency difference between the red and the green lasers. Of course, these dark resonance are much narrower than the line itself and, perhaps, may be used in other precision optical experiments.

However, there is another way to make a more sensitive detection of the excited level shift induced by a mirror. This level shift will change the detuning of both lasers with respect to the atomic resonance, and the spontaneous decay rate on the green channel will also be modified. The new detunings and spontaneous decay rate depend on the ion-mirror distance and are

$$\Gamma_g \longrightarrow \Gamma_g - \varepsilon \Gamma_g \cos(2kz), \tag{5.11}$$

$$\Delta_{g,r} \longrightarrow \Delta_{g,r} - (\varepsilon \Gamma_g/2) \sin(2kz). \tag{5.12}$$

The modified detunings and decay rate can be incorporated into the Bloch equations. The calculated excitation spectra versus detuning of the red laser and at different ion-mirror distances are shown in Fig. 5.3. In this figure the value of ε is chosen to be large (10 times more than the real experimental value) just to show the effect. As can be seen from these spectra, the excited state population has a non-trivial dependence on ion-mirror distance. Depending on the ion-mirror distance the resonance will take a different position across the detuning axis, and together with linewidth broadening or narrowing it causes a phase difference between the phase of the green interference and the population of the P-state, ρ_{pp}. In other words, if we would measure simultaneously the intensities of the green and red channels while scanning the ion-mirror distance, as it is described in section 2.3, and the detunings of both lasers would be fixed, we would see that the phase of the green interference fringes differs from the phase of the red modulation fringes, while the periods of these fringes are the same and equal $\lambda_g/2$. This effect is shown in Fig. 5.4. The phase difference between the green interference fringes and red modulation fringes determines the correlation phase.

Here we note again that in Fig. 2.4 the fringes have opposite phase, i.e. a maximum in the green fringes corresponds to the minimum in the red signal. The explanation given was that a minimum of ρ_{pp} has to coincide with a maximum of Γ_g due to the increased depopulation of the upper level [6]. Of course this explanation is oversimplified, and that measurement was just a lucky example due to the fact that the correlation phase in the vicinity of the resonance is equal to 180° for the normal laser parameters. Far from resonance the correlation phase is presumed to be equal to –180° [38].

In the case of small ε, the excited state population at fixed laser detunings and intensities can be written in the following form

$$\rho_{pp} = A_1 + \varepsilon[A_2 \cos(2kz) + A_3 \sin(2kz)], \tag{5.13}$$

where quantities A_1, A_2, A_3 depend on the laser intensities and detunings [15]. Without a level shift, the factor A_3 vanishes, and the population of the excited state ρ_{pp} and

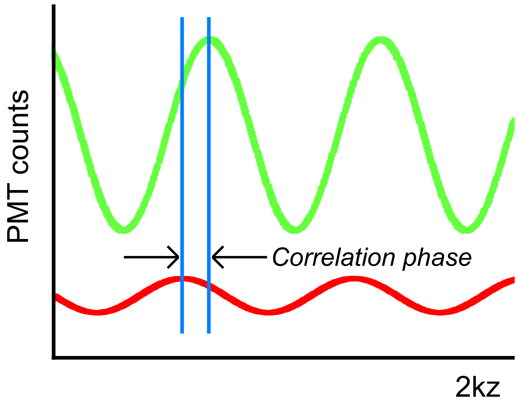

Figure 5.4: This figure illustrates the definition of the correlation phase. The green interference fringes and the modulated red signal are measured simultaneously while scanning the ion-mirror distance. The phase difference between these two signal is called the correlation phase.

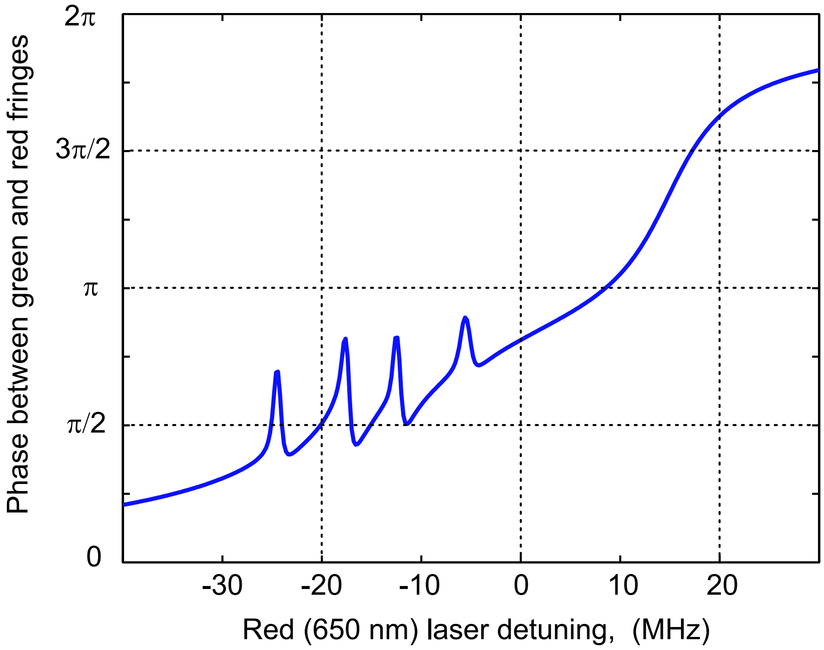

Figure 5.5: Correlation phase between green and red fringes, calculated with the same laser parameters as for Fig. 5.3.

green interference signal have opposite phase. However the existence of a level shift leads to a shift of the correlation phase from ±180°.

The correlation phase depends on the laser detunings: if, for example, the red laser is detuned well below resonance and is stepped in frequency towards the blue side of the resonance, then the correlation phase is seen to change by 360°.

The behavior of the correlation phase versus detuning of the red laser is shown in Fig. 5.5. The change in the correlation phase is not uniform with laser detuning, and is reminiscent of the behavior of the phase of a damped oscillator, with the addition of four extra spikes to it. These spikes are associated with the dark resonances. For certain laser parameters, for instance when the saturation of the red laser is high, the correlation phase in the region of positive detuning bends down. The reason why this happens is not yet clear, and requires further study.

Measuring the phase and the amplitude of the red fringes is a way of measuring the level shift and modified spontaneous decay. The next chapter will be devoted to that experimental study.

6 Spectroscopic method of level shift measurements

In the previous chapters we have shown that the level shift of the upper state of an atom has two experimental signatures. One can be viewed as a mechanical action of the retroreflected field on the atom, the other is a non-trivial excitation probability versus detunings of the lasers.

In this chapter we will describe the experimental results from an interference experiment in which the excited state population depends on laser detunings and the on-mirror distance. The dependence of the correlation phase (between red and green fringes) on laser detunings is experimental evidence of the P-level shift.

The experimental setup is the same as was described in Chapter 2, and is shown in Fig. 2.3. At first we will describe some additional measurements, such as beam waist measurement at ion position and FFT of the green and red fringes.

6.1 The quality of the focusing retroreflected beam onto the ion

The ion and its mirror image can be observed visually through the L1 port. Fine adjustment of the overlap is critical in obtaining high-contrast interference fringes, that is why there is an additional piezo actuator on the mirror holder for fine tuning by an angle of 10^{-2} rad. To scan through this angle we supply a DC-voltage to one of the fine-tuning piezo translators, while the other piezo remains at the same voltage. The tilt of a mirror is accompanied by a small amount of ion-mirror distance scan in our setup. Therefore the appearance of the interference fringes upon tilting the mirror indicates that the retro-reflected beam is focussed at the position of the ion. The interference pattern during the angle scan is shown in Fig. 6.1. The profile of the reflected beam at the position of the ion is clearly observable, and the beam waist size can be estimated from the tilt angle of the mirror and the value of the contrast.

The theoretical diffraction limit for the HALO lens used in our experimental setup is approximately 1.1 μm. The measured beam waist diameter is about 2 μm. We presume that the actual beam size is bigger due to optical imperfections, i.e. aberration of the HALO lens, optical misalignments, etc. For example, if the lens L1 and the HALO lens have some axis mismatch, coma abberation also appears. The interference profile will

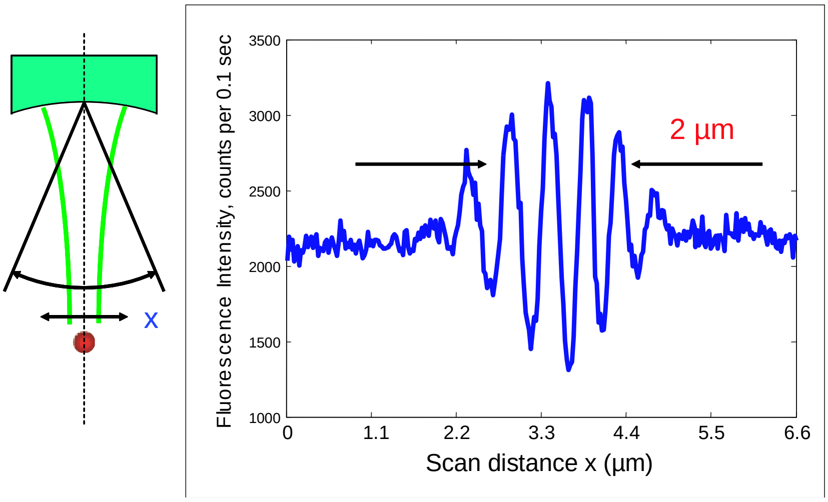

Figure 6.1: The fluorescence rate from a single ion in interference experiment as a function of a beam scanning distance in lateral direction (right). Scan distance is calculated from a tilt angle of a mirror. The additional schematic to explain experimental method (left).

then reveal more modulation features.

The quality of the beam focusing onto a single ion is associated with the coupling strength between reflected field and an atom, as shown in Chapter 4, and thus strongly affects the value of the red contrast. Here we must note that all formulas describing the modification of spontaneous decay rate and the level shift of an atom or classical dipole in front of a mirror, see Equations 4.18, 4.19, 3.17 and 3.18, have been derived under the assumption of diffraction limited ideal beams. That means that the retroreflected beam has a smallest possible diameter in the focus position. In the experimental situation the real beam waist can differ from the theoretical calculation, hence the measured value for the red modulation contrast or for decay rate modification will differ from the theoretically expected one.

Let us estimate the value of the effect from the measured diameter of the beam waist. The modification of a spontaneous decay rate $\Delta\Gamma_g \sim \rho(z)$, where $\rho(z)$ is the density of the electromagnetic modes of the retroreflected beam at the position of an ion. The latter is inversely proportional to the area of the focused beam $\sim 1/D^2$, where D is the diameter of the focused beam provided by the lens. Hence the amount of the effect will differ from the theoretical predictions by the factor $(D_{dif}/D_{real})^2$, where D_{dif} is a diffraction limit for the diameter of a beam waist, and D_{real} is a real beam diameter of a beam waist, which is provided by the HALO lens in our setup. Therefore we conclude that the contrast of the red fringes measured in our experiment is equal not to 4% as expected from the theoretical predictions, but will instead be approximately 1.2%.

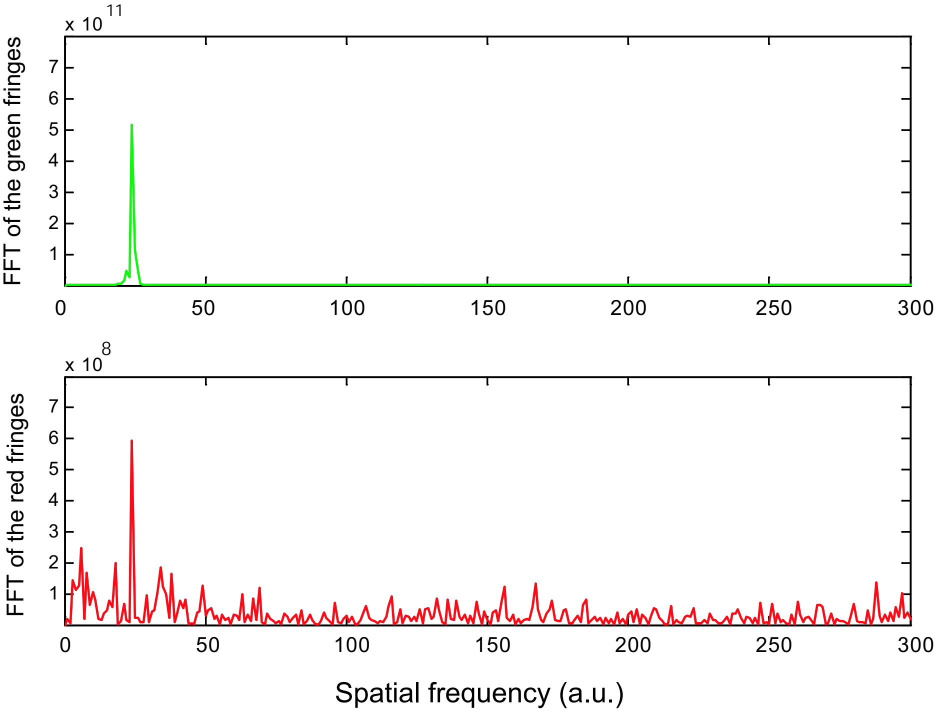

Figure 6.2: FFT transformation of the green and the red signal. The period of the red fringes is equal to the period of the green interference fringes.

6.2 FFT of the red and the green fringes

Simultaneously with the green signal on PMT1 we record on PMT2 the red fluorescence transmitted through the mirror. Varying the mirror-ion distance, which gives rise to the 493 nm fringes, it is also seen to modulate the red light with the same period [6]. To prove this we record the green and red fluorescence rate whilst scanning the mirror over 20 periods of an interference picture. After that, we take a FFT of the green and red recorded scans and the result is shown in Fig. 6.2.

As one can see from Fig. 6.2, there is a spike in each spectrum at the same spatial frequency, which is equal to $4\pi/493$ nm. Note that this modulation is not an interference at the red wavelength, as this would lead to a different modulation period equalling $4\pi/650$ nm. The red fringes are caused by the back-action of the mirror on the atom, i.e. that the mirror modifies the vacuum field at the green wavelength and leads to enhancement and inhibition of spontaneous decay from the $P_{1/2}$ state. As a consequence, the population of the $P_{1/2}$ level is modulated. Since the mirror reflects only the radiation at 493 nm, only the decay constant on the $^2S_{1/2}$ to $^2P_{1/2}$ transition is modified, its variation being proportional to the green fringes.

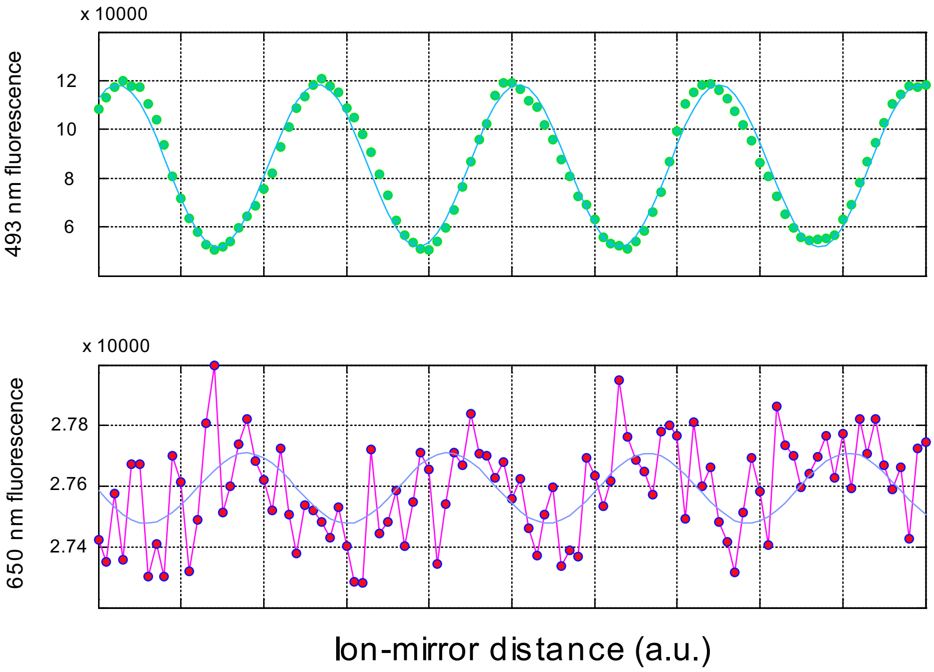

Figure 6.3: The green interference fringes (top) and the red modulation fringes (bottom). Sinusoidal fit have the same period for both pictures. Note that red and green fringes are not completely anti-correlated. There is a phase shift of about 150° between the respective fringes, which is due to the level shift of an excited state.

6.3 Measurement of the correlation phase

The detected red light is a measure of the P-state population, thus revealing the back-action of the mirror on the atom. Then one could expect that enhancement of spontaneous decay at 493 nm leads to increased de-population of the upper state and a decrease in the rate of detected 650 nm photons, while inhibited decay at 493 nm increases the 650 nm count rate. However, instead of such an anti-correlation, we observe a phase between the green and the red modulation which varies with the laser detuning and takes all values between correlation (phase close to 0 or 2π) and anti-correlation (phase π).

The typical scan of green interference fringes and red fringes is shown in Fig. 6.3. The red laser is tuned to the resonance of the line, the green laser is tuned to conditions for optimal cooling (approximately -20 MHz), the red intensity is adjusted to a level where we observe maximum green fringe contrast for the given intensity of a green laser. In this situation we found that the saturation parameter for the intensity of the red laser S_r (see Chapter 5) is about three times larger than for the intensity of the green laser. This is the optimal intensity ratio for optical pumping of the excited state

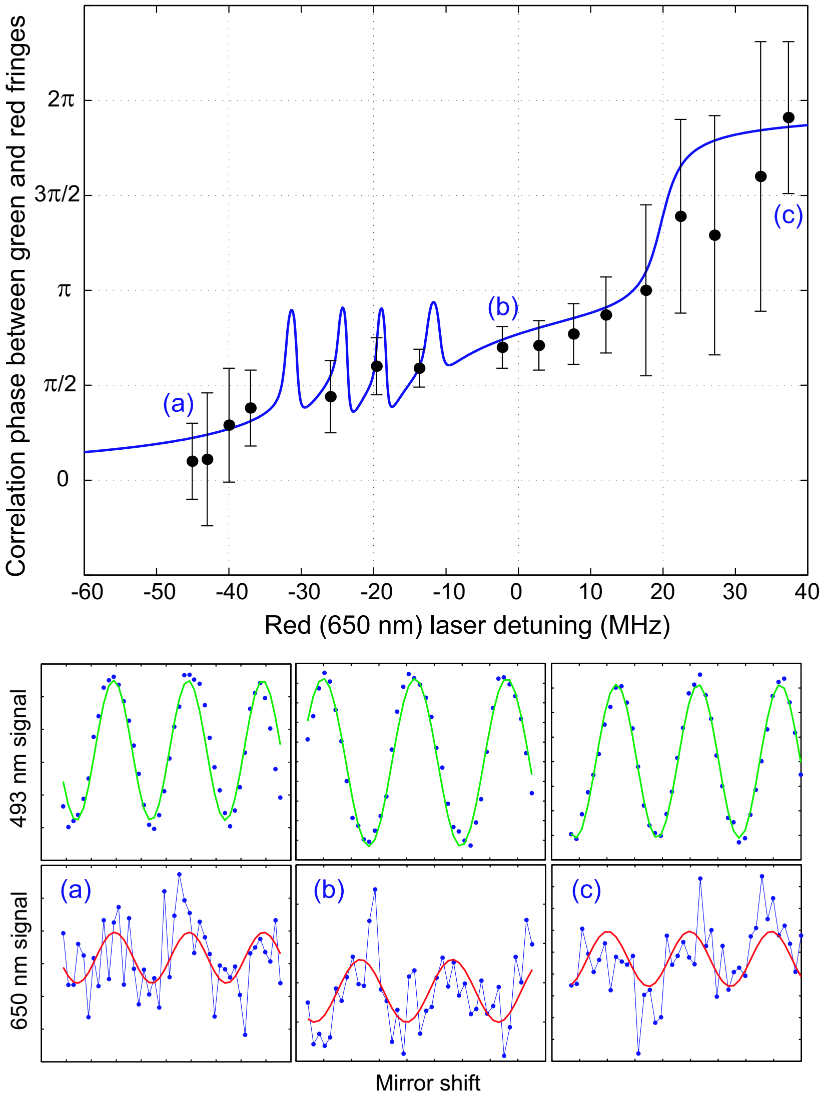

Figure 6.4: Large graph: Correlation phase between the observed fringes in the green and in the red fluorescence versus detuning of the red laser. The line is a calculation using 8-level Bloch equations, see Chapter 5. The narrow peak structures are caused by dark resonances [38]. For the three data points marked a), b), c), the smaller graphs display the simultaneously recorded green (top) and red (bottom) fringes, showing how the correlation phase varies between 0 and 2π.

and equals the ratio of decay rates of green and red channels.

A plot of this correlation phase as a function of the detuning of the red laser is shown in Fig. 6.4. For large negative or positive detunings, the green and red fringes are in phase, while with the red laser close to resonance, anti-correlation is observed.

As we will show now, this dependence of the correlation phase is a direct consequence and an experimental verification of the energy shift of the $P_{1/2}$ state (which is always associated with a modified decay rate of this state).

The data in Fig. 6.4 represent 7 hours of near-constant interrogation of a single barium ion. For each 650 nm laser detuning, up to 20 green and red interference periods were recorded simultaneously while the ion-mirror distance was varied. The correlation phase was then determined from a sinusoidal fit to red and green fringes with the same period equalling the period of the green interference. The 493 nm laser is stable to about 1 MHz over long periods whilst a red laser reference cavity drift rate of $\sim$ 2 MHz/hr limited the accuracy to which the 650 nm laser detuning could be determined. The data in Fig. 6.4 have detunings accurate to within ±1 MHz. The detuning of the red laser had been checked every half hour by taking an excitation spectra and by fitting it to 8-level Optical Bloch Equations. The green and red laser parameters defined from this spectrum are: $S_r = 1.63 \pm 0.07$, $S_g = 0.75 \pm 0.02$, $\Delta_g = -20.4 \pm 0.1$ MHz.

The red fringe contrast also varies with red laser detuning. It reaches values up to 2.5%, but for the laser parameters that were used in the data of Fig. 6.4, it reaches a minimum for a detuning of $\Delta_r \approx +20$ MHz. This, in conjunction with poor Doppler cooling at positive detunings, accounts for the large measurement errors in the correlation phase in this regime. The measured variation of the red fringe contrast is shown

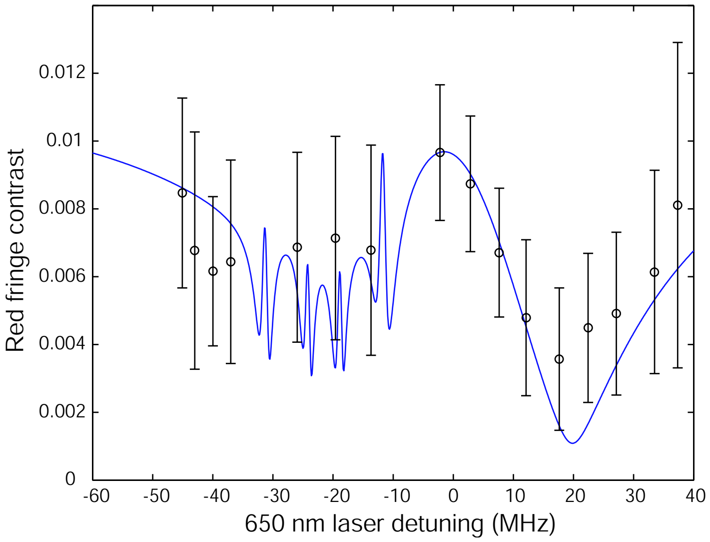

Figure 6.5: Red fringe contrast vs. detuning of the 650 nm laser for the data set of Fig. 6.4. The curve is calculated from Bloch equations with an effective solid angle of $\varepsilon = 1.6\%$ of 4π. The error bars are due to shot-to-shot variations. The maximum observed contrast of a single shot corresponds to $\varepsilon = 3\%$.

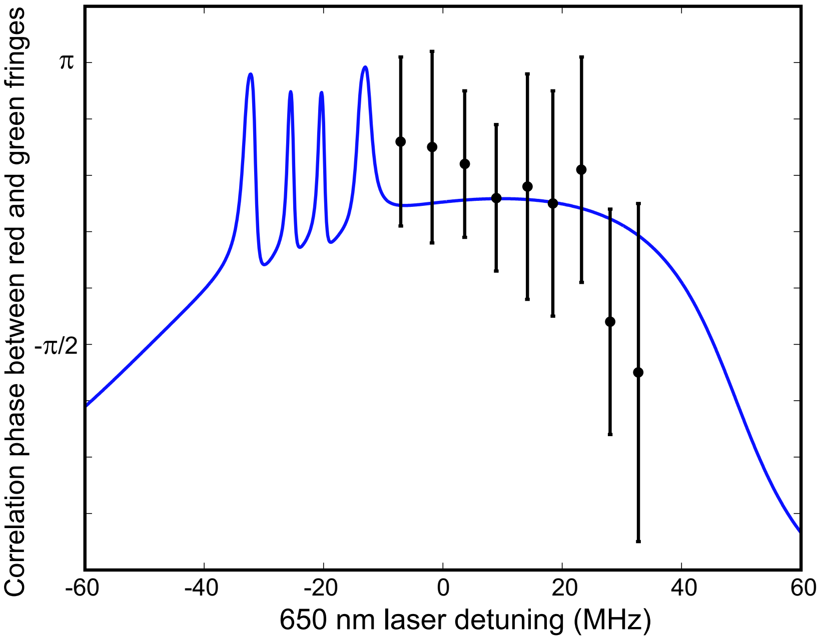

Figure 6.6: Measurement of the correlation phase vs. red detuning in the case where for large positive detunings the correlation phase decreases to zero rather than reaching 2π. Due to sub-optimal laser cooling, resulting from high red laser power, the fringe contrast decreases which leads to large error bars.

in Fig. 6.5. From a comparison with the expected dependence, again calculated with the Bloch equations, we estimate that optimally the mirror subtended an effective solid angle of $\varepsilon = 3.2\%$ of 4π, but the typical value is about 2%.

6.4 Multilevel effects in correlation phase measurements

While all observations are well described by the model, thus verifying that the level energies and decay rates are indeed modified by the distant mirror, we also find peculiar features which are due to the multi-level structure of the atom and would not appear in a simple two-level system. The red fringe contrast can fall completely to zero for a specific positive detuning of the 650 nm laser and a particular ratio of the laser intensities. In other words, modification of the decay constant on the green transition may have no effect on the excited-state population. If from that particular set of parameters, the red laser intensity is increased further, the dispersive dependence of correlation phase vs. detuning shown in Fig. 6.4 changes shape. At large positive Δ_r it is seen to return to zero instead of going up to 2π. An example is displayed in Fig. 6.6.

The laser parameters defined from the OBE for Fig. 6.6 are $\mathrm{S}_r = 2.4 \pm 0.07$, $\mathrm{S}_g = 0.8 \pm 0.02$, $\Delta_g = -20.4 \pm 0.1$ MHz. While it can be suspected that an interplay of modified decay and optical pumping is responsible for this behavior, the detailed underlying causes could be the subject of future study.

7 Detection of macro-motional sidebands

In this chapter we will describe how the macro-motion of a single Ba^+ ion in a Paul trap can be detected. The macro-motion is also known as the secular motion and is associated with the thermal energy of an ion. The ion moves with an amplitude of approximately 30 nm at a frequency of 1 MHz, see Eq. 2.5. As can be seen the ion displacement is 16 times less than the ion's emission wavelength ($\lambda_g = 493$ nm). Apparently, it is not possible to observe its motion through a conventional microscope, due to Abbe's criterion, which claims that two objects can be resolved if they are separated by a distance more than $\lambda/(2\sin\Theta)$, see [74], where Θ is the angle subtended by the objective in the point of observation.

There are several techniques that allow the diffraction limit of optical observation to be beaten. We will postpone at least part of this discussion until the chapter 9. Here we will outline two experiments which have been performed so far in our laboratory with a single Ba^+ ion. In the first experiment a heterodyne technique, where a part of the ion fluorescence was mixed with a strong laser field at a different frequency, was used to observe a motional sideband, see [75]. A low signal-to-noise ratio was the main problem of that experiment, therefore it was possible to measure only externally excited sidebands.

A second experiment used the interference technique as described in section 2.3. In article [6] such a configuration was proposed to act as a microscope to measure the average position of an ion. This idea was later developed to make a sub-wavelength probe for the optical fields [44].

Here we will show that our experimental setup allows us to directly observe macro-motional sidebands explicitly with rather high signal-to-noise ratio (about 8 dB) without any additional external excitation of this motion. Even in the regime of counting photons the spectrum of the photocurrent contains all relevant information about the spectrum of the incident light, and hence also of the ion's motion. The limiting factor in this measurement is photon or Poissonian noise appearing during the photon detection process [58, 76].

7.1 Detection of ion motion

The motion of an ion can be detected using an interference technique as shown in Fig 7.1. Let us calculate the photocurrent signal from the PMT using a classical picture. The PMT signal will then be a continuous signal in time and reads

$$i(t) = I_o(1 + V \sin 2k(z_o + z(t)), \tag{7.1}$$

where I_o is the average fluorescence level from the ion, V is the visibility of the interference fringes, z_o is the distance between the mirror and the center of the trap and $z(t)$ is the ion displacement from trap center.

The phase of the interference fringes, or in other words, the exact intensity on a fringe depends sinusoidally on the ion-mirror distance. When the ion is placed in the middle of a fringe slope, the intensity level will be proportional to the ion displacement from the mid-position, provided such a displacement is much less then a spatial period of the interference. In this case the motion of the ion appears in the photocurrent intensity as an amplitude modulation, see Fig. 7.1. Then the photocurrent is given by

$$i(t) \approx I_o + 2VI_okz(t), \tag{7.2}$$

and the correlation function of the photocurrent will be

$$\langle i(t)i(t+T)\rangle = I_o^2 + 4(I_oVk)^2\langle z(t)z(t+T)\rangle. \tag{7.3}$$

The first term in Eq. 7.3 is just a DC-signal of constant intensity level, the second term depends on the instant position of the ion at time moment t, hence this term represents the ion motion.

Using a quantum-mechanical description for that model yields a different picture. The field will be described by the quantized vector potential, see Eq. 4.1. The total electric field can then be written as $E(t) = \mathsf{E}(t) + \mathsf{E}^+(t)$. The intensity operator is then defined by as $I(t) = \mathsf{E}^+(t)\mathsf{E}(t)$. The photocurrent consists of a pulse train, where each pulse is caused by a photon detection event. Assuming that the response bandwidth of the photodetector is large, each photodetector click can be approximated by a δ-function. Then the signal reads

$$i(t) = \sum_i \delta(t - t_i), \tag{7.4}$$

where counts appear at random moments of t_i. Calculating the correlation function of the photocurrent we obtain

$$\langle i(t)i(t+T)\rangle = \overline{\sum_i \sum_j \delta(t - t_i)\delta(t - t_j + T)}, \tag{7.5}$$

where the averaging is taken over the distribution of the photo-counts. This expression is calculated in [76], for example. Here we will write only the result

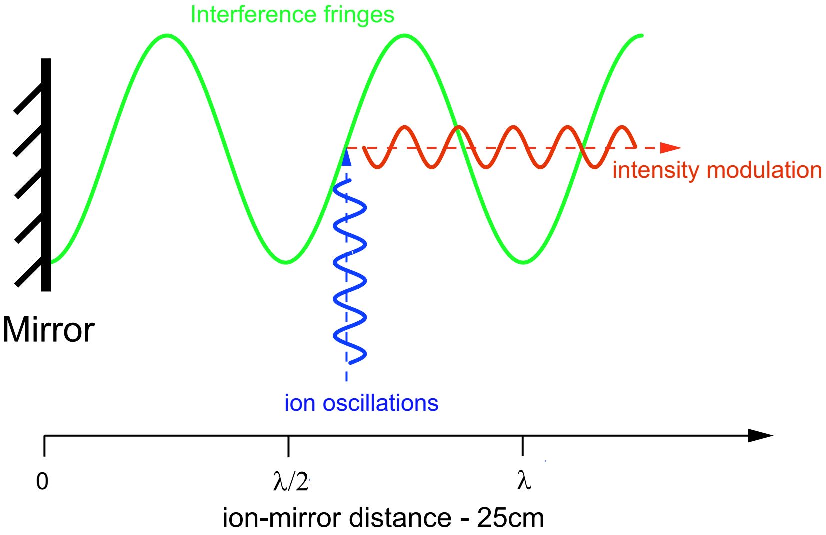

Figure 7.1: The ion moves around the middle of the slope of an interference fringe. The intensity of the interference fringe is proportional to the instantaneous ion position. Therefore on the fringe slope the ion's oscillations modulate the fluorescence level.

$$\langle i(t)i(t+T)\rangle = \eta I_o \delta(T) + \eta^2 G_2(T), \tag{7.6}$$

where $G_2(T) = \langle \mathsf{E}^+(t)\mathsf{E}^+(t+T)\mathsf{E}(t)\mathsf{E}(t+T)\rangle = \langle : I(t)I(t+T) :\rangle$ is a normally ordered second-order correlation function for the light fields [77], $I_o = \langle I(t)\rangle$ is an average intensity, η is a quantum efficiency of the photodetector.

The first term in Eq. 7.6 is the Poissonian noise, the second term is a quantum correlation function which has a direct correspondence to the classical correlation function. Now it is possible to calculate directly the spectrum of the photocurrent for our setup. The correlation function of the photocurrent will be

$$\langle i(t)i(t+T)\rangle = i_o \delta(T) + i_o^2 + 4(i_o V k)^2 \langle z(t)z(t+T)\rangle, \tag{7.7}$$

where $i_o = \eta I_o$ is the mean value of the photocurrent. Thus the quantum correlation function for the photocurrent and the classical correlation function differ by the Poissonian noise term only. According to the Wiener-Khinchine theorem the spectrum of the signal is the Fourier transformation of its correlation function. Let us also introduce the power-spectrum of the ion motion, which is given by:

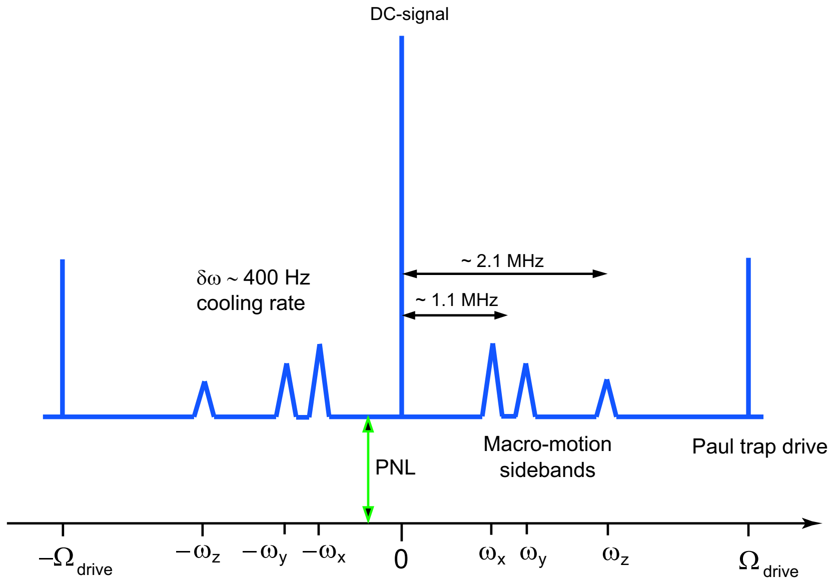

Figure 7.2: The spectrum of the interference signal when the ion sits in the middle of a fringe. The power spectrum has a baseline which is equal to Poissonian noise (PNL). The central spike is equal to the intensity squared (DC-signal). The macro-motion and micro-motion sidebands are shown schematically. The higher-order sidebands are omitted. The macro-motion sideband broadening is due to laser cooling [38].

$$S_M(f) = 2\pi \int \langle z(t)z(t+T)\rangle e^{-i2\pi fT} dT. \tag{7.8}$$

Note here, that in the experiment we use units of Hz instead of radians per second, that is why we are calculating the spectra in terms of the normal frequency f.

By taking the Fourier transformation of Eq. 7.7, and substituting into it Eq. 7.8, we obtain for the expected spectrum of the photocurrent

$$\langle i^2(f)\rangle = 2\pi i_o + 2\pi i_o^2 \delta(0) + 4(i_o V k)^2 S_M(f). \tag{7.9}$$

The power spectrum of the interference photocurrent contains three components, see Fig. 7.2. The first is the shot-noise or Poissonian noise which forms a baseline. The second term is the DC-signal and it is associated with the intensity level. The third term represents the ion motion and scales proportional to the square of production of the mean intensity and the contrast of the interference fringe.

The ion oscillates in the trap with four different frequencies [38], three frequencies $\omega_x, \omega_y, \omega_z$ corresponds to the macro-motion and Ω_{drive} corresponds to the oscillation with the frequency of the trap drive. If the motion with a certain frequency has a projection on the optical axis it will be revealed in the spectrum of the resonance fluorescence in the interference experiment.

7.2 Experimental setup

The total experimental setup for measuring the ion's motion is shown in Fig. 7.3. The optical arrangement is very similar to the interference experiment described in chapter 2, see for example Fig. 2.3. In the old experiment we used a mirror with a diameter of 20 mm, which is slightly less than the output aperture of a HALO lens (21mm). In the present experiment we use a mirror with a diameter of 50 mm, as we assumed the smaller diameter of the previous mirror could be an additional source of wavefront distortions in the focus of the HALO lens because of diffraction on the

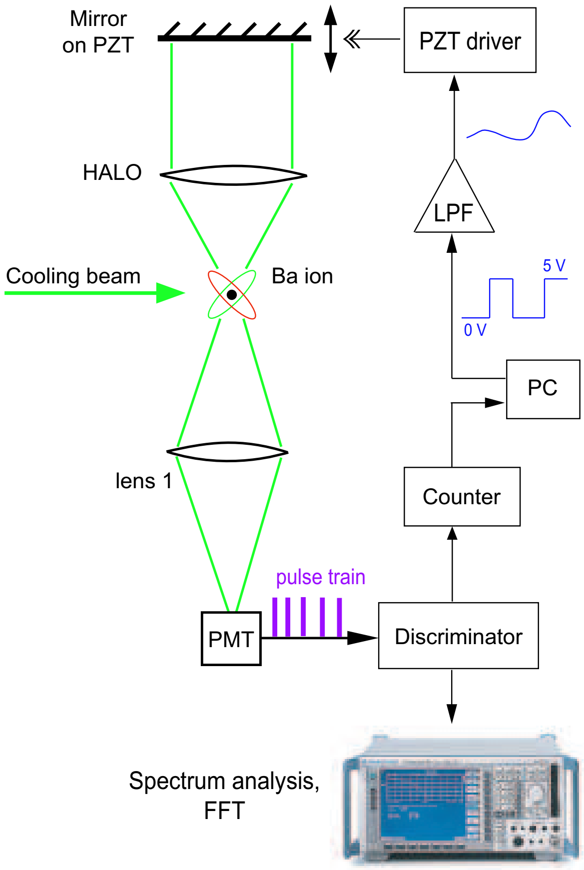

Figure 7.3: Interference experiment to detect ion motion with a fringe-lock setup. The optical setup is practically the same as used in earlier experiments, see for example Fig. 2.3.

mirror edges.

The mirror is 99.9% reflecting for the green light, and 4.3% reflecting for the red light. The green part of the resonance fluorescence is reflected back to the ion, and interferes with the light which is directly scattered from the ion. The red part of the resonance fluorescence passes through the mirror. High contrast interference fringes appear when the ion-mirror distance is scanned. The green light is focused with lens 1 and detected with a new photomultiplier tube Hamamatsu H7421. This tube has a GaAs photocathode and built-in Peltier cooling element. The PMT has a 47.8% quantum efficiency for 493 nm and an average dark count rate of 25 counts per second. This allows us to measure the intensity of a single ion's fluorescence with high signal-to-noise ration: the signal-to-background intensity ratio is approximately 30.

The photocurrent is a TTL signal with pulse width of 30 ns. The signal first goes to the TTL to NIM converter (as demanded by our data collection system), then to the pulse discriminator. After the pulse discriminator the signal has a –1 V amplitude and a 30 ns pulse width. The pulse width and amplitude can be varied by changing the setting parameters of the discriminator.

In our experiment, the pulse discriminator is used as a standard demultiplexer, as it has one input and five synchronized outputs. The first output goes to a photon-counter, the second one goes to a TDC (time to digital converter) and that signal is used for the micro-motion detection and compensation and the third is spectrally analyzed with an FSP-13 (Rohde and Schwarz) spectrum analyzer.

To stabilize the ion-mirror distance or phase of an interference fringe we use a fringe-lock technique, in fact we lock the ion-mirror distance to a certain intensity level of interference fringe. The intensity level in our case is the number of counts per certain time interval (usually 100 or 200 ms) as determined by a pulse counter which is controlled by our LabView interface programm.

The intensity lock-level is set in the program. When the intensity of the fringe differs from the lock level, the program, depending on the lock polarity, writes 0 or 1 to the DAQ-card buffer, and the output of the card will then be assigned to an amplitude of 0 or 5 V. To make the mean level of the signal equal 0 V, we shift the output signal down by –2.5 V. Low-pass filtration with a time constant of approximately 5 seconds is used to smooth voltage jumps. After filtration the signal is feed to the HV-piezo driver.

After amplification by the high voltage piezo driver, the error signal has an average amplitude of approximately 50 mV. This voltage corresponds to a 500 nm piezo displacement and gives the tracking range for the control of the ion-mirror distance. The experimental setup itself is found to be stable enough only to keep the interference phase constant within several tens of seconds. With the fringe lock the ion-mirror distance is stabilized to within 5-10 nm accuracy and can be kept for up to 10-20 minutes, which is sufficient time to perform our measurements.

The demonstration of the fringe lock functioning is shown in Fig. 7.4. As can be seen in that figure, for the first 10 seconds the lock is switched off and the ion-mirror distance

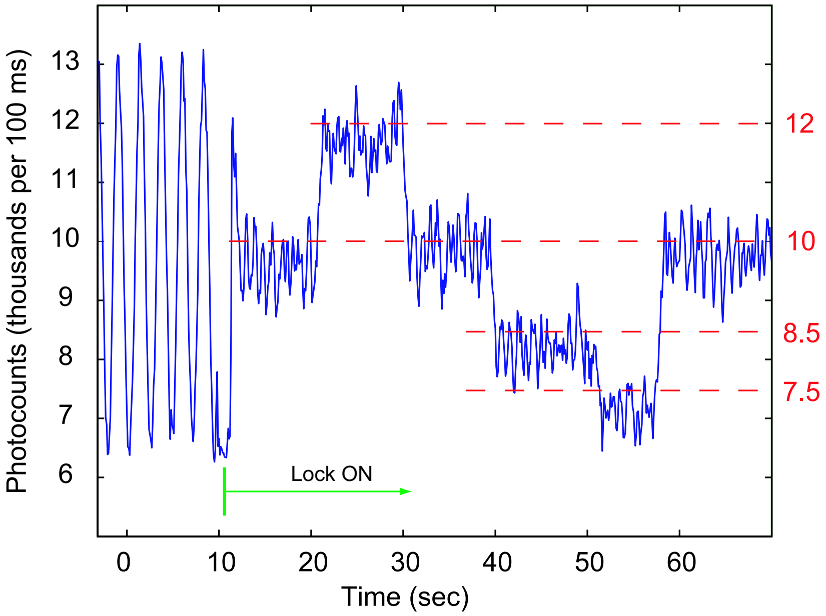

Figure 7.4: This figure shows the performance of the fringe-lock. Lock positions are depicted as dashed lines.

is scanned, leading to the appearance of interference fringes. Then the fringe-lock is switched on and the phase of the interference is set to a certain level of intensity equal to 10000 counts per 100 ms. Practically, we can lock to any phase of the interference fringes, or to any intensity level on the fringe. It can be seen also that the interference phase can be locked almost to the maximum of the fringe (12000 counts per 100 ms) down to the minimum of the fringe (7500 counts per 100 ms). The time constant for the fringe lock is approximately one second. The actual intensity level when the lock is on is about 5% less than the set point due to the imperfectly compensated integrator in the low-pass filter.

7.3 Detection of the macro-motional sidebands

To detect macro-motional sidebands in our experimental setup, at first we have to prepare an optimal interference picture from a single ion and its image, and this can be achieved by slightly tilting the mirror and setting green and red laser intensity levels to the predetermined values, see section 6.3. The mean intensity of an ion together with its image is usually between 4000 and 8000 counts per 100 ms, and the contrast of the fringes is typically about 40%. For these settings the laser intensities are quite close to saturation. The trap operates at a power of 5 W. The ion-mirror distance is locked to the middle of an interference slope.

The second step is to detect the motional frequencies of the ion and to see these on a spectrum analyzer. The initial position in frequency of the sidebands can be found by supplying an external excitation to the end-caps at the frequency of 0.8 – 2.5 MHz (the frequency range depends on the trap power). Excitation amplitude should be around –30 dBm. As soon as the excitation frequency starts to approach a sideband frequency, the interference contrast goes down due to strong ion oscillations.

Once the sideband frequencies are roughly known, they can be seen directly on the spectrum analyzer. For example, at 5 W trap drive power the frequencies of X and Y modes lie at around 1 MHz and 1.2 MHz respectively. The mean frequency between sidebands we assign as a central frequency on the spectrum analyzer, the frequency span is set to 200 kHz, the resolution bandwidth (RBW) is equal to 100 Hz and the RBW filter is set to FFT mode, in that situation the spectrum analyzer performs an FFT analysis of the signal. The acquisition time of a single spectrum in the FFT mode with these settings is 30 ms. The intrinsic noise of the spectrum analyzer is less than –120 dBm. To remove video noise from the spectrum, the number of trace averages (NAvg) can be set around 30 to 60. The spectrum of the resonance fluorescence is shown in Fig. 7.5. The sidebands appear on the spectrum as sharp resonances above the Poissonian noise baseline. The frequencies are equal to 1020 kHz and 1180 kHz

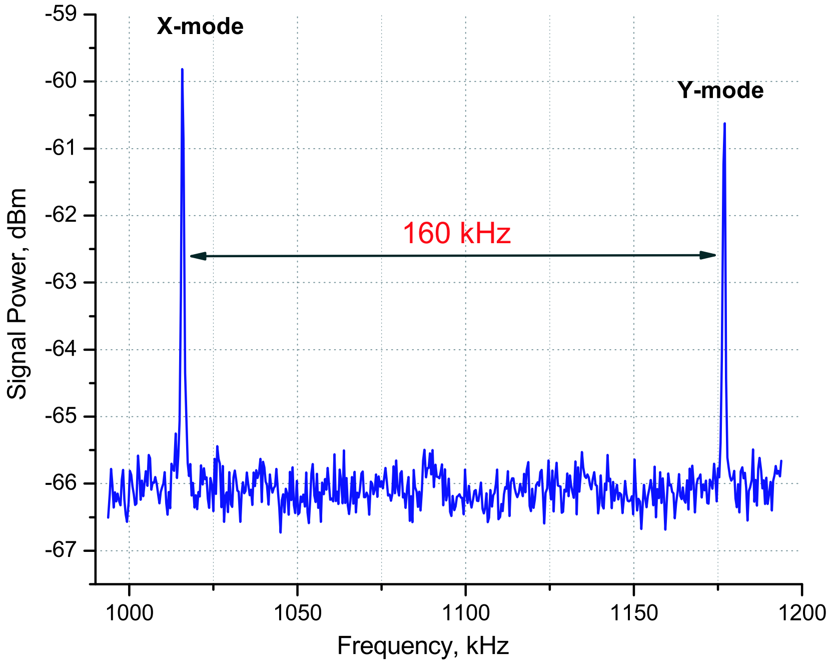

Figure 7.5: RF-Spectrum of the resonance fluorescence when the ion sits in the middle of the interference slope. X and Y sidebands are seen as sharp resonances with amplitude of 6 and 5.5 dB respectively above the Poissonian noise baseline.

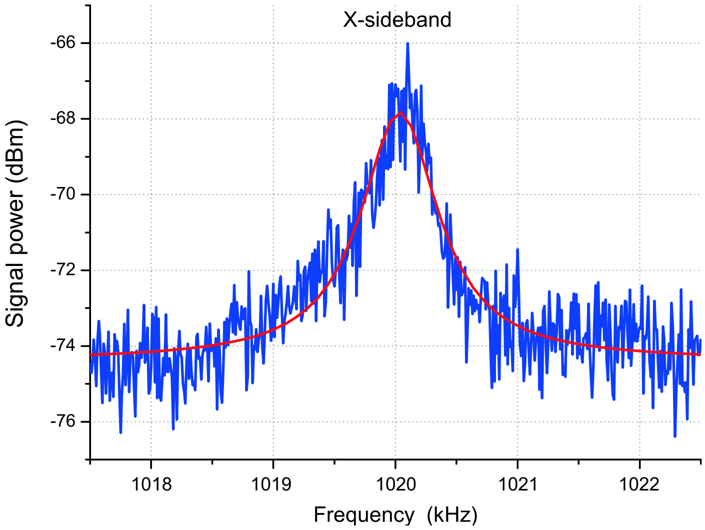

Figure 7.6: X-sideband of the macro-motion (blue curve) and Lorentzian fit (red curve). Frequency width $\Gamma = 470 \pm 20$ Hz. The spectrum analyzer frequency span is 5 kHz, RBW = 10 Hz, NAvg = 30.

and the amplitude is about 6 dB above the noise floor.

To look at the macro-motional sidebands in detail, the frequency span and RBW have to be reduced. For example, in Figs. 7.6 and 7.7, spectra of the X and Y sidebands are shown respectively. The spectrum of a sideband looks like a resonance line with an amplitude of 6 dB above the Poissonian noise and a frequency width of approximately 500 Hz and can be well approximated with a Lorentzian line. The central frequency of this line is equal to the ion's thermal oscillation frequency and after several seconds of averaging can be determined to within 10 Hz accuracy. The amplitude of the sidebands gives us information about the amplitude of the ion's oscillations in the trap, whereas the linewidth is equal to the cooling rate [79], which is in agreement with the expected values [75].

Here we should mention that the sideband shape has a small asymmetry towards the low frequency side due to the laser cooling of a trapped ion [78].

7.4 Detection of the macro-motional sidebands with different cooling beam directions

Our optical setup and the vacuum chamber allow us to illuminate the captured ion with 493 nm laser light from different directions, as shown in Fig. 7.8. The 650 nm laser beam is always directed along the X-axis with vertical polarization. Beams F and B are off-axis with respect to the main beam and are often used during the micro-motion

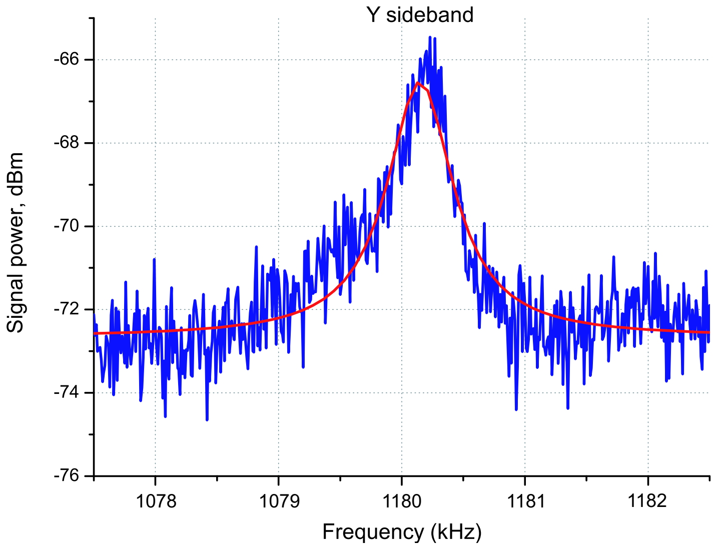

Figure 7.7: Y-sideband of the macro-motion (blue curve) and Lorentzian fit (red curve). Frequency width $\Gamma = 420 \pm 20$ Hz. The spectrum analyzer frequency span is 5 kHz, RBW = 10 Hz, NAvg = 30.

compensation process.

The X and Y oscillation modes lie in the plane of the ring electrode and are at the angle of approximately 45° with respect to the horizontal plane. The Z mode is oriented along the direction of the end cap electrodes.

The frequency of all modes can be detected by supplying the external excitation signal (with an amplitude of about –30 dBm) to the end caps and by looking at the interference fringes, as has been previously described. Due to the geometry of the setup, the cooling process turns out to be different for each mode and given beam direction. Therefore the sidebands which we observe on the spectrum analyzer have a different amplitude and width for different beam directions. Nevertheless it is important to mention that we did not find any substantial dependence of the amplitude and the width of the sidebands on the polarization of the chosen cooling beam, whether the beam goes along the F or B directions.

For example, if the front beam is used, denoted as beam F, the visibility of the fringes in that case is about 20-30%. With the green laser is detuned by about –20 MHz from the resonance, and red laser also detuned from the resonance by –10 MHz, the sideband spectra are shown in Figures 7.9 and 7.10. The amplitude of the X-sideband can be as high as 12 dB above the Poissonian noise baseline, and it is always the largest of the X-, Y- or Z-modes.

Here we have to point out that the X and Y-modes are seen if the ion is illuminated from any direction. The spectra of X- and Y-sidebands are shown in Figures 7.11 and 7.12 and taken when the B-beam is used instead. However, the Z-mode is observable only if the B-beam is used, see Fig. 7.13 and has the smallest amplitude over all beam directions and sidebands. The reason for that, perhaps, is that the direction of the Z-mode as well as directions of the cooling beams corresponds to the most optimal cooling conditions. Therefore the Z-mode has the smallest amplitude of all macromotional sidebands, and it can not be measured as effectively as the motion in other directions, however this topic needs further investigation.

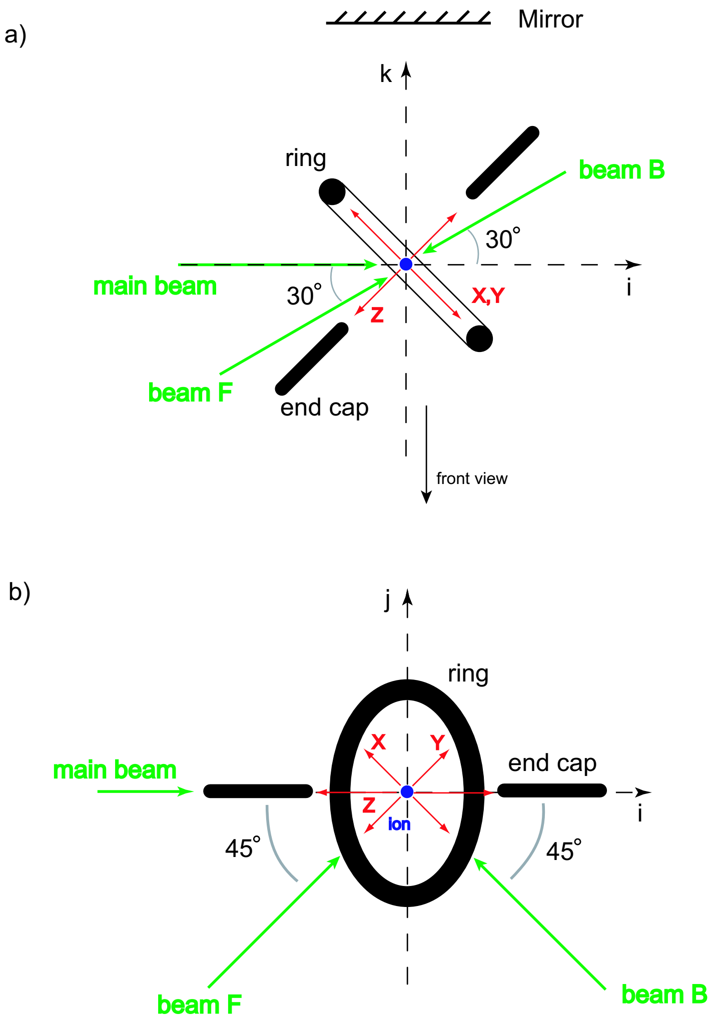

Figure 7.8: The spatial orientation of trap electrodes and green beams with respect to coordinate system (i,j,k), see also Fig. 2.2. a) is a view of the setup from above, b) is a front view, the i-axis corresponds to the main beam direction, the j-axis is directed vertically, the k-axis points away from the PMT. The direction of the red laser is always along the i-axis.

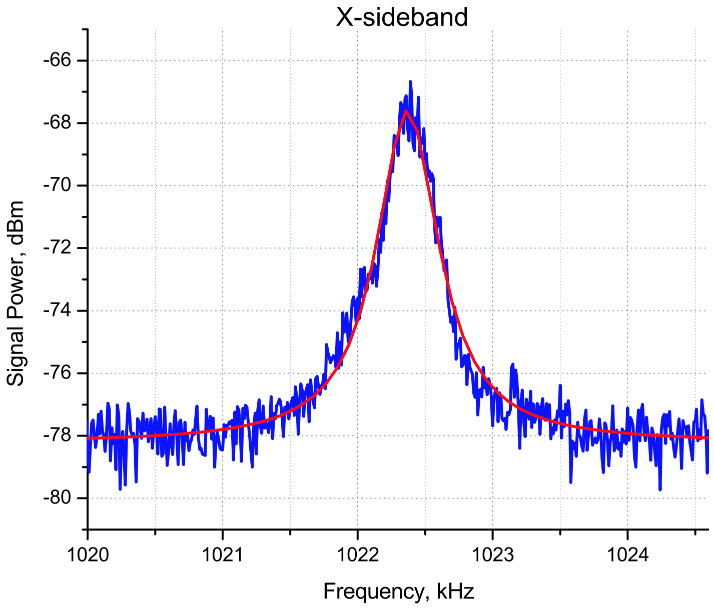

Figure 7.9: X-sideband of the macro-motion (blue curve) and Lorentzian fit (red curve). Frequency width $\Gamma = 313 \pm 5$ Hz. The spectrum analyzer frequency span is 5 kHz, RBW = 10 Hz, NAvg = 80. The F-beam is used to cool the ion.

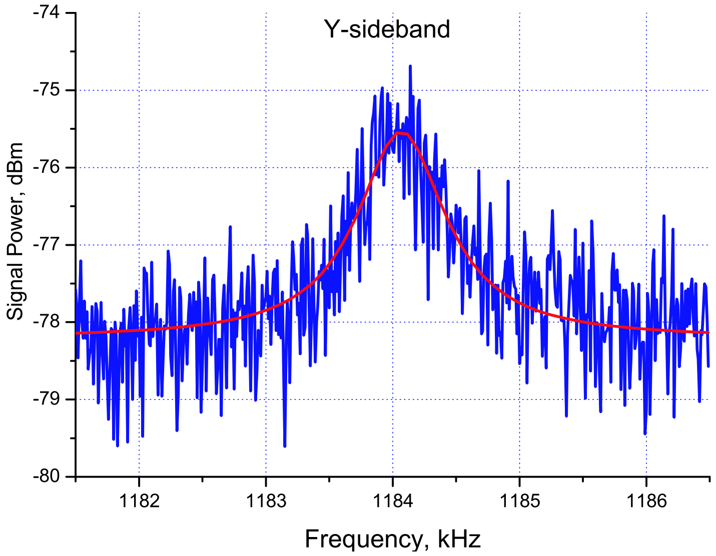

Figure 7.10: Y-sideband of the macro-motion (blue curve) and Lorentzian fit (red curve). Frequency width $\Gamma = 730 \pm 40$ Hz. The spectrum analyzer frequency span is 5 kHz, RBW = 10 Hz, NAvg = 80. The F-beam is used to cool the ion.

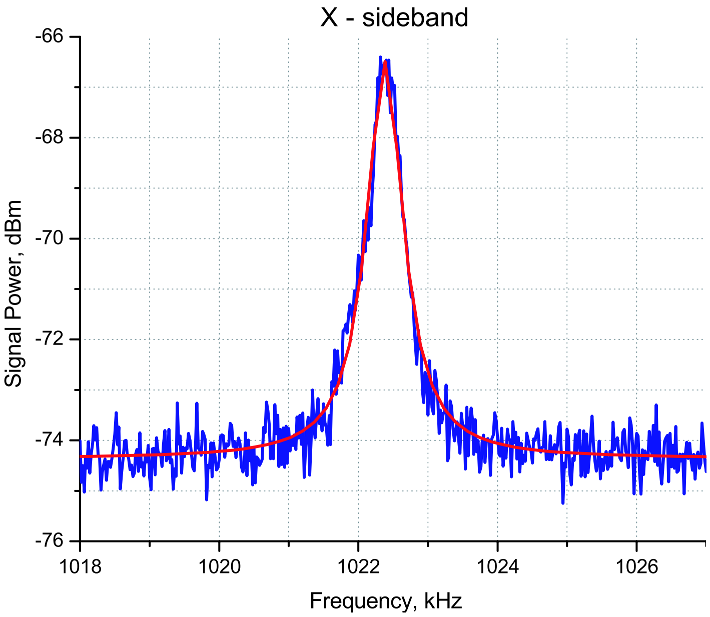

Figure 7.11: X-sideband of the macro-motion (blue curve) and Lorentzian fit (red curve). Frequency width $\Gamma = 630 \pm 10$ Hz. The spectrum analyzer frequency span is 15 kHz, RBW = 30 Hz, NAvg = 70. The B-beam is used to cool the ion.

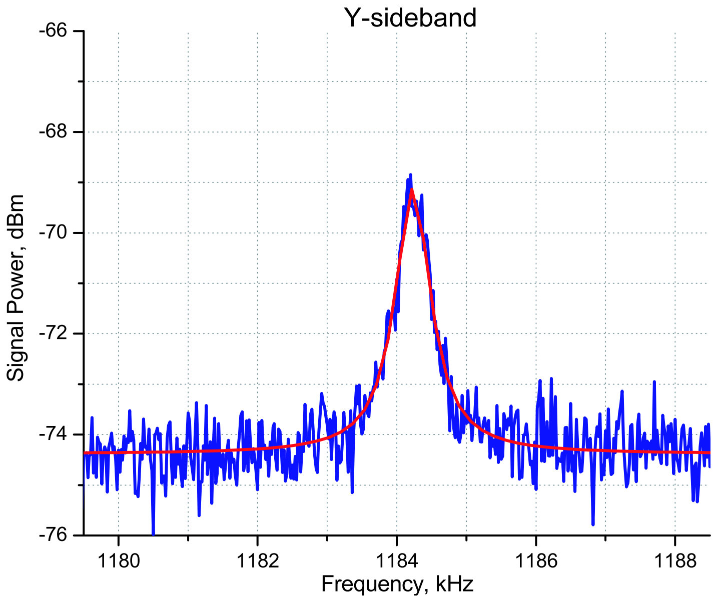

Figure 7.12: Y-sideband of the macro-motion (blue curve) and Lorentzian fit (red curve). Frequency width $\Gamma = 620 \pm 20$ Hz. The spectrum analyzer frequency span is 15 kHz, RBW = 30 Hz, NAvg = 70. The B-beam is used to cool the ion.

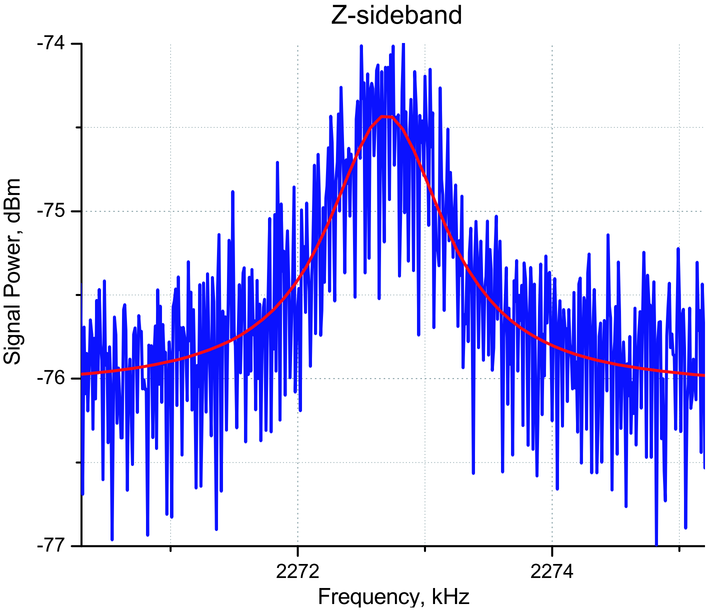

Figure 7.13: z-sideband of the macro-motion (blue curve) and Lorentzian fit (red curve). Frequency width $\Gamma = 1130 \pm 150$ Hz. The spectrum analyzer frequency span is 5 kHz, RBW = 10 Hz, NAvg = 80. The B-beam is used to cool the ion.

8 Mechanical action of the mirror-modified field on the single atom

The far-field mirror-induced shift of an excited atomic level oscillates on the wavelength scale when the atom-mirror distance is varied. Therefore, when the position of the atom is controlled to the extent that it becomes sensitive to this spatial dependence, the level shift then acts as a spatially varying potential $U(\vec{r})$, and the atom feels its gradient $-\vec{\nabla}U(\vec{r})$ as a force. The use of such a force to trap atoms in an optical resonator was proposed earlier [26, 27]; it is this kind of trapping forces which we observed for the first time in our experiment. A single trapped and laser-excited ion is an ideal system for this observation, as its position can be controlled on the nanometer scale [6,28,29], and its interaction with a distant mirror has already been demonstrated [6, 16, 17]. In contrast to these earlier experiments which detected the effect of a mirror on the electronic state of an ion, our new study reveals the action on its motional degree of freedom.

The results presented in this chapter have recently been published in [80].

8.1 The experimental method

Before we start to describe the experimental part itself, we focus on the method which was used to measure the mechanical action of the reflected field. The mirror stands at zero position on the z axis, as shown in Fig. 8.1, the position of the trap center is z_o, and the instant ion position is z_i. The ion moves in the two potentials: one is created by the Paul trap and another one is a level shift potential $U(z) = -\hbar\frac{\varepsilon\Gamma}{2}sin(2kz)$. The total potential energy for an ion can thus be written:

$$E_{trap} = \frac{M}{2}\omega_{trap}^2(z_i - z_o)^2 - \frac{\hbar\varepsilon\Gamma}{2}\sin(2kz_i), \tag{8.1}$$

where $\delta z = z_i - z_o$ is the amplitude of an ion's oscillations around its equilibrium position. The total energy can then be rewritten as:

$$E = \frac{M}{2}\omega_{trap}^2\delta z^2 - \frac{\hbar\varepsilon\Gamma}{2}\sin(2k(\delta z + z_o)) \tag{8.2}$$

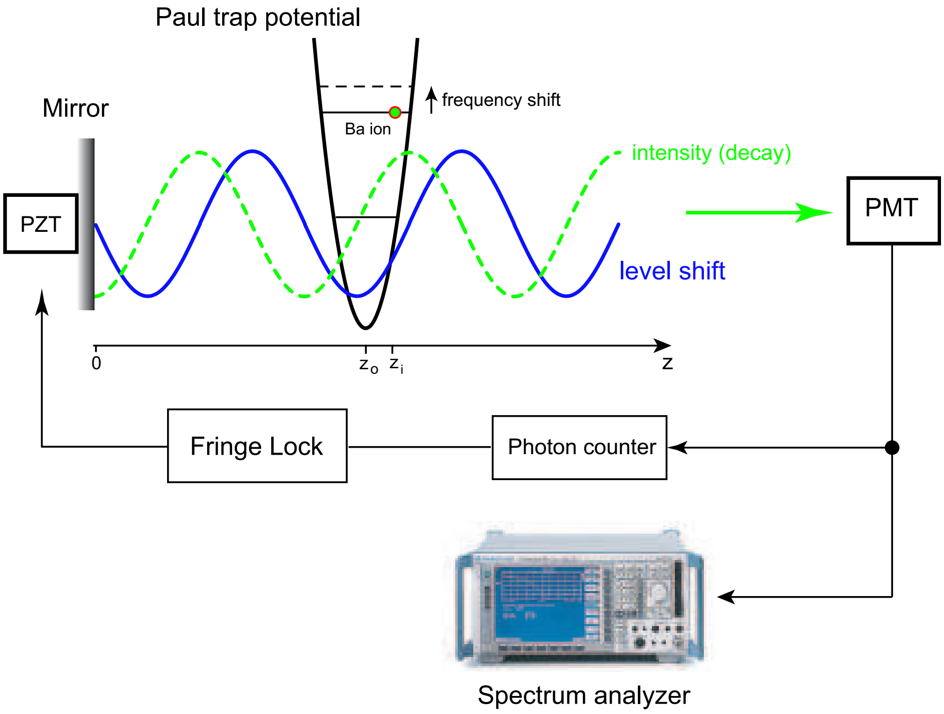

Figure 8.1: The experimental setup to detect the macro-motional frequency change due to the presence of a mirror.

The mean amplitude of the ion's oscillation is about 30 nm, therefore we assume that $\delta z \ll 1/k$, and $\delta z \ll z_o$, z_o is about 25 cm. The second term for the energy can be expanded in a δz series and we obtain:

$$E = \frac{M}{2}\omega_{trap}^2 \delta z^2 - \frac{\hbar\varepsilon\Gamma}{2}(2k\delta z\cos(2kz_o) + \cos(2k\delta z)\sin(2kz_o)). \tag{8.3}$$

The final expression for the potential energy of an ion in the presence of a mirror then has four terms:

$$E = -\frac{\hbar\varepsilon\Gamma}{2}\sin(2kz_o) - \frac{\hbar\varepsilon\Gamma}{2}\cos(2kz_o)2k\delta z + \frac{M}{2}\omega_{trap}^2\delta z^2 + \hbar\varepsilon\Gamma k^2\sin(2kz_o)\delta z^2. \tag{8.4}$$

The first term is the constant energy shift, the second one is a push/pull force of light pressure, the third is apparently the trap potential and the fourth is an extra potential created by the modification of the field due to the mirror. Depending on z_o, this total potential creates different mechanical effects: around $\sin(2kz) = 0$, a force is exerted on the ion which points either towards or away from the mirror; around $\sin(2kz) \pm 1$, a binding $(+1)$ or anti-binding (-1) potential is formed. Since the atom feels that extra potential only while it is in the excited state, the force exerted on an atom and hence the potential will be scaled by the probability P_e for an atom to be in that state. The trap potential then reads:

$$E = \frac{M}{2}\{\omega_{trap}^2 + \frac{2P_e\hbar\varepsilon\Gamma k^2}{M}\sin 2kz_o\}\delta z^2. \tag{8.5}$$

The binding/anti-binding potential at $\sin(2kz) = \pm 1$ is characterized by the oscillation frequency which an otherwise force-free atom would have in the respective potential well, $\omega_{vac} = (2P_e\varepsilon\Gamma\hbar k^2/M)^{1/2}$. By taking typical values for our experiment $P_e \approx 7\%$, $\varepsilon \approx 1.5\%$, $\lambda = 493$ nm, and $\Gamma = 2\pi \times 15.4$ MHz we get an estimation for that frequency, $\omega_{vac} \approx 20$ kHz. This is three times larger than recoil frequency $\hbar k^2/2M \approx 6$ kHz, this is why, in principle, one can trap an atom or an ion in this mirror potential, and it will not be kicked out of the that trap during a photon emission process.

For an ion which is already confined with trap frequency ω_{trap} (typically around $2\pi \times 1$ MHz), the potential $U(z)$ which is written above adds to the trapping potential, thus changing the trap frequency according to $\omega'_{trap} = (\omega_{trap}^2 + \omega_{vac}^2\sin(2kz))^{1/2}$. Since the deviation $\delta\omega_{trap} = \omega'_{trap} - \omega_{trap}$ is small, it is well approximated by

$$\delta\omega_{trap}(z) = \frac{P_e\varepsilon\Gamma\hbar k^2}{M\omega_{trap}}\sin(2kz) \quad . \tag{8.6}$$

It is this change of the trap frequency or macro-motional sideband frequency, a direct mechanical action, which we measure in the experiment.

8.2 Level shift measurement via detection of an ion motion

The experimental setup is shown in Fig. 8.1. The optical and electronic part of the setup is fully identical to that which has been described in Section 7. The counting signal on the PMT exhibits high-contrast interference fringes as the ion-mirror distance is varied [6]. In the present chapter we will describe the situation, where the beam B was used for the cooling and illuminating of the ion. In that case the interference contrast is about 40%. The deviation of the count rate from a chosen offset value is used in a feedback loop to control the position of the mirror such that the ion stays at a given point on an interference fringe to within ~ 10 nm. The feedback loop has about one second of integration time and compensates for slow drifts of the ion-mirror distance but not for the ion's oscillation in the trap. By switching the sign of the feedback gain, we choose between the positive and negative slopes of the interference fringes. This interference signal follows the $-\cos(2kz)$ dependence of the modified 493 nm decay rate [15], such that the midpoints of the slopes correspond to $\sin(2kz) = \pm 1$, i.e. to the maximum binding or anti-binding potential, as described above (see also Fig. 8.7 below). The trap frequency is measured by spectrally analyzing the PMT

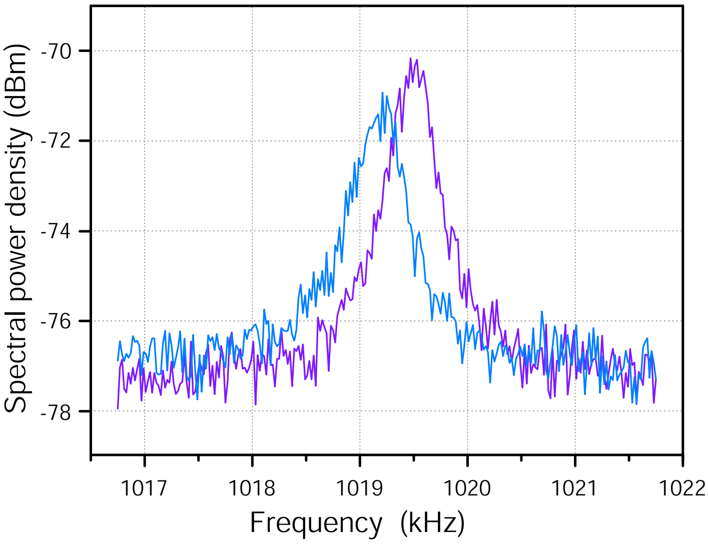

Figure 8.2: Signal on the spectrum analyzer for the ion positioned on the positive (right curve) and negative slope (left curve) of the interference signal. RBW = 10 Hz. The center frequency of a Lorentzian fit to the data is taken as the trap frequency.

signal. It contains a spectral component at the trap frequency, around 1 MHz, because the oscillation of the ion creates an intensity modulation of the scattered light. We observe oscillations of the x-sideband at frequency $\omega_x \approx 2\pi \times 1020$ MHz. The signal on the spectrum analyzer has, to good approximation, a Lorentzian line shape with width Δf of about 500 Hz. After a few seconds of averaging, the center frequency of the line is determined with less than 10 Hz inaccuracy.

Fig. 8.2 shows two spectra which were recorded directly one after the other, with the ion positioned at the midpoints of a positive and negative slope of the interference signal, respectively. The averaging time for each spectrum is about 20 sec. The shift is clearly visible and amounts to 310 Hz in this case. The value is within the range expected from Eq. 8.6, which predicts around 350 Hz, taking typical values for our experiment $P_e \approx 7\%$, $\varepsilon \approx 1.5\%$, $\lambda = 493$ nm, and $\Gamma = 2\pi \times 15.4$ MHz. We emphasize that no changes are made to the setup between the recording of the two spectra, apart from translating the distant mirror by $\lambda/4$.

It was found that the trap frequency is not constant in time due to thermal effects and slow changes in the trap drive power. To measure the value of the frequency shift in this situation we record about 60 spectra, alternating between the two slopes. It takes about 10 seconds to record each spectrum, the number of averages on the spectrum analyzer was set to 25. Each spectrum is fitted by a Lorentzian, and the center frequency is plotted. An example is shown in Fig. 8.3. While the trap frequency itself slowly varies, a constant difference is observed between the values measured on

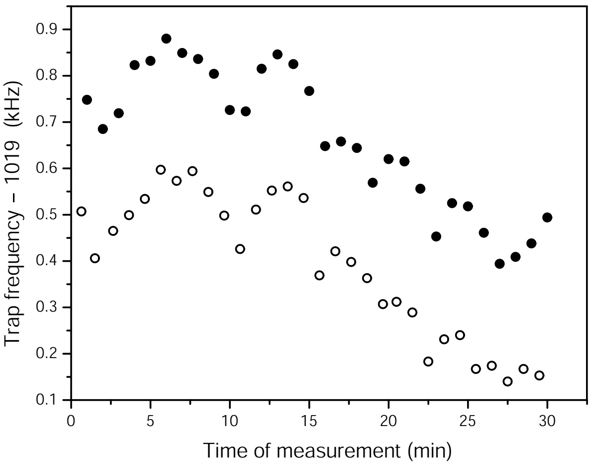

Figure 8.3: Trap frequency measured on the positive (full circles) and negative slope (open circles) of the interference signal, vs. measurement time, using the B cooling beam.

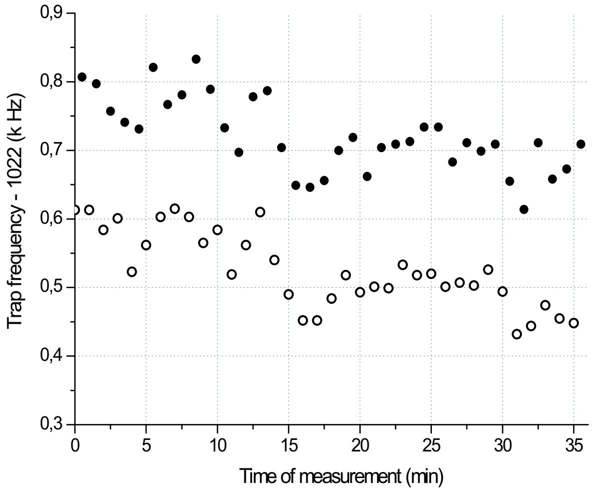

Figure 8.4: Trap frequency measured on the positive (full circles) and negative slope (open circles) of the interference signal, vs. measurement time, using the F cooling beam.

the two slopes, $\delta\omega_{trap}$= 284 ± 12 Hz.

The precise value of the shift depends on details of the experiment such as the settings of the lasers, their directions, and the fine alignment of the back-reflecting mirror. The trap frequency evolution when the ion is illuminated from F direction is shown in Fig. 8.4. The value for the trap frequency shift is smaller for this case. For the F beam $\delta\omega_{trap}$= 195 ± 5 Hz. For the main beam direction the frequency shift is less

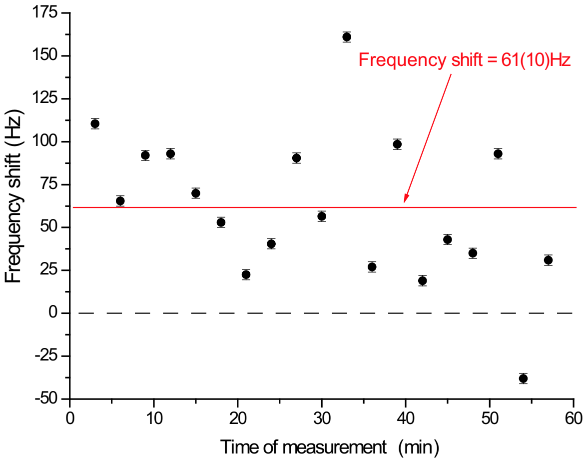

Figure 8.5: The trap frequency shift measured vs. measurement time. The main cooling beam is used.

than even in the previous case. To measure the frequency shift we set the ion position to the different slopes, just right one after the other. Sideband spectra are taken with an averaging time of approximately 30 seconds. An example of the evolution trap frequency shift is shown in Fig. 8.5, we can find that $\delta\omega_{trap}$= 60 ± 10 Hz.

We believe this essential difference in the trap frequency change occurs because the cooling beam induces a dipole moment with different direction with respect to the mirror's plane and a different amplitude. And with our present theory it is hard to obtain the numerical value for the shift when the ion is illuminated from different directions. Nevertheless, we observe values between 50 and 350 Hz, all within the range expected from Eq. 8.6. It is important to note that we always find the higher trap frequency on the positive slope of the interference fringes (count rate vs. ion-mirror distance), in agreement with the theoretical prediction [15].

8.3 Frequency shift versus probability to be an exited state

As shown in Eq. 8.6, the trap frequency shift depends on the laser parameters through the probability P_e with which the ion is found in the excited state. This dependence has been measured by recording the maximum shift for different laser parameters. The mean fluorescence level, at the midpoint of the interference fringes, serves as an indicator of P_e, to which it is strictly proportional. The result is displayed in Fig. 8.6. The data agree well with the expected linear dependence. Nevertheless, for laser intensities approaching saturation we find that the shift saturates, the reason being that in this regime laser cooling becomes inefficient, and the ion's excursion in

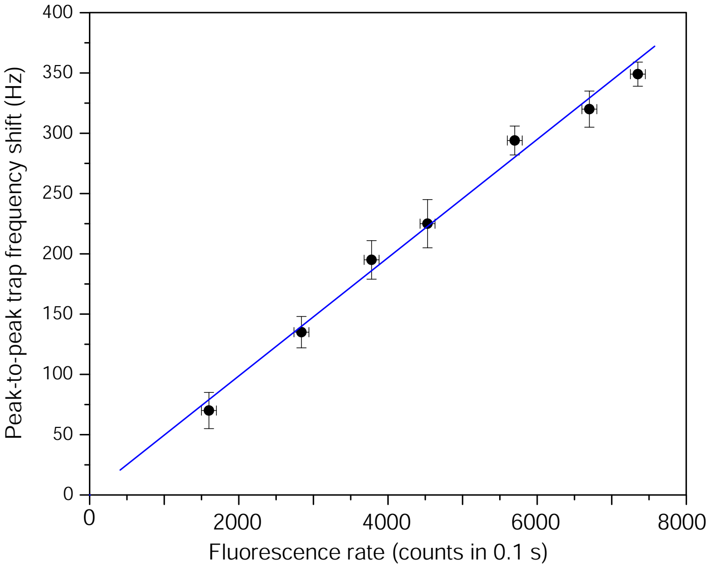

Figure 8.6: Measured dependence of trap frequency variation on excited state population P_e. The peak-to-peak difference, between the midpoints of the two slopes of the interference fringes, is plotted vs. the mean count rate. 10000 counts correspond to $P_e \approx 0.1$. The line is a linear fit.

the trap averages out the mechanical potential.

A similar effect is observable in the RF domain, where the force is exerted on the active and passive elements of the antenna. Note, that the resonance frequency shift of the antenna does not depend on the current, however the force does! This frequency shift depends only on the geometrical configuration of the antenna and arises as a result of a back-reaction on its own field. Hence in the case of an atom near the mirror, the argument that a frequency shift does not depend on the intensity of fluorescence light, as in [15], cannot be used as a proof of action of the vacuum field. This effect can be treated as a reaction on its own reflected field. We can drive the antenna with the highest possible current (until it starts to melt down), the shift of the resonance frequency still will remain the same, but the force which acts on antenna elements will be proportional to the magnitude of the current. The situation with the frequency shift for the atom is identical to the case of the antenna, but the force which exerts on the atom can not exceed a particular value due to the saturation of the excited state.

8.4 Trapping forces

A further test is the dependence of the trap frequency on the position of the mirror. We shift the ion between the maxima and minima of the interference fringes, by locking its positions to different fluorescence levels (between 5000 counts to 11000 counts per

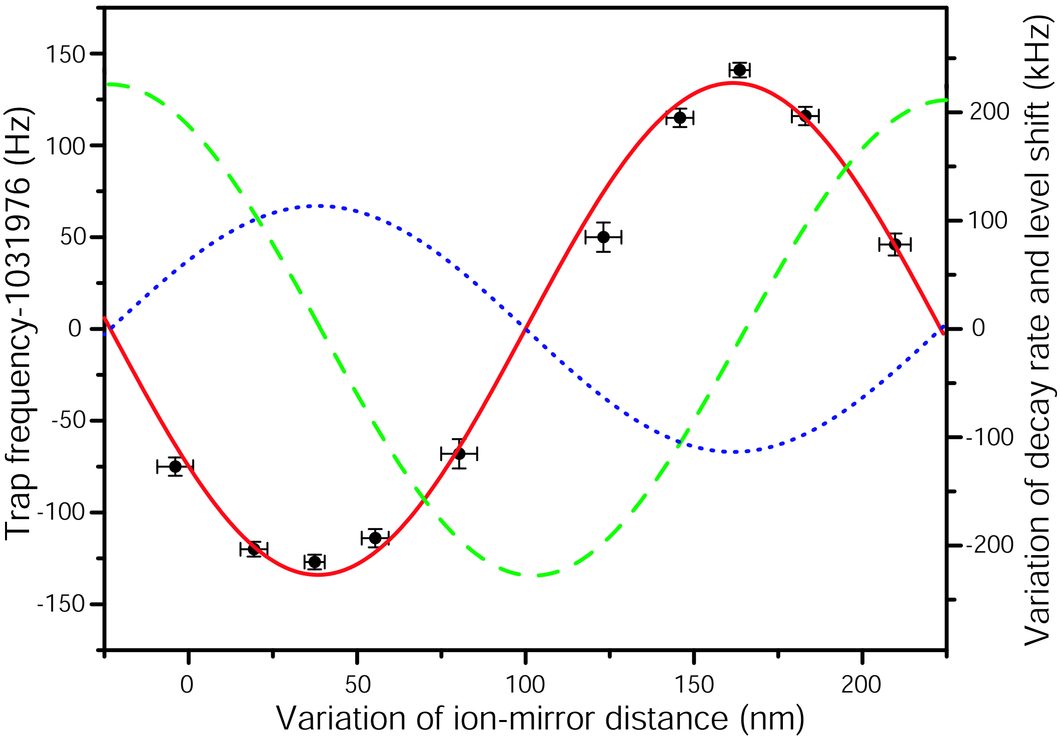

Figure 8.7: Measured variation of the trap frequency with ion-mirror distance (points). The solid line is a fit to the data. The dashed line shows the corresponding variation of the spontaneous decay rate on the S-P transition, and the dotted line is the shift of the excited level, i.e. the mirror-induced potential divided by $\hbar$. The dashed and dotted lines use the right-hand vertical scale.

100 ms) and measure the trap frequency as a function of this ion-mirror distance. The result is shown in Fig. 8.7. The sinusoidal variation predicted by Eq. (8.6) is clearly observed. The distance is adjusted by varying the signal level to which the ion's position is stabilized. This data set showed particularly small drifts of the trap frequency. The calculated maximum force from that graph, acting when the atom is positioned on a maximum or minimum of the dashed curve, corresponds to an acceleration of $\sim 100\ g$.

Unfortunately in the present setup it is impossible to demonstrate the real trapping effect, where the atom remains at the same place for a sufficient long time interval, because the trapping potential induced by the mirror has a depth of only about 1 μK. And this is very small compared to the thermal energy of the laser cooled ion. Nevertheless, trapping forces change the motional state of an ion in the Paul trap, i.e. its oscillation frequency, and that can be easily observed by measuring the spectrum of the intensity fluctuation.

Here we want to return again to the problem of the interpretation of the observed effect. One may construct a semi-classical explanation for the observed effect. Namely, that a maximum in the interference fringes at the PMT indicates increased emission caused by light returning from the mirror. This returning light stimulates additional radiation towards the PMT thus yielding a small recoil towards the mirror. Conversely, a minimum in the interference fringes corresponds to radiation returning from the mirror being predominantly absorbed which therefore leads to a force away from the mirror. However, quantum mechanical properties of the electromagnetic field are needed to explain quantitatively the spontaneous emission rate from an atom [18, 22, 49]. For example, without invoking the vacuum field the theory becomes mathematical inconsistent, due to breaking of commutation rules!

8.5 Vacuum versus self-reaction

The notion of the vacuum field seems to be an elegant way to describe many phenomena in QED, such as enhanced and inhibited spontaneous decay, the Lamb shift, the Casimir force, etc. For example, if we look at the experimental setup which is described in this thesis: the vacuum fluctuations which are created somewhere in the space surrounding the ion will be reflected back by the mirror, thereby standing waves of the vacuum field appear. The inhibited and enhanced spontaneous emission can then be explained by as being due to different coupling strengths between the atomic dipole and the vacuum modes, which depends on the position of the atom in the standing wave.

One can look at atomic spontaneous decay itself more deeply and interpret it as being induced by the vacuum fluctuations only. However, this point of view is an oversimplification of the physical picture. Actually, the QED description of the atom coupled to the quantized field allows us to interpret the spontaneous decay or level shift in at least three ways, see [18] and references therein. For a deeper understanding at the interpretation problem let us examine the Maxwell equation for the field.

The Maxwell equations have the same form in classical and quantum electromagnetic theory, but in QED the field are operators in a Hilbert space. Moreover, field operators commute with atomic operators resulting in a different physical interpretation during the process of the formal solution of the Schrödinger equation.

The simplest Hamiltonian of the interaction two-level atom and single mode quantized electromagnetic field is

$$H = \frac{1}{2}\hbar\omega_a\sigma_z + \hbar\omega_l a^+ a + i\hbar C[a + a^+][\sigma_- - \sigma_+] + \frac{e^2}{mc^2}\mathbf{A}^2, \tag{8.7}$$

where ω_a and ω_l are the atomic transition and the laser frequencies respectively, σ_z is the atomic energy operator, σ_+ and σ_- are the atomic raising and lowering operators, C is the coupling constant between the atomic dipole and the field and $\mathbf{A}$ is the vector potential of the electromagnetic field. The last $\mathbf{A}^2$ term in the Hamiltonian can be neglected in the dipole approximation, since it does not cause an observable level shift or change of the spontaneous decay rate. From this Hamiltonian we formally get the Heisenberg equations of motion

$$\dot{\sigma} = -i\omega_a\sigma + C[a + a^+]\sigma_z, \tag{8.8}$$

$$\dot{\sigma_z} = -2C[a + a^+][\sigma + \sigma^+], \tag{8.9}$$

$$\dot{a} = -i\omega_l a + C[\sigma - \sigma^+]. \tag{8.10}$$

Since the atomic and field operators commute, the Heisenberg equations 8.8 and 8.9 can be rewritten in different, but mathematically equivalent, ways by using different operator orderings. For example, one can use normal ordering, then Eq. 8.8 reads

$$\dot{\sigma} = -i\omega_a\sigma + C[\sigma_z a + a^+\sigma_z], \tag{8.11}$$

one can use anti-normal operator orderings, then the same equation will be given by

$$\dot{\sigma} = -i\omega_a\sigma + C[a\sigma_z + \sigma_z a^+]. \tag{8.12}$$

Another ordering of interest is symmetric ordering which yields

$$\dot{\sigma} = -i\omega_a\sigma + \frac{1}{2}C[\sigma_z(a + a^+) + (a + a^+)\sigma_z]. \tag{8.13}$$

To see how these different ordering schemes result in different interpretations, let us write the formal solution of Eq. 8.10 for the field operator, $a(t) = a(0)e^{-i\omega_l t} + a(t)$. Here, the first term is the source-free part which corresponds to the vacuum field and the second term is the source field or the atomic radiation field. Then, by substituting this solution into Equations 8.11, 8.12 or 8.13 and by taking the expectation values for atomic operators over the atom-field state $|\psi\rangle|vac\rangle$, where $|\psi\rangle$ is the wave function for the atom, and $|vac\rangle$ denotes the vacuum state for the field, we will see that the contributions from the vacuum field and source field are different for different operator orderings. For example, in the normal ordering scheme there is a contribution only from the source field (SF), in the anti-normal scheme the complete answer is quite exotic and equals 2×Vac−SF and for the symmetric case the vacuum and source fields contribute equally (i.e. 50% contribution from each field).

The numerical answer for all types of level shifts (Lamb shift, van der Waals shift, resonance radiative shift) and for decay rates is the same regardless of the operator ordering scheme. This suggests that these interpretations are in the physical sense quite close. Perhaps, to find out what the true physical picture is, an experiment must be made where the contribution of the source field and vacuum field can be separated. For example, by taking our experimental situation – a single atom in front of a single mirror – one can ask the question: "Does the atom see the mirror before it emits the light?".

Let us assume that the laser excited atom is placed at a distance L, close enough to the mirror, i.e. the coherence length of the emitted photon is much larger than the atom-mirror distance ($c/\Gamma \gg L$). The total field in the vicinity of the atom equals $E_{tot} = E_{Vac} + E_{SF}$. Then the excited level shift and the decay rate will have contributions from the vacuum and from the source field (symmetric operator ordering scheme). However, being in the excited state the atom will "see" the mirror after a time $2L/c$, and then the level shift and the decay rate change will get the contribution from the retroreflected field as well, and then it is impossible to interpret the effect unambiguously: either it comes from the vacuum field or from the source field. But it would be possible to make a conclusion about the effect when the atom is still "blind" or has not "seen" the presence of the mirror. This corresponds to the situation when the atom is in its ground state. To measure that moment, an additional photodetector can be installed near the atom, and when it "clicks" it will simply mean that the atom has emitted the photon. Since this happens during a time $\tau \sim c/\Gamma$ we would have to measure the level shift or the decay rate. If the answer in that experiment is the same as for usual measurements (see the section 8.2), then we can conclude that there is no vacuum field action, and all the contributions to the level shift and decay rate come from the source field only [20]. If the answer is different, it would be interesting to know numerically what would be the ratio between these two cases.

In our setup, we can use a photomultiplier to measure the intensity of the red light, see Fig. 2.3, this could be the detector of the ground state. Then we can try to perform the measurement of the trap frequency shift or the decay rate change (perhaps, via G^2 function measurements) during a time when the atom does not "see" the mirror. A similar experiment is discussed in article [81].

There is an interesting idea to separate the action of the vacuum field from the source field in [22]. In that article the authors are discussing how to compare numerically the force acting on a single atom placed in front of a mirror, in the near-field and far-field zones. In the first case, the total force affecting the atom will be the sum of the Casimir-Polder and van der Waals forces, whereas in the second case, the force is mainly the resonant-radiative force or the reaction of the atomic dipole on it's own retroreflected field, i.e. exactly the force which has been measured in our experiment!

Perhaps, it would also be very interesting to use a light source which, depending on certain parameters, could be considered either as a classical antenna or as an atom obeying quantum mechanics. This may be possible for atoms in highly excited states, or Rydberg atoms [82]. In that case we could compare numerically the total radiated power of "the antenna" and "the atom", see [49]. If the dipole moments of these sources are the same, then due to the coupling to the vacuum field the atom in free space will radiate with twice the power of the antenna [18, 22].

9 Observation of an ion's macro-motion in real time

Spectral analysis in the RF-range of the resonance fluorescence of a single Ba^+ ion in the interference experiment has been described in chapter 7. It was shown that macro-motional sidebands appear in the spectrum of the resonance fluorescence as a sharp resonances, and the averaged frequency and amplitude of the ion's motion can be measured. Information about the ion's instantaneous position as well as the phase of it's oscillation can be measured in the experiment which will be described in this chapter. A homodyne technique was used, i.e. the photocurrent is mixed with some carrier frequency down to a DC range to reconstruct the trajectory of the ion. The signal of the ion's motion after homodyne detection looks like noise, we therefore use a feedback based on a phase locked loop (PLL) not only to prove that the signal we observe is the ion motion in the Paul trap but to synchronize the phase of ion's oscillation to the phase of pure sinusoidal or FM-modulated external signal.

9.1 Experimental setup

The experimental setup is shown in Fig. 9.1. The optical setup is the same as described in chapter 7. Ion oscillations occur at an angle of 55° with respect to the optical axis Z. The fringe lock sets the ion-mirror distance such that the ion moves through the middle of the slope of an interference fringe. The motion of the ion through this field leads to an intensity modulation of the resonance fluorescence which can be measured in the present experimental setup. By taking into account the fact that the ion oscillates almost with the same frequency (the sideband is a narrow resonance line) Equation 7.2 can be rewritten as:

$$i(t) \approx I_o + 2VI_o k\mathbf{z}\mathbf{x}(t)e^{-i\omega_x t+i\phi(t)}, \tag{9.1}$$

where **z** is a unit vector along the optical axis, x(t) is the slowly varying amplitude of the ion's oscillations, and ω_x and $\phi(t)$ are the frequency and the phase of the ion's macro-motion. The phase of the macro-motion is also a slowly varying function of time, and its changes, or even jumps, are mainly due to the cooling process during which the ion gets a momentum kick.

The photocurrent is fed to a quadrature detector, which consists of a local oscillator (LO), a mixer stage and low-pass filters. The LO creates two signals with a frequency

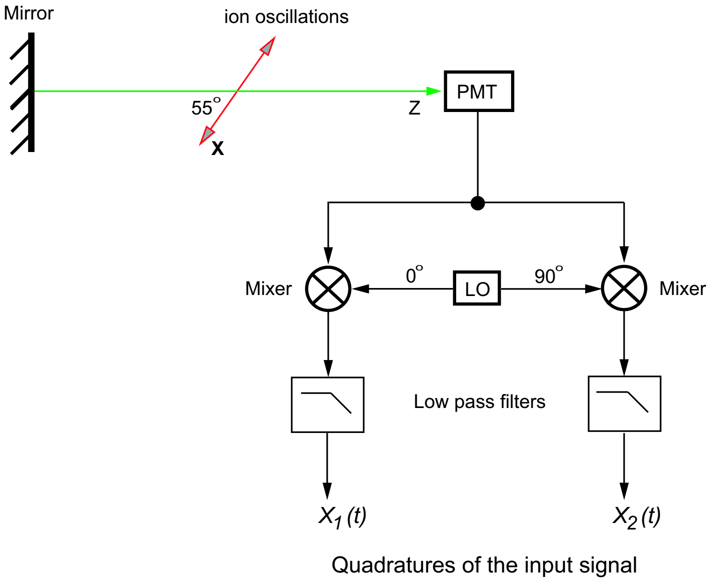

Figure 9.1: The experimental setup to detect the amplitude and the phase of the ion's oscillations with the help of an electronic homodyne technique.

equals to the frequency of the ion's oscillation, and the phase of each signal is shifted by 90° with respect to each other. The quadrature components of the photocurrent is mixed to DC range and low-pass filtered it to remove signals at the doubled frequency. After filtration the resulting quadrature signals are amplified using a 40 dB gain amplifier stage, and is recorded on a two-channel digital oscilloscope.

The low-pass filter has a 3 dB bandwidth of about 25 Hz, and a 40 dB stop band of about 700 Hz. The signals after demodulation and filtration can be written as

$$X_1(t) = \mathbf{x}(t)\mathrm{cos}\phi(t) + n_{x1}(t), \tag{9.2}$$

$$X_2(t) = \mathbf{x}(t)\mathrm{sin}\phi(t) + n_{x2}(t), \tag{9.3}$$

where $n_{x1}(t)$ and $n_{x2}(t)$ are quadrature components of the Poissonian noise which arose during detection process. The signals $X_1(t)$ and $X_2(t)$ contain all the information about the amplitude and the phase of the ion's oscillation. The amplitude of the ion oscillations will then be $x(t) = \sqrt{X_1^2(t) + X_2^2(t)}$ and its phase with respect to the phase of the LO is $\phi(t) = \arctan(X_2(t)/X_1(t))$.

After filtration the spectral density of the noise is not changed, but the bandwidth of the noise will be equal to the bandwidth of the filter. The signal-to-noise ratio can be estimated from sideband spectra, see for example Fig. 7.6, and one can obtain SNR ≈ 2.5.

The spectrum of motion has a Lorenzian shape, see Fig. 7.6, and occupies a sufficiently large band (compared to the band of low-pass filter), therefore the signal-to-noise ratio in the detector will be inversely proportional to the bandwidth of the filter. A larger bandwidth of the low-pass filter transmits more noise. With a 25 Hz low-pass filter we select only the top of the motional spectra, and then the signal-to-noise ratio is about 7 dB for the measuring the ion trajectory oscillating on X-mode. It gives approximately ± 20% error in the detection of the "instantaneous" position of the ion after approximately 10 ms averaging.

9.2 Calibration of the motion

The first step is to observe externally excited motion of the ion, which can be done relatively easily by supplying an ac-voltage near the ion's resonant frequency from an external generator to the end caps, as done in [75]. At first glance it seems that this cannot be done because the oscillation lies in the ring plane, and the line which connects the end caps (direction of the excitation field) will be orthogonal to the X- and Y-modes of the ion's oscillations, see Fig. 2.2. Nevertheless, we assume that due to the small asymmetry of the position of the end caps with respect to the ring plane, there will be a projection of the electrical field created by the end caps on the ion's motion along the ring plane. Therefore the ion starts to oscillate at the frequency of the external excitation with an amplitude which depends on the amplitude of the excitation voltage and its detuning from resonance. The spectrum of the sideband which is resonantly excited by the external sinusoidal signal of an amplitude of –47 dBm is shown in Fig. 9.2.

The excitation spike is approximately 17 dBm above the Poissonian level and is clearly observed on the sideband spectrum. In a linear approximation the signal size is proportional to the amplitude of an ion's oscillation multiplied by the interference contrast. Here we assume that the amplitude of the externally excited motion is proportional to the amplitude of the excitation AC-voltage. The visibility of the interference fringes decreases with increasing size of the ion excursion, because of the ion motion washes out the interference. Therefore, the fringe visibility decreases with increasing excitation voltage. To calculate the contrast of the interference fringes V_{exc} during external excitation the following formula is used [44]:

$$V_{exc} = V_o exp(-2k^2\overline{\sigma^2}), \tag{9.4}$$

where V_o is the visibility of the interference when no driving field is applied, and σ - is the amplitude of the excited ion's oscillations (which is averaged over the period of the oscillation). The amplitude of the excited oscillations can then be determined

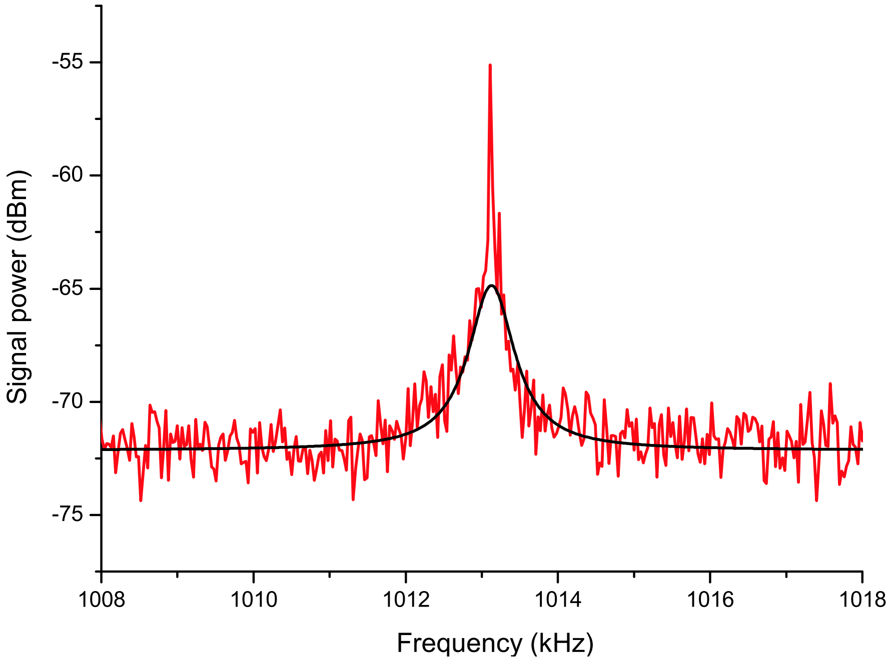

Figure 9.2: The sideband spectrum during external excitation, RBW = 30 Hz. The black curve is a Lorentzian fit to the sideband taken when the excitation is off.

from measurements of the interference contrast when the driving field is applied from formula

$$\sigma = \frac{\lambda}{2\pi}\sqrt{ln(V_{exc}/V_o)}. \tag{9.5}$$

For example, if the amplitude of the driving field is −47 dBm then the interference contrast drops from 46% to 30%. By using equation 9.5 the amplitude of the projection of an ion oscillation onto the optical axis can be calculated. This amplitude is about 53 nm. The excited motion takes place in the direction of the X-mode, and the amplitude of the excited motion is therefore equal to 93 nm.

These oscillations can be observed using a homodyne detection technique. For this purpose the frequency of the LO is detuned by 1.5 Hz from the frequency of the driving field, hence a beat-note waveform must appear as the signal. In Fig. 9.3 the X_1-component of the detected signal is shown. The X_2-component of the signal has a 90° phase difference. Therefore, the phase plot of the motion, i.e. the X_2-component versus the X_1-component, will be a circle in that case. The radius of the circle gives the amplitude of the ion's motion and is equal to 93 nm, the frequency of the motion being the same as for the driving field. Oscillations take place along the X-mode of the macro-motion.

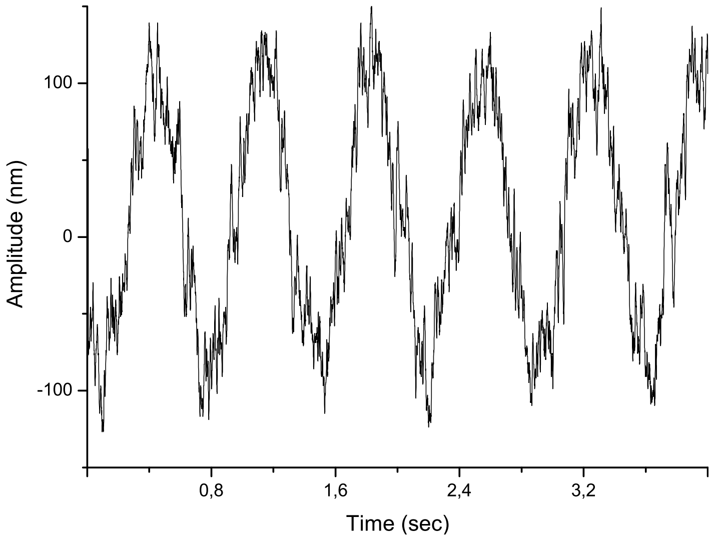

Figure 9.3: The observed X_1-component of the excited ion oscillation using the homodyne detector when the LO frequency is 1.5 Hz detuned from the resonance frequency.

9.3 Observation of ion motion

To observe the ion's thermal motion or its macro-motion the LO has to be tuned exactly to the center of the sideband. The gain of the detector is the same as before in the case of the motion calibration. This is in order to obtain the same voltage-to-distance conversion coefficient. The X-component of the detected signal is shown Fig. 9.4.

The amplitude of the ion macro-motion can be calculated using the voltage-to-distance conversion coefficient, known from the excited motion measurements, and also by taking into account the decreased fringe visibility when the driving field is applied.

To extract full information about the ion motion, or to reconstruct the trajectory of the ion's macro-motion, the phase and amplitude must be observed simultaneously, these measurements are shown in Fig. 9.5. The average amplitude of the macro-motion calculated from the graph is $A = 27 \pm 6$ nm, which corresponds to a mean phonon number $\overline{n} \approx 10$, which is in good agreement with the expectation value for the size of the wave packet during Doppler cooling. The temperature of the ion or more correctly it's thermal energy can be calculated from the average amplitude of the oscillations, or from the mean phonon number: $kT \approx \hbar\Omega(\overline{n} + \frac{1}{2}) = \frac{1}{2}M_{Ba}\Omega^2 A^2$. This yields in our case $kT/\hbar \approx \Gamma/2 = 10$ MHz.

The accuracy of the amplitude measurement is limited by the presence of Poissonian noise and can be determined by taking measurements to those described above. To pick up the noise signal the LO is detuned by about 3 kHz from resonance to avoid the influence of the sideband signal. The detected signal is now due to the Poissonian

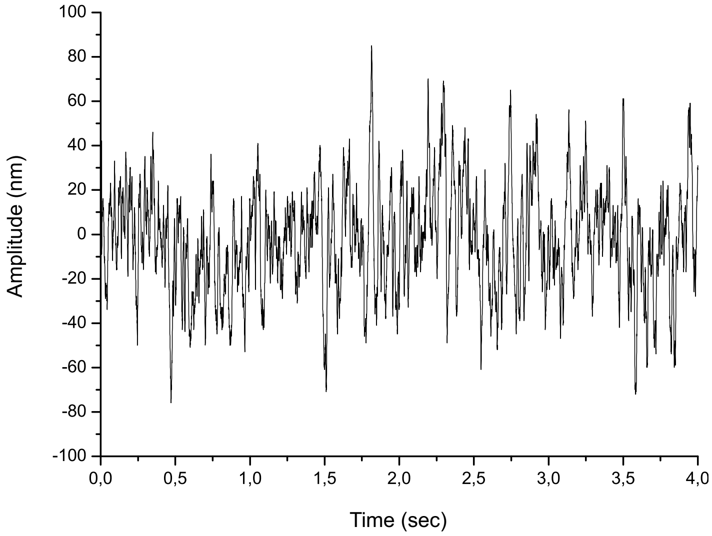

Figure 9.4: The observed X_1-component of the ion macro-motion using a homodyne detector. The LO is tuned exactly to the center of the sideband.

noise only, and it's RMS amplitude is approximately equal to 12 nm. This is the detection limit for our measurement method, or standard quantum limit (SQL) in our measurement scheme [34].

The SQL can be beaten by either increasing the intensity collected from a single ion, or decreasing the width of the low-pass filter. The first solution could be implemented in the future setup only. One can try to use an objective with a higher aperture, but special cares must be taken to avoid optical aberrations, as they decrease the contrast of the interference fringes. The second solution simply requires the increase of the integration time for the reconstructed motional signal. Therefore, all the fast features of the ion motion will be averaged, and the meaning of the "real time" measurement in that case is the sequential measurements during time intervals which are inversely proportional to the bandwidth of the low-pass filter.

The next step will be to introduce a control of the ion motion with the help of an active feedback. The first step will be to introduce a feedback based on phase-locked loop. This kind of feedback allows us to encode and decode phase/frequency information into the ion motion.

9.4 Phase locking of ion macro-motion

9.4.1 Experimental setup

The experimental and electronic setup for PLL feedback is shown in Fig. 9.6. The optical part is the same as for the interference experiment and for the experiments

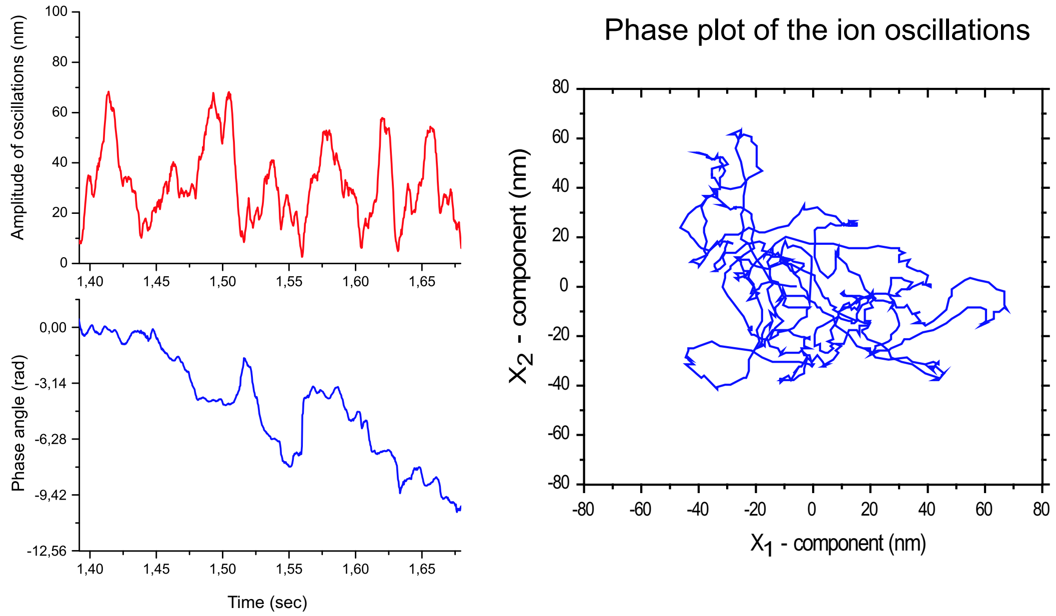

Figure 9.5: The amplitude of the ion's macro-motion and its phase relative to the LO measured by a homodyne detector (left side). To see the behavior in detail, a smaller scale in the horizontal axis is used than in Fig. 9.4. On the left side – the 50 ms phase plot of the part of the right handed graph.

which have been already described, see chapters 2 and 7. The electronics however is quite different even from the experiment described just above (see section 9.1). In the next three paragraphs some technical details of the PLL feedback are introduced.

The PMT pulse train from the pulse discriminator is split by a PSC-2-1 combiner/splitter. One part is spectrally analyzed with the FFT spectrum analyzer, another part is low-pass filtered at 1.9 MHz (not shown on the figure for clarity) and then sent into the phase-locked loop. The PLL used in our experiment has a standard design [83], and consists of a phase detector, a voltage-controlled oscillator (VCO) and a loop filter.

The phase detector in our setup is an analog modulator/demodulator AD630. We found that this chip works quite well with a signal frequency up to 1.8 MHz and –65 dBm amplitude. The input amplifier stage in that chip has an impedance of 5 KΩ, therefore we use the non-inverted buffer based on an AD811 to obtain the frequency

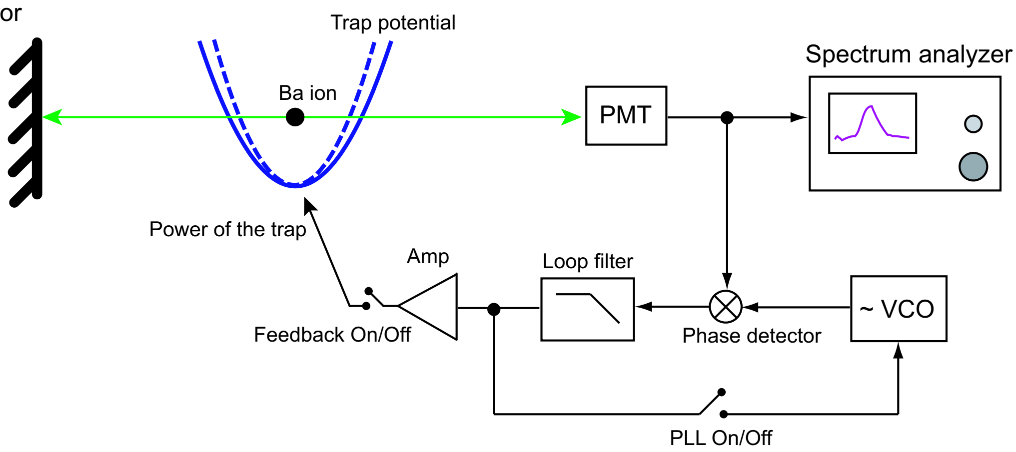

Figure 9.6: The experimental setup for phase-locking the motion of an ion motion in a Paul trap.

bandwidth on the order of a few MHz.

The measured input signal has a level of approximately –54 dBm, that is why a high quality VCO with a low SSB phase noise must be used. In the present setup we use a signal generator (Rhode and Schwarz SML-01) in the external frequency modulation regime. Our generator has about –123 dBm SSB phase noise 1 kHz away from the signal frequency of 1 MHz. This measurement was performed with RBW = 10 Hz. The sensitivity of the oscillator, i.e. the voltage to the frequency conversion coefficient K_v, can be tuned up to 200 kHz/Volt. The amplitude of the control signal must not exceed 0.5 V (this is a demand of the modulation input of our signal generator or VCO).

The loop filter can be switched between a third and second order low-pass filter with different bandwidths. All filters have a flat amplitude response for frequencies below 3 dB level. The shape of the loop filter can be chosen so that more than 75% of the sideband energy resides in the loop and the 45° cross-over point lies further than the HWHM of the sideband. This is done to provide the best collection of the signal energy. We use an active filter design using an OP-77 operational amplifier in multiple-feedback configuration, see [84], for example. The actual filter response has been calculated by using special programs, for example Micro-Cap 7.0.

Part of the PLL DC-output is used to control the power of the trap, hence it will change the sideband frequency as well, depending on the frequency difference between the sideband and the LO. The control signal has a small amplitude, on the order of several millivolts. For example, the sideband frequency changes by 1 kHz if 7 mV is applied to the trap power control (which is shown as an Amp in Fig. 9.6). The amplitude of the control signal can be varied by the amplifier with variable gain just after the loop filter (not to be confused with the trap power control). In the following sections the gain of that amplifier stage will be called the feedback gain.

Thus the PLL circuit described above can function in three different modes. These modes are:

- Tracking of the instantaneous frequency of the ion.
- Phase-locking of the ion's motion to the primary generator.
- Phase-locking of the ion's motion to the center frequency of the sideband signal.

9.4.2 Tracking the instantaneous frequency of the excited ion motion

To work in the tracking regime the switch "Feedback", see Fig. 9.6, must be off, and "PLL internal" must be switched on. In the case of the ideal locking conditions the VCO output frequency will follow the phase of the ion's motion, and the VCO input will be equal to the "instantaneous" frequency of the ion's motion. By measuring the VCO input voltage the frequency of the ion's oscillation can be determined and the phase of the output VCO signal reveals the phase of the ion's oscillation.

To demonstrate this mode, we first excite the motion of the ion with an external FM-modulated driving field of amplitude –40 dBm at a frequency which is 3 kHz away from the sideband center. For that purpose a SRS-235 signal generator phase-locked onto a 10 MHz time base signal supplied by the VCO (the time-base output at the rear panel of the signal generator) was used. The spectrum of the ion's excited motion is shown in Fig. 9.7. The frequency span for the FM modulated driving signal is 30 Hz and the frequency rate for that signal is 10 Hz.

From a technical point of view, the signal which we want to lock onto is about 15 dBm above the noise observed with a RBW = 3 Hz. This signal is quite small and the presence of the noise will try to destabilize the PLL from lock conditions leading to a phase error, see for example [85]. Therefore, to increase the performance of the PLL, i.e. to decrease its phase error, the loop filter must have a smaller possible bandwidth. On the other hand the smaller bandwidth means that the PLL can not reveal the phase/frequency information as precisely as possible [83]. The rule of thumb would be to take a filter with a bandwidth which is slightly larger than the frequency span of the input signal. In our case a good choice for the loop filter is a PI-regulator with a 2nd order low-pass filter with a bandwidth of about 40 Hz.

The response of the phase-locked loop, or the VCO input voltage vs time is shown in Fig. 9.8. It is easily seen that the VCO input voltage tracks the instantaneous frequency of the driving field. The motion excited with that external field also has the same phase, hence the PLL locks onto the motional signal and follows the frequency of the excited motion.

There is a constant phase mismatch between the two signals of approximately 30°, which is due to a non-zero offset voltage inside the loop. The noise on the signal

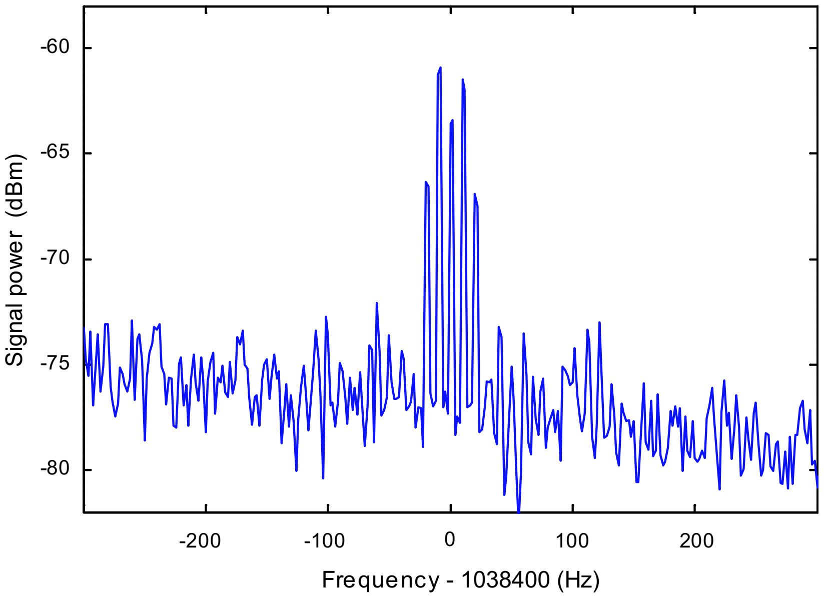

Figure 9.7: The spectrum of the ion motion during external excitation with an FM-modulated signal. Higher order sidebands are clearly seen. RBW=3 Hz.

is Poissonian noise and arises from the detection of the resonance fluorescence, the electronic noise of the circuit is approximately 40 dB less than the signal level.

The shot noise cannot be completely removed by lowering the bandwidth of the low-pass filter, as in that case the performance of the the PLL would also be worse, and it will not effectively follow the instant frequency of the signal.

To study the case when the instant frequency is changed quickly we tried to make a phase lock to a complex signal which is FM-modulated with rectangular and sawtooth waves. However, it was not as successful as using a sinusoidally modulated signal. At the input of the VCO we expected to see a modulation signal, i.e. rectangular or sawtooth, unfortunately due to the limited bandwidth of the loop filter it was not possible to reveal these features.

The detected macro-motion signal looks like noise, see Fig. 9.4, hence the phase detector output will also look like a noise. With this noise-like signal it would be hard to prove that we do indeed measure the trajectory or the instant frequency (depending on the experiment) of the ion rather than Poissonian noise. However, we are going to use a PLL feedback to show that we really can control the frequency and the phase of an ion oscillations. Therefore the next step is to synchronize the frequency of the ion oscillation to the frequency of the external generator.

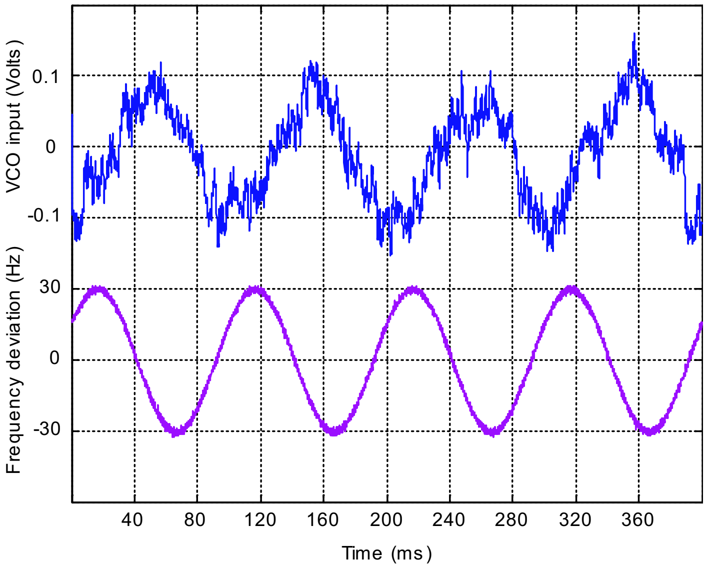

Figure 9.8: The upper curve is the time scan of the response of the phase-locked loop on the external FM excitation. $K_v = 160$ Hz/Volt. The lower curve is the time scan of the instantaneous frequency or frequency deviation of the driving field. A spectrum of excited motion is shown in Fig. 9.7.

9.4.3 Phase locking of a mono-ion oscillator to sinusoidal signal

The aim is to synchronize the phase of the oscillations of the single ion in the Paul trap to the phase of an external signal generator. Now we want that the sideband spectrum occupy as much of the bandwidth of the feedback loop as possible to prevent the loss of the phase information. For that purpose we use a single third order low-pass active filter with a bandwidth of approximately 300 Hz. The switch "Feedback" is now turned on, but the switch "PLL" is turned off.

This time, the oscillating signal of the ion motion will play the role of the VCO which can be synchronized to the phase of the external signal, as in the case of the classical design of the PLL [83]. The generator which was used as a VCO in the previous subsection is now the primary generator and makes the base signal to lock the ion oscillations onto it.

The first step in the PLL experiment is to lock the ion motion to the external frequency source (again the signal synthesizer SML-01). The frequency of that signal is kept constant and has to be around the sideband center (the motion response is maximal there). The spectrum of the sideband when the PLL is in locking conditions is shown in Fig. 9.9. It can be seen that the 7 dB narrow spike appears on the top of the sideband showing that the ion motion becomes coherent. The pedestal around that spike is treated as phase noise of the PLL. That spectrum is known to belong to the phase-locked signal, see [83], and indicates that the PLL does function and the ion oscillations are synchronized to the external generator.

The sideband evolution with feedback gain is shown in Fig. 9.10. A small coherent spike appears at low gain and increases as the feedback gain is increased, reaching it's maximum value at a gain of approximately 1. The coherent spike decreases again for higher gain due to the saturation of the feedback loop. The wings of the sideband become broader with increasing PLL gain, and although the sideband spectrum becomes about twice as broad in locking conditions, the total area (thermal energy) of the sideband remains the same. Therefore, we conclude the PLL feedback does not change the energy of the ion's oscillation on the locked mode, and perhaps, could not even be used for cooling or heating purposes.

The sideband spectrum taken with feedback gain G = 1, see Fig. 9.10 looks like a classic servo signal under lock conditions. The coherent spike has an amplitude of approximately 7 dB above the sideband floor, and 11 dB above the Poissonian noise level, taken with a RBW = 10 Hz.

It is interesting to find out the bandwidth of the coherent spike. When measured with the narrowest resolution of FFT spectrum analyzer (RBW = 1 Hz), the narrow phase locking spike is observed with an amplitude of 20 dB above the noise pedestal,

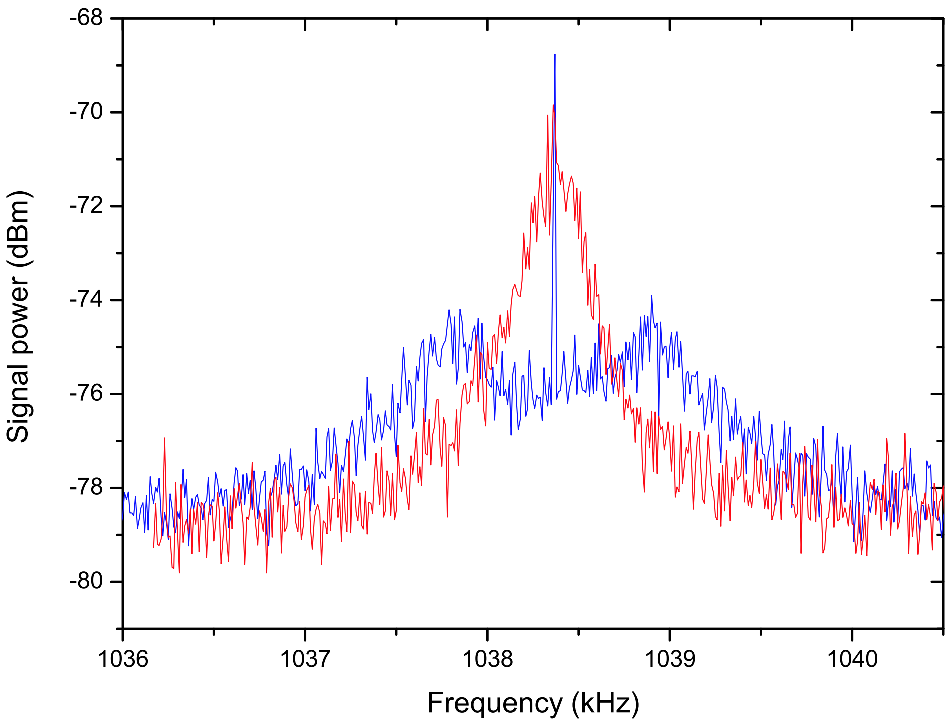

Figure 9.9: The red curve is the sideband spectrum of the free ion oscillation. The blue curve is the sideband spectrum when ion oscillation is locked to an external frequency generator. RBW = 10 Hz. Feedback gain = 1.

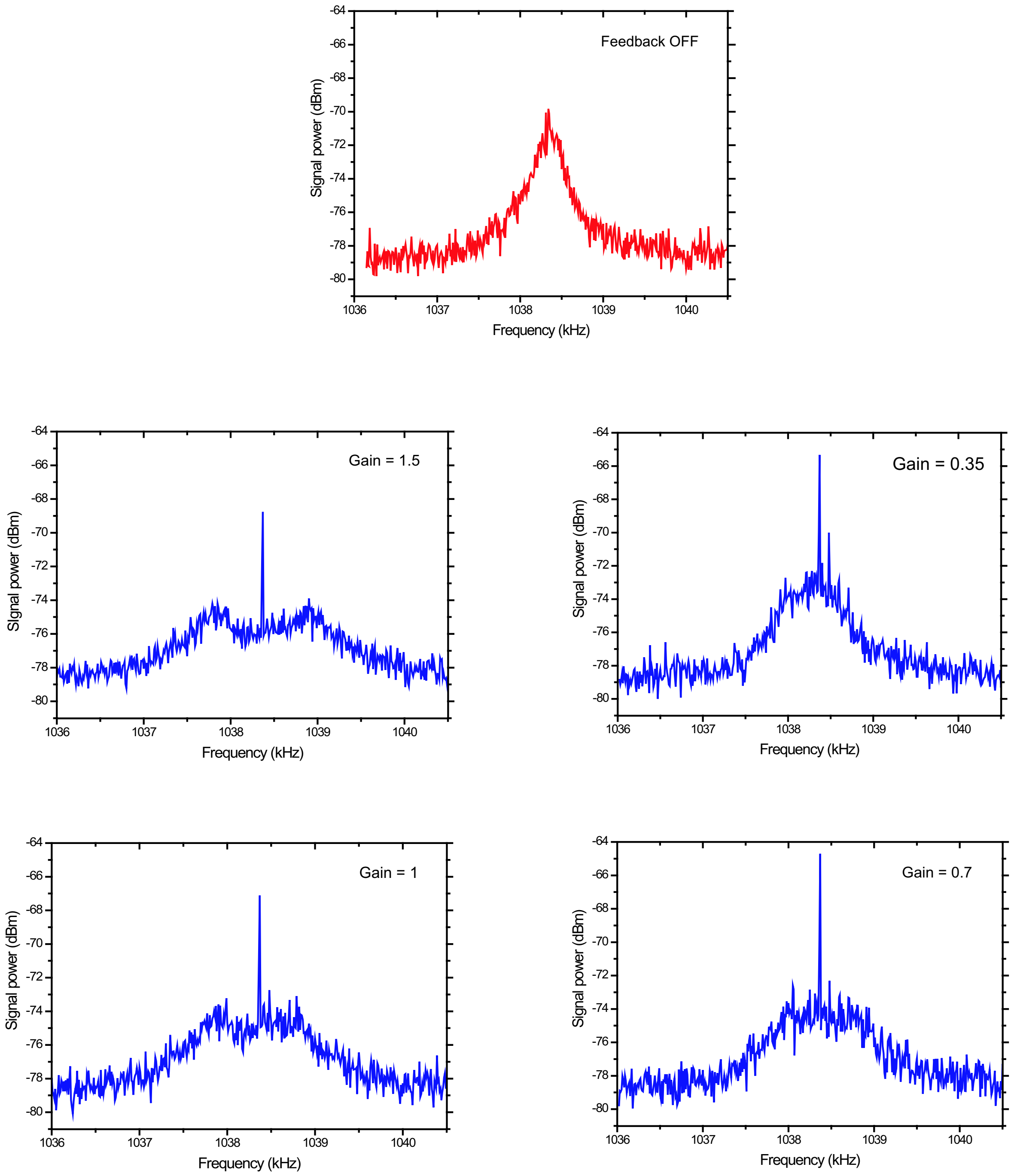

Figure 9.10: The evolution of the sideband spectrum in locking conditions with different feedback gains. RBW = 10 Hz.

and the measured width of that spike is less than 3 Hz, see Fig. 9.11. The non-zero

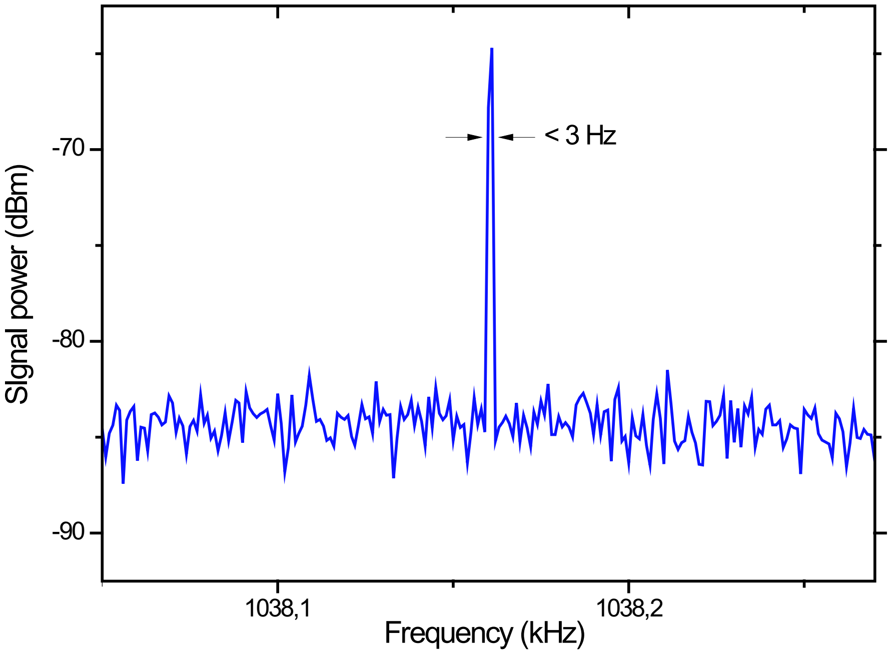

Figure 9.11: The phase locking spectra taken with smallest resolution which is possible on the spectrum analyzer, RBW = 1Hz. This is a detailed version of the spectra which is shown in Fig. 9.10. Feedback gain = 1.

linewidth of the locked signal is determined not only by the resolution bandwidth of the spectrum analyzer but also by the fact that FFT analyzer is not connected to the 10 MHz time-base network of the frequency source for the lock signal. This results in a phase jitter between the primary generator and FFT analyzer which explains the size of the bandwidth of the locked signal.

9.4.4 Phase locking of a mono-ion oscillator to FM signal

Once the motion of the ion can be synchronized to a sinusoidal signal, it would be also interesting to synchronize the frequency of the motion to the signal with varying frequency, i.e. to the frequency modulated signal (FM-signal), as has been described in subsection 9.4.2.

With the external generator switched to FM mode, the frequency span and the FM rate are set to 56.3 Hz, hence the modulation index is equal to 1. The particular value of the span and rate is chosen such that it is smaller than the bandwidth of the loop filter and it is not equal to 50 Hz (power supply frequency) and harmonics of that. The spectrum of the sideband in locking conditions and FM signal are shown in

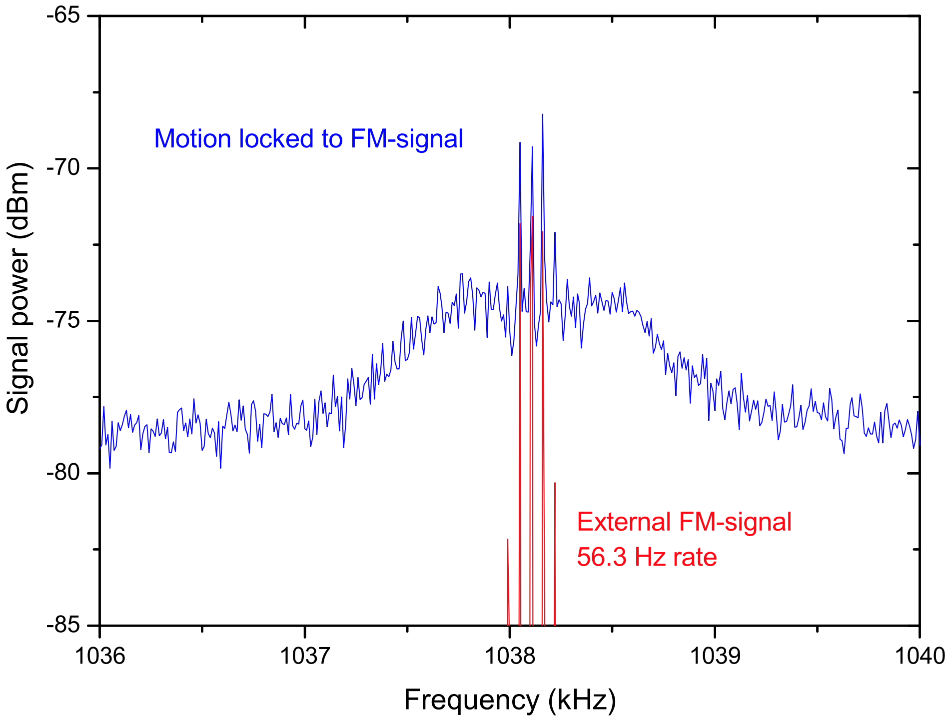

Figure 9.12: The sideband spectrum(blue curve) when locked to FM modulated signal(red curve) with the frequency span 56.3 Hz and the modulation index is equal to 1. Feedback gain = 1. RBW = 10 Hz. FM modulated signal is 60 dB attenuated.

Fig. 9.12. Four FM spikes are revealed in the sideband spectrum with frequencies equal to the sidebands of the FM signal. Other FM sidebands disappear in the noise floor. This measurement shows that in principle we can encode and decode phase/frequency information into the motion of the single trapped atom.

9.5 The conclusion and outlook for PLL feedback experiment

The temperature of an ion, or its kinetic energy is equal to the area under its sideband spectrum and it does not change during the feedback operation. Nevertheless, the shape of the sideband is not Lorentzian for feedback gains greater than 0.3. This means that the part of the sideband energy inside the Doppler profile will be redistributed by the feedback loop over its frequency bandwidth. Some part of the energy will be transferred to coherent oscillations. This is reminiscent of the Mössbauer effect, where the recoil energy is absorbed by the crystal lattice. Therefore one could say that this is a direct analogy to the effect we observed, because during the feedback operation the recoil momentum will be absorbed by the feedback giving an effective line narrowing. Nevertheless, the physics behind this PLL control is different. The recoil frequency of the photon during the Doppler cooling is about 6 kHz and it is absorbed by the trap. We do not see the recoil on the sideband spectra! The ion can be represented as a wave packet moving back and forth in the trap potential with the sideband frequency, and the PLL feedback only stimulates the ion to move more coherently.

The size of coherent oscillations can be calibrated by using spectra of excited motion, and the amplitude of the oscillations are then found to be approximately 25 nm. As previously mentioned the ion motion in the trap can be represented as the motion of the harmonic oscillator. The mean energy of that oscillator is set by the Doppler cooling process. We can even say that the harmonic oscillator is connected to the thermal bath with a temperature greater then the oscillation frequency (the case when $kT \gg \hbar\Omega$, see [34]). The width of the motional spectra is a damping rate and is due to the cooling process. In that case the behavior of that oscillator can be treated classically, see [86]. Due to the action of the PLL feedback the harmonic oscillator (the single Ba^+ion) starts to move more coherently, and the oscillation frequency is kept the same by the PLL. Hence the temperature or kinetic energy also remains the same!

Here we want to mention some current task and make an outlook for future experiments. The first task would be to determine the quantum state of motion, and how this is connected to the spectrum of the sideband.

The PLL can recover only the phase/frequency information. It does not measure the amplitude of the ion's oscillations in a Paul trap. Therefore, the second task would be to incorporate the quadrature detector into the PLL, in order to acquire complete information about the ion's motion.

Once the ion motion can be locked to an external generator, we could try to phase-lock the motion of the ion to the motion of another ion which would be confined in a different trap. This has recently achieved with frequencies of lasers, and perhaps it would be illuminating to do the same for the motional phase/frequencies of a different massive particles.

10 Towards quantum feedback

It is known that a single trapped ion can be cooled by means of different optical techniques: Doppler cooling, EIT cooling, sideband cooling. Doppler cooling can reduce the thermal motion of the ion to temperatures of about $k_B T \sim \hbar\Gamma/2$, while sideband and EIT cooling, in principal, can be used to cool the ion's motion down to the ground state [87]. We demonstrate the alternative, electro-mechanical method to cool the ion's motion below its Doppler-limit by using "cold damping" or homodyne feedback control [35, 93].

We create an additional friction force, which is proportional to the "instantaneous speed" of the ion in the trap, by supplying additional electric fields along the direction of the ion's motion. We observe a reduction of the thermal energy of the ion to 1/2 of the initial value. For sufficiently high loop gain the motion becomes correlated with the Poissonian noise of the photocurrent, thus producing a hole in the noise spectrum.

While this kind of feedback technique been used earlier to cool a vibrational mode of a mirror [36], we believe this is its first demonstration with a single particle at the quantum noise limit. Here we present the first experimental results on this topic.

10.1 Thermally excited harmonic oscillator

As mentioned in Chapter 9 the motion of a single ion in the trap can be approximated by the motion of a damped harmonic oscillator externally excited by stochastic forces. The latter are often called Langevin forces and describes the coupling of the oscillator to the thermal bath with some temperature T [88]. Let us take an oscillating mass on a spring as a model for the ion's motion in a Paul trap which undergoes Doppler cooling. We can also say that the oscillator, which represents the motion of the trapped ion, is now connected to the thermal bath with a temperature on the order of $T \sim \hbar\Gamma/2k_B$, where Γ is the linewidth of the atomic transition and k_B is Boltzman constant (see also section 2.2).

The equation of the motion of the oscillator can be written as

$$\ddot{x} + \gamma\dot{x} + \omega_M^2 x = F_T(t)/M \ , \tag{10.1}$$

where γ is the damping or cooling rate of the oscillator, ω_M its mechanical frequency, $F_T(t)$ is the Langevin force and M is the mass of the oscillator. In the framework of the linear response theory (for details see [88]) the spectrum of the resulting motion can be expressed via the mechanical susceptibility of the oscillator $\chi(\omega)$ and we obtain:

$$x(\omega) = \chi(\omega) F_T(\omega) = \frac{F_T(\omega)}{M(\omega_M^2 - \omega^2 - i\gamma\omega)} \ . \tag{10.2}$$

The power spectrum can be calculated through the power spectrum of the Langevin force $S_{F_T}(\omega)$ by

$$S_x(\omega) = |\chi(\omega)|^2 S_{F_T}(\omega) \ . \tag{10.3}$$

Assuming that the oscillator is in thermal equilibrium with the thermal bath, $S_{F_T}(\omega)$ can be calculated using the fluctuation-dissipation theorem [88]

$$S_{F_T}(\omega) = -\frac{2k_B T}{\omega} \mathrm{Im}[1/\chi(\omega)] = 2M\gamma k_B T. \tag{10.4}$$

Substituting this equation into Eq. 10.3, and assuming a high value of the quality factor of the mechanical resonance (for the Ba$^+$ ion in Paul trap in our experimental conditions $Q = \omega_M/\gamma \sim 1000$ kHz $/0.5$ kHz $= 20000$), we finally calculate the power spectrum of thermally excited motion of the harmonic oscillator

$$S_x(\omega) = \frac{\gamma k_B T}{2M\omega_M^2} \frac{1}{(\omega_M - \omega)^2 + \frac{\gamma^2}{4}} \ . \tag{10.5}$$

The power spectrum of the oscillator motion excited at temperature T has a Lorentzian shape, as has already been verified in our experiment (see Chapter 7). The width of the spectrum is equal to the damping rate, and the area under the curve corresponds to the thermal energy of the oscillations and obeys the equipartition theorem

$$\frac{1}{2} M\omega_M^2 \overline{x^2} = \frac{1}{2} M\omega_M^2 \int S_x(\omega) d\omega = \frac{1}{2} k_B T, \tag{10.6}$$

where $\overline{x^2}$ is the averaged thermal variance of the oscillator position. If we look at Eq. 10.5 it becomes clear that by increasing the damping rate of the oscillator we decrease the area under the motional spectrum, and hence we also decrease the thermal variance of the oscillator position or, slow down its motion, although this is not apparent from Eq. 10.6. The reason is the damping rate from that equation cancels out because it appears both in the mechanical susceptibility and in the spectrum of the Langevin force.

10.2 Cold damping technique

To slow down the motion of the harmonic oscillator we will use a feedback loop which applies an additional force in such a way that this force is proportional to the speed of the oscillator but has an opposite direction

$$\vec{F}_{FB}(t) = -\alpha M \vec{v}(t), \tag{10.7}$$

where α is a constant and M is the mass of an oscillator. Thus the feedback loop exerts a viscous force on the harmonic oscillator, therefore its motion can be slowed. The Fourier spectrum of such a force will be then

$$F_{FB}(\omega) = i\omega M\gamma G x(\omega), \tag{10.8}$$

where G is the gain of the feedback loop.

The motion of the oscillator under feedback control arises from the action of the Langevin force and viscous force created by the feedback loop. We can rewrite Eq. 10.2 as

$$x(\omega) = \chi(\omega)[F_T(\omega) + F_{FB}(\omega)] = \chi_{FB}(\omega)F_T(\omega), \tag{10.9}$$

where $\chi_{FB}(\omega)$ is an effective mechanical susceptibility due to the action of the feedback loop given by

$$\chi_{FB}(\omega) = \frac{1}{M(\omega_M^2 - \omega^2 - i(1+G)\gamma\omega)} \ . \tag{10.10}$$

The additional viscous force exerted by the feedback loop increases the damping rate of the harmonic oscillator. The Langevin force is not modified by the feedback, hence the thermal energy of the motion is reduced. From Eq. 10.9 we obtain

$$S_{FB}(\omega) = \frac{\gamma k_B T}{2M\omega_M^2}\frac{1}{(\omega_M - \omega)^2 + (1+G)^2\frac{\gamma^2}{4}} \ . \tag{10.11}$$

Performing the integration of Eq. 10.11 over the entire frequency range yields

$$\frac{1}{2}M\omega_M^2\overline{x^2} = \frac{1}{2}M\omega_M^2\int S_{FB}(\omega)d\omega = \frac{k_B T}{2(1+G)} \ . \tag{10.12}$$

Therefore the feedback control will reduce the temperature of the harmonic oscillator by a factor of $1+G$. Note that the damping rate of the oscillator will be increased by the same factor, while the temperature of the thermal bath remains unchanged! This cooling method using the active feedback control is often called the *cold damping technique* [35,89] or *stochastic cooling*. The latter method has been used to slow down the transverse oscillations of the protons in accelerator beam [91]. The difference between cold damping and stochastic cooling is that the latter method will shift the oscillation frequency [90].

In the real experimental situation there is always noise which influences the system. For example in our experiment there is Poissonian noise appearing during the photodetection process. In the theoretical description which we have just presented this is not taken into account. However, a more detailed analysis can be found in [92,93].

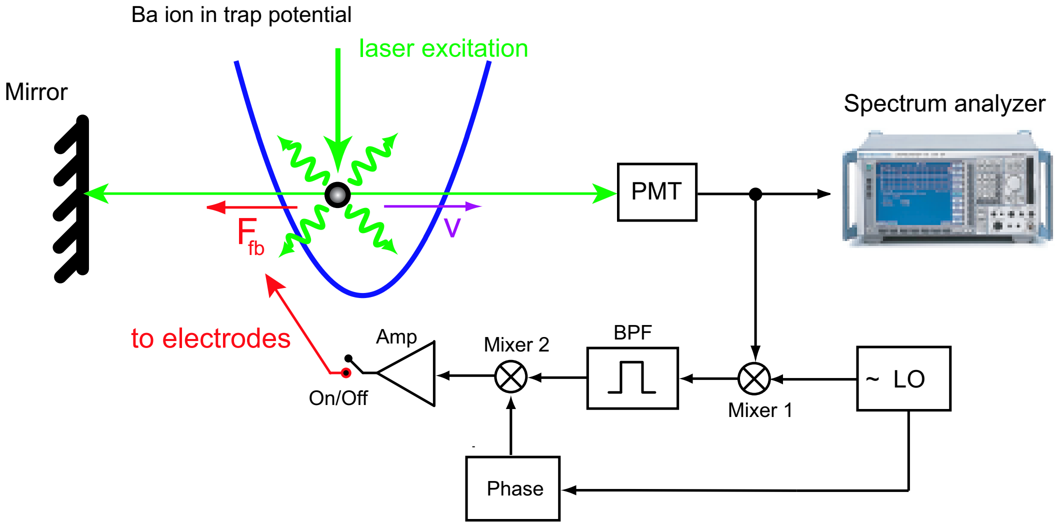

Figure 10.1: The experimental setup for feedback cooling of the ion oscillation in a Paul trap.

10.3 Experimental setup

The experimental setup is shown in Fig. 10.1. The optical part of that experiment is the same as has been described in Chapter 7. The motion of the single Ba^+ ion is detected in an interference experiment, and this procedure has also been described in Chapter 7.

The resonance fluorescence of the Ba^+ ion has a level of approximately of 6000 counts per 100 ms. The green laser is detuned to half of the linewidth, the red laser is kept on resonance. The contrast of the interference fringes is 40%. The mirror position is set by the fringe lock to the middle of the interference slope for better detection of the ion's motion. The motional sideband signal is observed on a FFT-spectrum analyzer and has a frequency $f_y \approx 1200$ kHz (Y-mode) with a signal-to-noise ratio of 6-8 dB above the Poissonian noise level. The width of the sideband is determined by the laser cooling process [75] and is in agreement with the expected value of about 400 Hz.

The resonance fluorescence is detected by PMT, and the part of that signal is going to the electronic feedback loop which consists of the local oscillator (LO), mixer stages, crystal bandpass filter (BPF), phase rotator (Phase), amplifier with variable gain. The input signal is mixed up with the LO (signal synthesizer SML-01) to match the transmission frequency band of the bandpass filter. We use a crystal filter with the center frequency of $f_o = 10.7$ MHz and 3 dB bandwidth of about 30 kHz. The 60 dB stop bandwidth is equal to 130 kHz. The phase characteristic of such a filter on a maximum transmission is rather steep, thus ±90° phase cross-over points limits the efficiency of a feedback loop to a bandwidth of about 6 kHz.

After filtration the signal is again mixed down with the local oscillator and thus acquires its phase. Upper sidebands while appeared during mixing are rejected with a low-pass filter (omitted for simplicity) and the signal then goes to the amplifier. The output signal has an amplitude of approximately 1 mV, is resonant again with the ion's oscillation frequency and is supplied to the end cap electrodes (see Chapter 9). The phase of the output signal can be tuned from –220° to +220° with respect to the input signal. Therefore the force applied to the ion's motion could be the viscous force (cooling mode) or accelerating force (heating mode).

10.4 Experimental results

The sideband spectra measured without feedback action and with a different value of feedback gain are shown in Fig. 10.2. Here the phase of the feedback loop is equal to –90° and creates a viscous force for the ion motion. The presented curves are obtained after averaging 200 scans of the spectrum analyzer with a resolution bandwidth of 30 Hz. The baseline for each spectrum corresponds to the Poissonian noise level which remains at the same level, because the feedback does not influence the intensity of the resonance fluorescence.

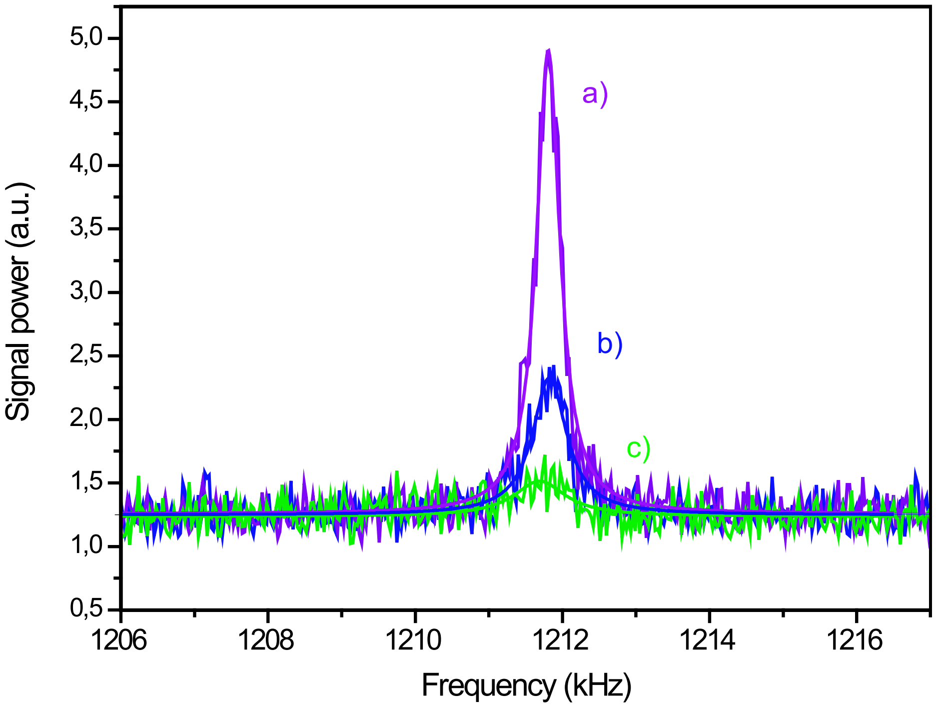

Figure 10.2: Sideband spectra recorded without feedback (curve a), with feedback G = 0.3 (curve b), and with G = 0.7 (curve c).

In Fig. 10.2 the curve a) corresponds to the spectrum of the Y-mode of the ion's oscillations, with a center frequency of $\omega_M = 2\pi\times$ 1211.8 kHz and a width of $\gamma = 2\pi\times$ 380 Hz. Curves b) and c) are obtained under feedback action with increasing gain. The area under the sideband spectrum is strongly decreased while its width becomes approximately 6 times larger, which corresponds to further cooling of the Y-mode of the ion motion.

The thermal energy of the ion motion cannot be calculated from the Eq. 10.12 because of the presence of the Poissonian noise, which also influences the motion. Nevertheless, the measured spectrum of the motion in the presence of background noise can be described by (for details see [36, 92]) by:

$$S^N_{FB}(\omega) = [1 - \frac{1}{SNR}G(2+G)]S_{FB}(\omega) + S_{PNL}(\omega), \tag{10.13}$$

where SNR is the signal-to-noise ratio at resonance, $S_{FB}(\omega)$ is the spectrum calculated from Eq. 10.11, and $S_{PNL}(\omega)$ is the spectrum of the Poissonian noise. The feedback gain in Fig. 10.2 is calculated by fitting the measured spectra with Eq. 10.13 and is less than the electronic gain of the amplifier by a factor of 3. The spectrum shape remains Lorentzian with the baseline equal to the Poissonian noise level, but the measured area

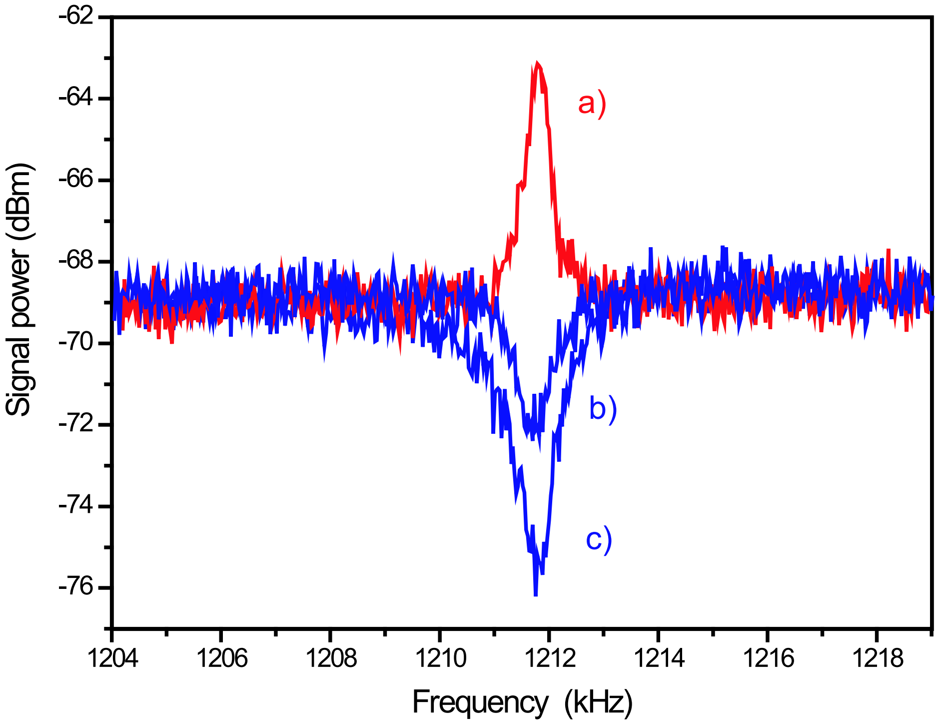

Figure 10.3: Sideband spectra recorded without feedback (curve a), with feedback G = 1.2 (curve b), and with G = 2.2 (curve c).

of the sideband is less than in the case of noiseless feedback described in section 10.2.

The sideband spectra without feedback action and with higher feedback gain than in Fig. 10.2 are shown in Fig. 10.3. The gain of the feedback is calculated again from the fit of the measured spectra. One can see, that for high gain the sideband spectrum is completely eliminated by the feedback action, furthermore the feedback digs a hole in the background noise floor (it happens when the first term in Eq. 10.13 becomes negative). The Poissonian noise suppression achieved in our experiment is about 7 dB. This reflects the fact that the cold damping feedback starts to work against the background noise.

The feedback loop which cools the ion's oscillation works also as an intensity stabilizer. The theory and experimental results obtained for this kind of feedback loop can be found in [76, 94]. The authors have also measured the the Poissonian noise suppression up to 12.5 dB inside the feedback loop with the gain of the feedback (this is the case of the intensity stabilizer based on the electro-optical modulator), whereas the noise of the light which has been measured outside the feedback loop becomes 2 dB larger.

In our case, the phase of the ion's motion induced by the feedback loop with respect to the input signal is equal $-90°$ (coming from the phase shift) $-90°$ (response on the resonance) giving a total phase shift of $-180°$. If the input signal is due to intensity fluctuation, then the feedback tries to keep the intensity at the constant level by supplying the signal proportional to the amplitude of the fluctuations but with the opposite phase. Therefore the current state and the light fluctuation are anti-correlated inside the feedback loop, which results in Poissonian noise suppression, and this effect cannot be associated with the light squeezing.

During the measurement the motional spectrum appears as a resonance line on the top of the noise floor, see Chapter 7, because the oscillation of the trapped ion is uncorrelated with the Poissonian noise. The action of the feedback loop will decrease the level of the Poissonian noise inside the band of the feedback loop as described above. Therefore, the measurement of the motion inside the loop is strongly affected by suppressed light fluctuations. To separate contributions of the light fluctuations and the actual ion's motion to the measured spectrum one has to measure the spectra outside the loop, as has been done in [94].

In a future experiment we are going to split the light beam coming from the ion into two parts. One beam will be used for the feedback purposes, the other beam will be used to detect the actual motional spectrum and will therefore allow us to measure the thermal energy of the single ion.

11 Summary and conclusions

The work presented here started with a description of the experimental setup which has been already built in [38]. The Ba^+ is cooled to the Lamb-Dicke regime and can be reliably stored in the trap for a sufficient long time (more than 5 hours). The interference experiment [6,38] described in Chapter 6 demonstrated the interference of the ion with its mirror image was demonstrated with a visibility of more than 70%. The mirror induced modification of the spontaneous decay rate on the $P_{1/2} \rightarrow S_{1/2}$ transition was measured by observing fringes in the fluorescence on the $P_{1/2} \rightarrow D_{3/2}$. The value of this decay rate change is approximately 1.5% and is determined by the size of the beam waist on the focal point of the HALO 25/04 lens which is approximately 1.8 times larger than the optical diffraction limit for that lens.

The modification of the spontaneous emission rate of an atom is always accompanied by the shift of the excited atomic state. In Chapter 6 the shift of the $P_{1/2}$ state of a single Ba^+ ion was measured in an interference experiment. The main signature of the level shift is that the phase between the green interference fringes and the red modulation (correlation phase) is not constant with regard to dependence of the detuning of the 650 nm laser and it was experimentally demonstrated. The level shift has been calculated from the fit of theoretically calculated contrast of the red fringes versus the detuning of the 650 nm laser to the experimental data. The level shift has a magnitude of 240 ± 60 kHz, and as in the case of the modification of the spontaneous decay rate is also limited by the quality of the focus of the HALO 25/04 lens. It has been also demonstrated that for certain parameters of the 650 nm laser (blue detuning, high intensity) behavior of the correlation phase becomes non-trivial. This effect is assumed to be due to the interplay of the modified decay and optical pumping. The detailed underlying causes could be the subject of future study.

Chapter 7 showed that RF spectral analysis of the resonance fluorescence from an ion in the interference experiment is one of the most sensitive methods to detect an ion's macro-motion ever shown so far. In our experiment we measured the spectrum of all three macro-motion sidebands with a signal-to-noise ratio from 1.5 dB to 12 dB with a resolution bandwidth up to 100 Hz. It was found that a particular size of the sideband signal is mainly determined by the direction of the cooling beam. The noise floor is determined by the Poissonian noise level arising from the photo-detection process. We assume the signal-to-noise ratio can be improved in a future setup by either increasing the fluorescence collection from the single ion or by mixing the fluorescence with the strong local oscillator, i.e. by introducing a homodyne or heterodyne technique.

The energy shift of the $P_{1/2}$ state has a sinusoidal dependence on the ion-mirror distance, thus leading to a spatially dependent force on the excited ion which changes the trap frequency by up to 300 Hz. We measure this variation of the trap frequency with < 10 Hz error by positioning the ion with nanometer accuracy relative to the mirror and detecting the intensity modulation in the scattered light due the ion's oscillation in the combined trap and the mirror induced potential. The trap frequency shift is also measured by observing the dependence of the level shift on the fluorescence rate (excitation probability of the upper state). As predicted this relationship is linear.

The level shift of the excited state can be treated from the classical point of view, i.e. in terms of the reaction of the ion to its own retroreflected field. The valid description of the atom-field interaction demands use of an adequate apparatus of quantum electrodynamics, in which vacuum field appears. Although it is impossible to separate the action of the real field from the action of the fluctuations of the electromagnetic vacuum in the present experiment, we believe that the action of the pure vacuum field would be revealed only in either relativistic experiments or by introducing some asymmetry into the system, i.e. squeezed states, strong magnetic or electrical fields, fast moving boundaries, dielectric boundaries, etc. The interesting proposal of how an atom or molecule can acquire momentum from the vacuum field has been proposed recently in [95]. Nevertheless, the question "What is the vacuum field really?" remains unsolved.

It is possible to optically reconstruct the trajectory of the ion's motion in the interference experiment. This measurement is described in Chapter 9. The phase plot of the ion's trajectory in the X oscillation mode was measured with an accuracy of 12 nm (limited by the presence of the Poissonian noise). Furthermore we demonstrate for the first time phase locking of the ion's oscillation in the Paul trap not only to the pure sinusoidal signal but also to the FM signal with a frequency span of 56.3 Hz and modulation index of 1. The phase-locking spike of 8 dB above the noise floor appears on the sideband spectrum showing that the oscillation becomes more coherent.

In the last chapter 10 we demonstrated the alternative, electro-mechanical method of cooling the ion's motion below its Doppler-limit by using "cold damping" or homodyne feedback control. It is shown that the spectrum of the ion's oscillation with feedback control still remains Lorentzian and its area decreases with increasing the gain of the feedback. For sufficiently high loop gain the motion becomes correlated with the Poissonian noise of the photocurrent, thus producing a hole which is 7 dB less than the noise floor. While this kind of feedback technique has been used earlier to cool a vibrational mode of a mirror, we believe that this is its first demonstration with a single particle at the quantum noise limit. The thermal energy of the ion's oscillation is not yet known and we plan to measure this in the near future outside of the feedback loop. The cooling limit for that kind of feedback is still the subject of future theoretical and experimental studies.

Bibliography

[1] H. R. Hertz. *On electric radiation*, Annalen der Physik und Chemie **36**, 1 (1889). See also H. Hertz. *Electric Waves*, translation by D. E. Jones, Dover Publications, New York (1962).

[2] D. V. Sivukhin, *General Physics. Vol.3 (Electricity).* Moscow Institute of Physics and Technology (2002).

[3] V. L. Lyuboshitz. *Scattering of electromagnetic waves by a system of dipole centers*, Soviet Phys.-JETP **25**, 612 (1967).

[4] L. V. Black. *Antennas*, John Wiley and Sons (1966).

[5] K. H. Drexhage, H. Kuhn, and F. D. Schafer, Ber. Bunsen Ges. Phys. **72**, 329 (1968).

[6] J. Eschner, Ch. Raab, F. Schmidt-Kaler, R. Blatt. *Light interference from single atoms and their mirror images*, Nature **413**, 496, (2001)

[7] J. E. Lennard-Jones, Proc. Camb. Phil. Soc. **27**, 469 (1931).

[8] H. B. G. Casimir and D. Polder. *The Influence of Retardation on the London-van der Waals Forces*, Phys. Rev. **73**, 360 (1948).

[9] H. Morawitz. *Self-coupling of a two-level system by a mirror*, Phys.Rev. **187**, pp.1792-1796(1969).

[10] G. Barton. *Quantum-electrodynamic level shifts between parallel mirrors: analysis* Proc. R. Soc. Lond. A **410**, 141-174 (1987).

[11] D. Meschede, W. Jhe and E. A. Hinds. *Radiative properties of atoms near a conducting plane: An old problem in a new light*, Phys.Rev. **41**, pp. 1587-1596 (1990).

[12] E. A. Hinds. *Cavity quantum electrodynamics*, Adv. At. Mol. Opt. Phys. **28**, 237-289 (1991).

[13] D. J. Heinzen and M. S. Feld. *Vacuum radiative level shift and spontaneous-emission linewidth of an atom in an optical resonator* Phys. Rev. Lett. **59**, 2623 (1987).

[14] M. Brune, P. Nussenzveig, F. Schmidt-Kaler, F. Bernadot, A. Maali, J. M. Raimond, S. Haroche. *From Lamb shift to light shifts: Vacuum and subphoton cavity fields measured by atomic phase sensitive detection* , Phys. Rev. Lett. **72**, 3339-3342 (1994).

[15] U. Dorner and P. Zoller. *Laser-driven atoms in half-cavities* , Phys. Rev. A **66**, 023816 (2002).

[16] M. A. Wilson, P. Bushev, J. Eschner, F. Schmidt-Kaler, C. Becher, R. Blatt and U. Dorner. *Vacuum-field lavel shift mediated by a single distant mirror*, Phys.Rev.Lett. **91** (2003).

[17] A. Mundt. *Cavity QED with single trapped* $^{40}Ca^{+}$*-ions* , *PhD thesis*, Innsbruck 2003.

[18] P. W. Milonni. *The quantum vacuum*, Academic press, San Diego (1994).

[19] P. W. Milonni, J. R. Ackerhalt, W. A. Smith. *Interpretation of Radiative Corrections in Spontaneous Emission*, Phys. Rev. Lett. **31**, 958-960 (1973).

[20] J. R. Ackerhalt, P. L. Knight, J. H. Eberly. *Radiation Reaction and Radiative Frequency Shifts* , Phys. Rev. Lett. **30**, 456 (1973).

[21] J. Dalibard, J. Dupont-Roc, C. Cohen-Tannoudji. *Vacuum fluctuations and radiation reaction: identification of their respective contributions* J. Physique (Paris) **43**, 1617 (1982).

[22] E. A. Hinds and V. Sandoghdar. *Cavity QED level shifts of simple atoms*, Phys.Rev. A **43**, pp. 398-403 (1991).

[23] P. N. Lebedev. *Experimental examination of light pressure*, Annalen der Physik **6**, 433-458 (1901).

[24] R. Frisch. *Experimental demonstration of Einstein's radiation recoil*, Z. Phys. **86**, 42-48 (1933).

[25] K. Dholakia, G. Spalding and M. MacDonald. *Optical Tweezers: the next generation*, Physics World **15**, 31-35 (2002).

[26] S. Haroche, M. Brune, and J. M. Raimond. *Trapping atoms by the vacuum field in a cavity*, Europhys. Lett. **14**, 19-24 (1991).

[27] C. Schön and J. I. Cirac,*Trapping atoms in the vacuum field of a cavity*, Phys. Rev. A **67**, 043813 (2003).

[28] G. R. Guthöhrlein, M. Keller, K. Hayasaka, W. Lange, and H. Walther. *A single ion as a nanoscopic probe of an optical field* Nature **414**, 49-51 (2001).

[29] A. B. Mundt, A. Kreuter, C. Becher, D. Leibfried, J. Eschner, F. Schmidt-Kaler, R. Blatt. *Coupling a single atomic quantum bit to a high finesse optical cavity*, Phys. Rev. Lett. **89**, 103001 (2002).

[30] J. I. Cirac and P. Zoller. *Quantum Computations with Cold Trapped Ions* , Phys. Rev. Lett. **74**, 4091-4094 (1995).

[31] C. Monroe, D. M. Meekhof, B. E. King, W. M. Itano, and D. J. Wineland. *Demonstration of a Fundamental Quantum Logic Gate* , Phys. Rev. Lett. **75**, 4714-4717 (1995).

[32] F. Schmidt-Kaler, H. Häffner, M. Riebe, S. Gulde, G. P. T. Lancaster, T. Deuschle, C. Becher, C. F. Roos, J. Eschner, and R. Blatt. *Realization of the CiracZoller controlled-NOT quantum gate*, Nature **422**, 408-411 (2003).

[33] D. Leibfried, B. DeMarco, V. Meyer, D. Lucas, M. Barrett, J. Britton, W. M. Itano, B. Jelenkovich, C. Langer, T. Rosenband, and D. J. Wineland. *Experimental demonstration of a robust, high-fidelity geometric two ion-qubit phase gate*, Nature **422**, 412-415 (2003).

[34] V. B. Braginsky and F. Y. Khalili. *Quantum measurement*, Cambridge University Press (1992).

[35] J. M. W. Milatz and J. J. Van Zollingen. Physica (Amsterdam) **19**, 181 (1953).

[36] P. F. Cohadon, A. Heidmann, and M. Pinard. *Cooling of a Mirror by radiation pressure* Phys. Rev. Lett. **83**, 3174 (1999).

[37] V. B. Braginsky and Y. I. Vorontsov. Soviet Physics Uspekhi **17**, 644 (1975).

[38] Ch. Raab. *Interference experiments with the fluorescence light of Ba$^+$ ions, Ph.D.thesis*, Universität Innsbruck (2001)

[39] W. Paul, O. Osberghaus, and E. Fischer. *Ein Ionenkäfig.* Forschungsberiechte des Wirtschafts- und Verkehrsministeriums Nordrhein-Westfalen 415, Westfälischer Verlag (1958).

[40] R. Blatt, P. Gill, and R. C. Thompson. *Current perspectives on the physics of trapped ions*, J. Mod. Opt. **39**(1992).

[41] C. Raab, J. Bolle, H. Oberst, J. Eschner,F. Schmidt-Kaler, R. Blatt. *Diode laser spectrometer at 493 nmfor single trapped Ba ions*, Aplied Optics B **67**, pp. 683-688 (1998).

[42] P. K. Ghosh. *Ion traps.* Clarendon press (1995)

[43] S. Stenholm. *The semiclassical theory of laser cooling*, Rev. Mod. Physics **58**, 699-739 (1986).

[44] J.Eschner *Sub-wavelength resolution of optical fields probed by single trapped ions: Interference, phase modulation, and which-way information*, Eur. Phys. J. D **22**, 341-345 (2003).

[45] D. V. Sivukhin. *General Physics. Vol.4 (Optics)*, Moscow Institute of Physics and Technology (2002).

[46] V. M. Fain and Ya. I. Khanin. *Quantum radiophysics*, Soviet radio (1965).

[47] A. M. Afanasiev and Yu. Kagan, Soviet Physics JETP Letters **2**, 81 (1965).

[48] J. D. Jackson. *Classical electrodynamics*, John Wiley and Sons (1975).

[49] W. Heitler. *The quantum theory of radiation.* 3rd eddition, Dover publications, New York (1984).

[50] S. Haroche in *Fundamental systems in quantum optics, Les Houches 1990*, North Holland (1992).

[51] A. E. Sigman. *Lasers*, University Science Books (1986).

[52] IEEE History center, *http://www.ieee.org/organizations.*

[53] V. Weisskopf und E. Wigner. *Calculation of the natural breadth of spectral lines on the basis of Dirac's theory of light*, Z. Phys. **63**, 54 (1930).

[54] L. D. Landau and E. M. Lifshitz. *Course of theoretical physics: Field theory*, Physmatlit Moscow (2002).

[55] W. E. Lamb, Jr. and R. C. Retherford. *Fine structure of the Hydrogen atom by a microwave method*, Phys.Rev. **72**, 241-243 (1947).

[56] H. Dehmelt. *Experiments with an isolated subatomic particles at rest*, Rev. Mod. Phys. **62**, 525 (1990).

[57] H. A. Bethe. *The electromagnetic shift of energy levels*, Phys. Rev. **72**, 339-341 (1947).

[58] R. Loudon. *The quantum theory of light*, Oxford University Press (2000).

[59] C. Cohen-Tannoudji, J. Dupont-Roc, G. Grynberg. *Photons and Atoms*, Wiley Intelligence, New-York (1989).

[60] J. J. Sakurai. *Advanced Quantum Mechanics* , Addison-Wesley Pub Co. (1967).

[61] A. B. Migdal. *Qualitative methods in quantum theory* Nauka publ. Moscow (1975).

[62] R. Feynman. *Quantum electrodynamics*, Addison-Wesley Pub Co. (2000).

[63] K. H. Drexhage. in *Progress in Optics XII* vol.12, p.165 , Amsterdam, North Holland (1974).

[64] J. M. Wylie, J. E. Sipe. *Quantum electrodynamics near an interface*, Phys.Rev. A **30** 1185 (1984); Phys. Rev. A **32** 2030 (1985).

[65] P. W. Milonni and M. L. Shih. *Source theory of the casimir force* , Phys. Rev. A **45**, 4241 (1992).

[66] I. R. Senitzky. *Radiation-Reaction and vacuum-field effects in heisenberg-picture quantum electrodynamics* Phys. Rev. Lett. **31**, 955 (1973).

[67] G. Barton. *Frequency shifts near an interface: Inadequacy of two level atomic models*, J. Phys. B **7**, 2134 (1974).

[68] H. Oberst. *Resonance fluorescence of single barium ions* , *Diploma thesis*, Innsbruck University (1999).

[69] M. O. Scully and M. S. Zubairy. *Quantum optics*, Cambridge Univerisity Press (1997).

[70] P. L. Knight. *The Rabi frequency in optical spectra*. Phys. Rep. **66**, pp.21-107 (1980).

[71] W. Vogel, D. Welsch, S. Wallentowitz. *Quantum optics an introduction*. Wiley-VCH, Berlin (2001).

[72] W. Vogel and R. Blatt. *Resonance fluorescence from three-level atoms: Atomic coherences and squeezed light*, Phys. Rev. A **45**, pp. 3319-3328 (1992).

[73] R. K. Wagness and F. Bloch. *The dynamical theory of nuclear induction* , Phys. Rev. **89**, 728 (1953).

[74] M. Born and E. Wolf. *Principles of Optics*. 6-th edition, Pergamon Press (1984).

[75] C. Raab, J. Eschner, J. Bolle, H. Oberst, F. Schmidt-Kaller and R. Blatt. *Motional sidebands and direct measurement of the cooling rate in the resonance fluorescence of a single trapped ion* , Phys. Rev. Lett. **85** pp. 538-541 (2000).

[76] D. N. Klyshko, A. V. Masalov. *Photon noise: observation, squeezing, interpretation.* Physics-Uspekhi **38** pp.1203-1231 (1995).

[77] R. J. Glauber. *Quantum radiophysics*(Russian edition), Nauka, Moscow (1975).

[78] M. Lindberg. *Resonance fluorescence of a laser-cooled trapped ion in the Lamb-Dicke limit.* Phys. Rev. A **34** pp.3178-3189 (1986).

[79] J. I. Cirac, R. Blatt, A. S. Parkins and P. Zoller. *Spectrum of resonance fluorescence from a single trapped ion* , Phys. Rev. A **48**, pp.2169-2181 (1993).

[80] P. Bushev, A. Wilson, J. Eschner, C. Raab, F. Schmidt-Kaler, C. Becher, and R. Blatt. *Forces between a single atom and its distant mirror image*, Phys. Rev. Lett. **92**, 223602 (2004).

[81] H. Fearn, R. J. Cook, P. W. Milonni. *Sudden replacement of a mirror by a detector in cavity QED: are photons counted immediately*, Phys. Rev. Lett. **74**, pp.1327-1330 (1995).

[82] P. Bertet, S. Osnaghi, A. Rauschenbeutel, G. Nogues, A. Auffeves, M. Brune, J. M. Raimond, S. Haroche. *A complementarity experiment with an interferometer at the quantum-classical boundary*, Nature **411**, pp. 166-170 (2001).

[83] F. M. Gardener. *Phaselock Technique*, Wiley (1979).

[84] D. Lancaster. *Active filter cookbook*, Newnes (1996).

[85] B. Sklar. *Digital communications. Fundamentals and applications*, Prentice Hall, New Jersey (2001).

[86] K. K. Liharev. *Really-quantum macroscopic effects in weak superconductivity*, Soviet Physics Usekhi 47, p. 87 (1983).

[87] F. Diedrich, J. C. Bergquist, W. M. Itano, and D. J. Wineland. *Laser cooling to the zero-point energy of motion* , Phys. Rev. Lett. **62**, 403 (1989).

[88] L. Landau and E. Lifshitz, *Course of Theoretical Physics: Statistical Physics*, Pergamon, New York (1958).

[89] F. Grassia, J. M. Courty, S. Reynaud and P. Touboul. *Quantum theory of fluctuations in a cold damped accelerometer* , Eur. Phys. J. D **8**, 101 (2000).

[90] D. Vitali, S. Manchini, L. Ribichini, and P. Tombesi. *Mirror quiescence and high-sensitivity position measurements with feedback*, Phys. Rev. A **65**, 063803 (2002).

[91] S. van de Meer. *Stochastic cooling and the accumulation of antiprotons*, Nobel lecture (1984).

[92] M. Pinard, P. F. Cohadon, T. Briant and A. Heidmann, *Full mechanical characterization of a cold damped mirror*, Phys.Rev. A **63**, 013808 (2002).

[93] S. Manchini, D. Vitali, and P. Tombesi. *Optomechanical cooling of a macroscopic oscillator by homodyne feedback*, Phys.Rev.Lett. **80**, 688 (1998).

[94] A. V. Masalov, A. A. Putilin, and M. V. Vasilyev. *Sub-Poissonian light and photocurrent shot-noise suppression in closed opto-electronic loop*, J. Mod. Optics **41**, 1941 (1994).

[95] A. Feigel. *Quantum vacuum contribution to the momentum of dielectric media*, Phys. Rev. Lett. **92**, 020404 (2004).